

Electrochemical Performance and Structural Changes of $\text{Na}_{0.67}\text{Mn}_{0.67}\text{Ni}_{0.33}\text{O}_2$ as Cathode for Sodium Ion Batteries

vorgelegt von

Master of Science

Li Zhang

von der Fakultät III – Prozesswissenschaften

der Technischen Universität Berlin

zur Erlangung des akademischen Grades

Doktor der Ingenieurwissenschaften

- Dr.-Ing. -

genehmigte Dissertation

Promotionsausschuss:

Vorsitzender: Prof. Dr. Walter Reimers

Gutachter: Prof. Dr. John Banhart

Gutachter: Prof. Dr. Martin Winter

Tag der wissenschaftlichen Aussprache: 15. Oktober 2019

Berlin 2019

**Helmholtz-Zentrum Berlin
für Materialien und Energie**

**Energie Materialien
Abteilung Mikrostruktur- und Eigenspannungsanalyse
EM-AME**

ERKLÄRUNG

Ich erkläre hiermit, dass ich die vorliegende Dissertation selbst verfasst und keine anderen als die angegebenen Quellen und Hilfsmittel verwendet habe.

Berlin, 08.2019

Li Zhang

Abstract

P2- and P3-type $\text{Na}_{0.67}\text{Mn}_{0.67}\text{Ni}_{0.33}\text{O}_2$ materials are potential cathodes for sodium ion batteries. P3-type $\text{Na}_{0.67}\text{Mn}_{0.67}\text{Ni}_{0.33}\text{O}_2$ demonstrates higher initial discharge capacity ($233 \text{ mAh}\cdot\text{g}^{-1}$) in the voltage range 1.5 - 4.5 V than P2-type $\text{Na}_{0.67}\text{Mn}_{0.67}\text{Ni}_{0.33}\text{O}_2$. However, the severe capacity fading in P3-type $\text{Na}_{0.67}\text{Mn}_{0.67}\text{Ni}_{0.33}\text{O}_2$ hinders its practical utilization as cathode for sodium ion batteries. Using X-ray absorption spectroscopy (XAS) measurements we investigate the redox mechanism of Mn and Ni and the local structural changes around Mn and Ni during cycling. The experiments show that the preferential occupancy of Na around Ni and the high redox activity of Ni mainly affect the expansion and shrinkage of TMO_2 layers resulting in capacity fading in P3-type material. In order to improve the cycling performance of P3-type material, we design a special core-shell design method to produce P3-type $\text{Na}_{0.67}\text{Mn}_{0.67}\text{Ni}_{0.33}\text{O}_2$. The core of the precursor is designed as Ni rich material and the shell is as Mn rich material. The core-shell designed P3-type material delivers higher specific capacity ($240 \text{ mAh}\cdot\text{g}^{-1}$) in the voltage range 1.5 - 4.5 V and better cycling performance in the range 2.0 - 4.1 V. The rate capabilities of the core-shell designed P3-type material are better than those of the normal P3-type material. Using *operando* XRD measurements, we investigate the structural evolution of P3-type materials. In the following, the core-shell designed P3-type $\text{Na}_{0.67}\text{Mn}_{0.67}\text{Ni}_{0.33}\text{O}_2$ is utilized as cathode for fast cycled sodium ion batteries. The cycling retention of P3-type material with core-shell structure is 89% after 1500 cycles of fast charge and discharge. Using XAS, we investigate the redox mechanism of Mn and Ni during fast and slow cycling. The reason for better cycling performance of the core-shell designed P3-type material is further studied from the sight of local structural changes around Mn and Ni.

Kurzfassung

P2- und P3- $\text{Na}_{0.67}\text{Mn}_{0.67}\text{Ni}_{0.33}\text{O}_2$ -Materialien sind mögliche Kathoden für Natriumionenbatterien. $\text{Na}_{0.67}\text{Mn}_{0.67}\text{Ni}_{0.33}\text{O}_2$ vom P3-Typ zeigt eine höhere anfängliche Entladekapazität ($233 \text{ mAh}\cdot\text{g}^{-1}$) im Spannungsbereich von 1,5 bis 4,5 V als $\text{Na}_{0.67}\text{Mn}_{0.67}\text{Ni}_{0.33}\text{O}_2$ vom P2-Typ. Das starke Nachlassen der Kapazität von $\text{Na}_{0.67}\text{Mn}_{0.67}\text{Ni}_{0.33}\text{O}_2$ vom P3-Typ behindert jedoch seine praktische Verwendung als Kathode für Natriumionenbatterien. Mit Röntgenabsorptionsspektroskopiemessungen (XAS) untersuchen wir den Redoxmechanismus von Mn und Ni und die lokalen Strukturänderungen um Mn und Ni während des Zyklus. Die Experimente zeigen, dass die bevorzugte Besetzung von Na um Ni und die hohe Redoxaktivität von Ni hauptsächlich die Ausdehnung und Schrumpfung von TMO_2 -Schichten beeinflussen, was zu einem Kapazitätsschwund in Material vom P3-Typ führt. Um die Zyklenfestigkeit von P3-Material zu verbessern, entwickeln wir eine spezielle Core-Shell-Konstruktionsmethode zur Herstellung von $\text{Na}_{0.67}\text{Mn}_{0.67}\text{Ni}_{0.33}\text{O}_2$ vom P3-Typ. Der Kern der Vorstufe ist als Ni-reiches Material und die Hülle als Mn-reiches Material ausgeführt. Das Core-Shell-Material vom P3-Typ bietet eine höhere spezifische Kapazität ($240 \text{ mAh}\cdot\text{g}^{-1}$) im Spannungsbereich von 1,5 bis 4,5 V und eine bessere Zyklenleistung im Bereich von 2,0 bis 4,1 V. Die Leistungsfähigkeit des Core-Shell-Materials vom Typ P3 ist besser als das normale Material vom P3-Typ. Mit Hilfe von Operando-XRD-Messungen untersuchen wir die strukturelle Entwicklung von Materialien vom Typ P3. Im Folgenden wird die Core-Shell-Lösung vom P3-Typ $\text{Na}_{0.67}\text{Mn}_{0.67}\text{Ni}_{0.33}\text{O}_2$ als Kathode für schnell zyklische Natriumionenbatterien verwendet. Die zyklische Retention von P3-Material mit Core-Shell-Struktur beträgt nach 1500 Zyklen schnellem Laden und Entladen 89%. Mit XAS untersuchen wir den Redoxmechanismus von Mn und Ni während des schnellen und langsamen Zyklus. Der

Grund für eine bessere Zyklenleistung des Kern-Schale-Materials vom P3-Typ wird unter dem Gesichtspunkt lokaler Strukturänderungen um Mn und Ni weiter untersucht.

Acknowledgements

I would like to thank my advisor Prof. John Banhart for giving me an opportunity to finish my PhD at Technische Universität Berlin and Helmholtz-Zentrum Berlin. I also thank Prof. Martin Winter for being the second evaluator of my thesis. I would like to express my sincere gratitude to Prof. Gerhard Schumacher, who supported my idea and created any opportunities for me as he can. I thank Dr. Jie Li and Prof. Jun Wang for introducing me into the field of sodium ion batteries.

I would like to thank Dr. De Ning, Dr. Anna Manzoni, Dr. Fanxing Xi, Dr. Yajie Wang, Dr. Melanie Paulisch, Dr. Götz Schuck, Dr. Ivo Zizak, Jinke Li and Christiane Förster for their assistance of my experiments. I would like to thank my colleagues Dr. Andrea Fantin, Dr. Tobias Scherb, Dr. Meng Liu, Xingpu Zhang, Kang Dong, Qin Tan and Zi Yang for their kind assistance on numerous of scientific and other occasions. I would like to thank other members of the institute such as Claudia Leistner and Jörg Bajorat for their help in my work. My special thanks go to Mrs. Christiane Ciceron for her patience in helping me with all paper-work throughout my Ph.D.

I would thank my closest companions, Ying Luo, Zheng Wang, Qianning Guo, Dr. Chunmei Liu, Dr. Xi Xiao, Yujie Tan, Lu Chen and Yueting Zhou, who offer me support and encouragement to be myself.

Finally, I would like to convey my deepest gratitude to my parents for their persistent efforts and enormous love. Without their understanding and sacrifice, I cannot reach so far. I also thank my sister, Yaping Jiang, for taking care of my parents and reducing my annoyance.

Contents

| | |
|--|-----|
| Abstract | VII |
| Kurzfassung..... | IX |
| Acknowledgements | XI |
| 1 Introduction..... | 1 |
| 1.1 Materials for sodium ion batteries | 2 |
| 1.1.1 Cathodes for sodium ion batteries | 2 |
| 1.1.2 Anodes for sodium ion batteries | 5 |
| 1.1.3 Electrolytes for sodium ion batteries | 7 |
| 1.2 Structure investigations of cathodes in sodium ion batteries | 8 |
| 1.2.1 X-ray diffraction and neutron diffraction | 9 |
| 1.2.2 X-ray absorption spectroscopy | 9 |
| 1.2.3 Others..... | 10 |
| 1.3 Structural stability of cathodes for sodium ion batteries | 11 |
| 1.4 Motivation of the thesis and outline | 12 |
| 2 Experimental..... | 13 |
| 2.1 Synthesis..... | 13 |
| 2.1.1 Synthesis of P2-type $\text{Na}_{0.67}\text{Mn}_{0.67}\text{Ni}_{0.33}\text{O}_2$ | 13 |
| 2.1.2 Synthesis of P3-type $\text{Na}_{0.67}\text{Mn}_{0.67}\text{Ni}_{0.33}\text{O}_2$ without core-shell structure | 13 |
| 2.1.3 Synthesis of P3-type $\text{Na}_{0.67}\text{Mn}_{0.67}\text{Ni}_{0.33}\text{O}_2$ with core-shell structure | 14 |
| 2.2 Characteristics | 16 |
| 2.3 Electrochemistry..... | 17 |
| 2.4 <i>Ex situ</i> XAS | 18 |
| 2.5 <i>Operando</i> XRD | 21 |
| 3 P3-type $\text{Na}_{0.67}\text{Mn}_{0.67}\text{Ni}_{0.33}\text{O}_2$ for sodium ion batteries | 22 |
| 3.1 Motivation | 22 |
| 3.2 Results | 23 |
| 3.2.1 Characteristics..... | 23 |
| 3.2.2 Electrochemistry | 25 |
| 3.2.3 XANES | 28 |

| | | |
|-------|---|----|
| 3.2.4 | EXAFS | 30 |
| 3.2.5 | Local structure in P3-type $\text{Na}_{0.67}\text{Mn}_{0.67}\text{Ni}_{0.33}\text{O}_2$ | 32 |
| 3.3 | Discussion | 36 |
| 3.4 | Conclusions | 43 |
| 4 | Core-shell design in P3-type $\text{Na}_{0.67}\text{Mn}_{0.67}\text{Ni}_{0.33}\text{O}_2$ | 44 |
| 4.1 | Motivation | 44 |
| 4.2 | Results | 45 |
| 4.2.1 | Characteristics..... | 45 |
| 4.2.2 | Electrochemistry | 48 |
| 4.2.3 | Operando XRD | 52 |
| 4.3 | Discussion | 55 |
| 4.4 | Conclusions | 60 |
| 5 | Fast charge and discharge in P3-type $\text{Na}_{0.67}\text{Mn}_{0.67}\text{Ni}_{0.33}\text{O}_2$ | 62 |
| 5.1 | Motivation | 62 |
| 5.2 | Results | 63 |
| 5.2.1 | Characteristics..... | 63 |
| 5.2.2 | Electrochemistry | 66 |
| 5.2.3 | XANES | 69 |
| 5.2.4 | EXAFS..... | 71 |
| 5.3 | Discussion | 77 |
| 5.4 | Conclusions | 81 |
| 6 | Conclusions..... | 82 |
| 7 | Outlook | 84 |
| 8 | Reference | 85 |

1 Introduction

At present, lithium ion batteries are the most successfully commercialized secondary batteries which partly replace fossil fuels and power the electronics and electric vehicles^[1]. However, the limited distribution and reserve of lithium resources as well as the rapidly growing demand for lithium ion batteries have exacerbated the imbalance between supply and demand which leads to increase in price of lithium. Hence, the exploration of low cost secondary battery systems is urgently to be carried out.

In consideration of the low price of sodium resources, the wide distribution of sodium reserves and the suitable redox potential of sodium, the sodium ion battery is one of the most promising energy storage systems, especially for large scale storage applications. Similar to lithium ion batteries, sodium ion batteries mainly consist of cathode, anode, electrolyte, separator and current collector. The preparation costs of cathode and electrolyte can be saved by replacing Li precursor and salt with inexpensive Na precursors and salt, respectively. Due to the lack of alloy formation between Al and Na, the Cu current collector of sodium ion batteries can be replaced with Al current collector which decreases preparation cost of sodium ion batteries by 8%^[2].

The chemical potential difference between the cathode and the anode of sodium ion batteries creates a voltage on the cell. Sodium ions diffuse from the cathode to the anode during charge and return back during discharge^[3]. The energy density and the cycling life are two main properties of batteries. Although the energy density of sodium ion batteries is smaller than that of lithium ion batteries, the drawback of low energy density can be compensated by increasing the dimension of batteries. Hence, the cycling performance is the most critical property of sodium ion battery materials^[4]. Due to the larger ionic radii of Na ions, the structural changes of cathode or anode materials are

severe during cycling of sodium ion batteries resulting in poor cycling performance in comparison with lithium ion batteries^[5, 6].

In this chapter, we present some common materials for sodium ion batteries under the category of cathodes, anodes and electrolytes, introduce the common techniques of structure investigation and present effective methods to improve the cycling performance of sodium ion battery materials by special structure design.

1.1 Materials for sodium ion batteries

1.1.1 Cathodes for sodium ion batteries

The specific capacity, the cycling life and the cost of preparation and safety are the relevant properties of cathode materials for sodium ion batteries to evaluate the feasibility of practical utilization. According to thermo-dynamical knowledge, the specific capacity of cathode materials is determined by the molecular weight and the electron-transfer number. Currently, the specific capacities of cathodes for sodium ion batteries are 120 - 230 mAh·g⁻¹ in different operating potential ranges^[3, 7, 8]. The cycling performance of cathode materials for sodium ion batteries is mainly determined by their structural stability and recoverability.

Cathodes for sodium ion batteries can be categorized into inorganic and organic types and demonstrate different mechanisms during cycling. One of the most extensively investigated inorganic cathodes for sodium ion batteries is layered Na_xTMO₂ (0 < x ≤ 1, *TM* = transition metal) with the nomenclature by Delmas^[9]. Layered Na_xTMO₂ cathodes can be categorized into P2, P3 and O3 types, in which “P” and “O” represent Na atoms, respectively, occupy at the center of prismatic and octahedral sites and the numbers, “2” and “3”, stand for the number of TMO₂ layers in each unit cell. The schematic structures of P2-, O3- and P3-type Na_xTMO₂ are shown in Fig.1.1^[5].

The crystal structure of layered Na_xTMO₂ is affected by the concentration of Na, the type of *TM* atoms, the ratio between different types of *TM* atoms, the synthesis temperature and the cooling way after calcination^[10-14]. *TM* atoms in layered Na_xTMO₂ can be Mn, Fe, V, Ti, Cr, Ni, Co as well as their combination^[15-21]. Enlarging the operating voltage range to increase the capacity and improving the structure stability to prolong the cycling life are two main challenges of further development of layered Na_xTMO₂.

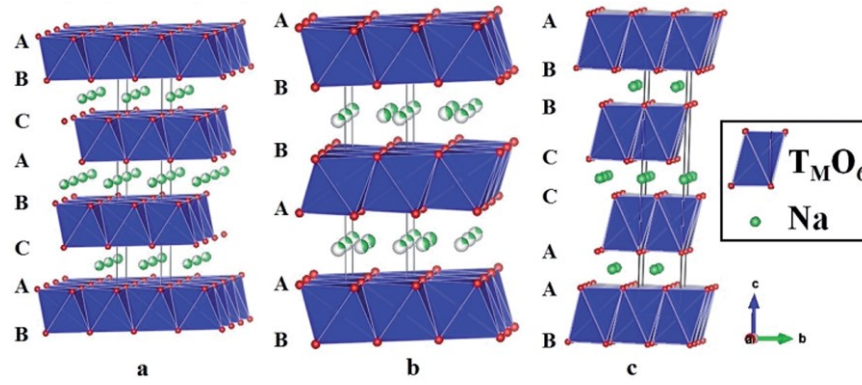


Fig. 1.1 Schematic structure images of O3- (a), P2- (b) and P3- (c) type of layered Na_xTMO_2 ^[5]

Similar to the composition of layered Na_xTMO_2 , tunnel Na_xTMO_2 materials, like $\text{Na}_{0.44}\text{MnO}_2$, $\text{Na}_{0.61}\text{Ti}_{0.48}\text{Mn}_{0.52}\text{O}_2$ and $\text{Na}_{0.61}\text{Mn}_{0.27}\text{Fe}_{0.34}\text{Ti}_{0.39}\text{O}_2$, are another type of inorganic cathodes for sodium ion batteries^[22-25]. Fig. 1.2 schematically illustrates the orthorhombic crystal structure of tunnel Na_xTMO_2 materials^[26]. This structure is built up based on double and triple rutile-type chains of edge-sharing MnO_6 octahedra and single chains of corner-sharing MnO_5 square-pyramid. There are three different Na sites in Fig. 1.2. These Na sites are situated in the tunnels formed by MnO_6 and MnO_5 polyhedrons. Unlike layered Na_xTMO_2 materials, tunnel Na_xTMO_2 materials are stable in aqueous solutions during cycling and have attracted great interest in terms of their safety.

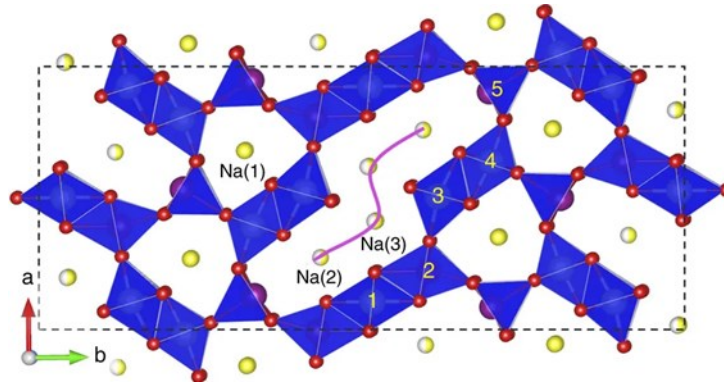


Fig. 1.2 Schematic structure image of tunnel Na_xTMO_2 materials^[26]

The third type of inorganic cathodes for sodium ion batteries is polyanionic compounds with high operating potential, which are classified as phosphates, pyrophosphates, fluorophosphates and sulfates, schematically illustrated in Fig. 1.3^[3, 27-31]. The TM atoms inside of polyanionic compounds are generally Fe, Mn, Co and V^[32-35]. Although these cathodes have high operating potential, the low rate performance and low electron conductivity are two common drawbacks. Besides, the electrolyte decomposition of these polyanionic compounds at high operating potential should be hindered to improve their cycling performance.

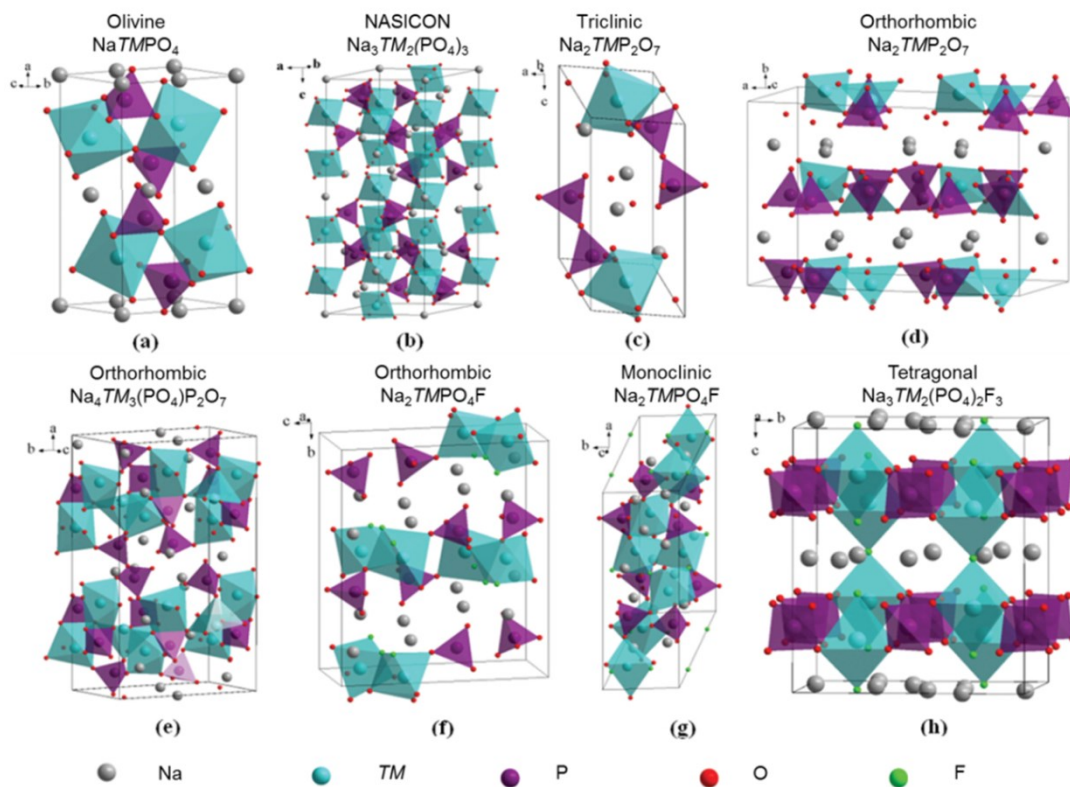


Fig. 1.3 Schematic structure images of polyanionic compounds: olivine NaTMPO_4 (a), NASICON $\text{Na}_3\text{TM}_2(\text{PO}_4)_3$ (b), triclinic $\text{Na}_2\text{TMP}_2\text{O}_7$ (c), orthorhombic $\text{Na}_2\text{TMP}_2\text{O}_7$ (d), orthorhombic $\text{Na}_4\text{TM}_3(\text{PO}_4)_2\text{P}_2\text{O}_7$ (e), orthorhombic $\text{Na}_2\text{TMPO}_4\text{F}$ (f), monoclinic $\text{Na}_2\text{TMPO}_4\text{F}$ (g), and tetragonal $\text{Na}_3\text{TM}_2(\text{PO}_4)_2\text{F}_3$ (h)^[3]

In addition, FeS_2 , FeF_3 , NaTMF_3 , Prussian blue and Prussian white, as shown in Fig. 1.4, are some other possible cathodes for sodium ion batteries. In these materials, Na atoms occupy the inter-slab vacant sites^[36-42]. Due to the lack of O in these materials, oxygen is not produced during cycling which indicates better safety of these sodium ion batteries. However, the lack of Na limits the capacity of FeS_2 and FeF_3 . NaTMF_3 delivers poor cycling performance. The operating voltage of Prussian blue and Prussian white in aqueous solutions is relative low. These properties should be considered for practical application in the future.

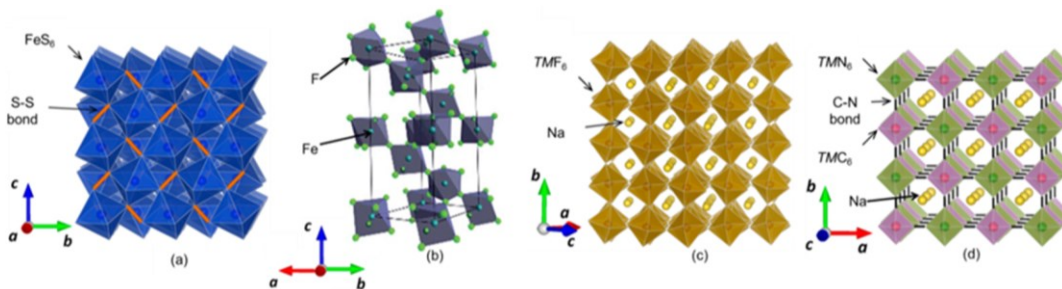


Fig. 1.4 Schematic structure images of FeS_2 (a), FeF_3 (b), NaTMF_3 (c) and Prussian blue and Prussian white (d)^[41, 42]

Aromatic carbonyl derivatives, pteridine derivatives and polymers are the main types of organic cathodes for sodium ion batteries and can also be classified into cation insertion and anion insertion types with different insertion mechanisms^[3]. During cycling of cation inserted aromatic carbonyl and pteridine derivatives, Na atoms are leased from the redox centers, which are, respectively, the carbonyl group and an isoalloxazine ring. Polymer cathodes are the main anion insertion cathodes which also demonstrate cation-inserted characteristic in a porous honeycomb material constituting of aromatic rings^[43]. Although organic cathodes for sodium ion batteries are low in cost, designable and recyclable, the drawbacks of the organic cathodes such as the low electron conductivity and severe dissolution in the electrolyte should be overcome to enlarge the capacity and prolong the cycling life of these materials.

1.1.2 Anodes for sodium ion batteries

The investigation of anodes for sodium ion batteries is inspired by that of lithium ion batteries^[44]. The structural stability, Na ion storage ability and the redox potential are the main considered properties, which are useful for increasing the energy density and prolonging the cycling life of anodes for sodium ion batteries. The specific capacities of anodes for sodium ion batteries can be a few hundred to 2500 mAh·g⁻¹ in different operating potential ranges at different currents, which are generally higher than those of cathodes for sodium ion batteries^[45, 46].

Carbon compounds, like coke and carbon black can be utilized as anodes for sodium ion batteries. The shape of carbon compounds with porous microstructure can be synthesized as tube, wire, sheet, hollow tube and hollow microsphere^[47-50]. The purpose of preparing carbon compounds in different shapes is to increase the surface-to-volume ratio for better contact with electrolyte and then improve their electrochemical performance^[51]. Recently, the investigation of carbon compounds as anode for sodium ion batteries is extensively performed on non-graphitic and graphitic types which demonstrate different insertion mechanisms of Na ions, schematically illustrated in Fig. 1.5^[52, 53].

Because of narrow interlayer spacing in graphite, the insertion of Na ions during charge of graphite is difficult and limits their capacity^[53]. In addition, carbon compounds are used as matrix and combined with other anode materials to improve the electrochemical performance of those anodes for sodium ion batteries^[45, 54-56].

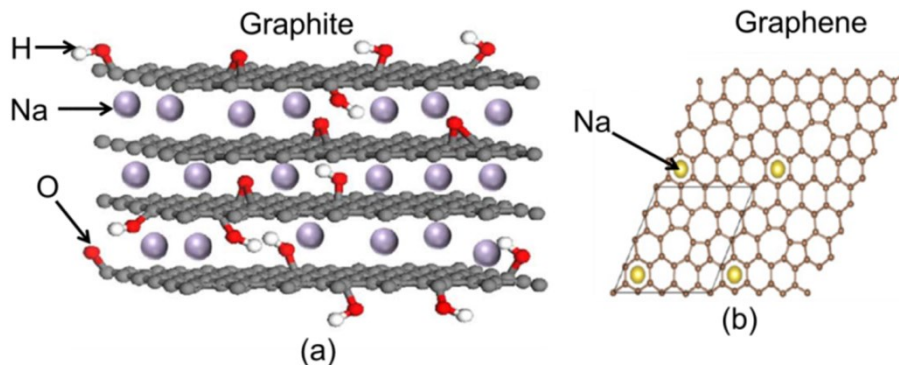


Fig. 1.5 Schematic representation of insertion of Na ions in graphite (a) and graphene (b) as anodes for sodium ion batteries^[52, 53]

Si, Ge, Sn and Sb are additional four main anodes used in current sodium ion batteries^[57-60]. During the cycling of these anodes, they have alloying reactions with Na and store Na inside. Fig. 1.6 illustrates the structural evolution of Sn during sodiation^[59]. Alloys consisting of these four materials and other metals, such as Si/Ge, Si/Sn, Sb/Al, Sb/Cu, Sb/Mo and Sn/Bi/Sb alloys, are possible to be utilized as anodes for sodium ion batteries^[61-66]. During the alloying process, the drastic volume changes lead to poor cycling performance of alloy anodes for sodium ion batteries.

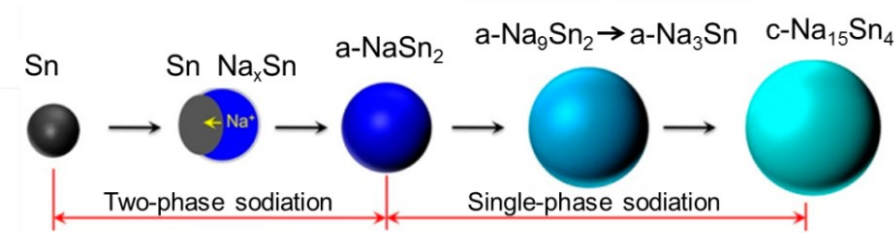


Fig. 1.6 Schematic depiction of the structural evolution of Sn during sodiation^[59]

In addition, the investigation of oxides, sulfides, phosphides and carbides, like NiCo_2O_4 , TiO_2 , MoS_2 , NiP_3 and Mo_2C , are other hot topics of exploring the optimal anodes for sodium ion batteries^[67-71]. The conversation reaction of oxides, sulfides and carbides as anodes in sodium ion batteries is expressed by the following equations with different reaction:



where TM represent transition metals, X is an anion which can be O, S and C. The subscripts, n , a and b , represent the numbers of Na, TM and X atoms. However, some common anodes for lithium ion batteries, like NiO , FeO and CoO , showed almost no electrochemical activity with $\text{Na}^{[4]}$.

Because of the appropriate redox potential of phosphorous in comparison with pure Na, phosphorous is another promising anode material which has high theoretical specific capacity ($2596 \text{ mAh}\cdot\text{g}^{-1}$) with formation of Na_3P after full sodiation^[2]. Anodes with different reaction mechanism are combined together to overcome the drawbacks of low capacity and huge volume changes and improve the electrochemical performance of sodium ion batteries.

1.1.3 Electrolytes for sodium ion batteries

Electrolytes for sodium ion batteries are the medium for Na transport between cathodes and anodes. They consist of solvent, sodium salt and some additives^[74]. The common electrolytes for sodium ion batteries can be categorized into five types, like non-aqueous liquid electrolytes, ionic liquid electrolytes, glass ceramic electrolytes, solid polymer electrolytes and gel polymer electrolytes^[75]. The basic properties of electrolytes for sodium ion batteries, such as high ionic conductivity, low viscosity, large electrochemical window, good thermal stability and low toxicity, can be optimized by variation of the constituents of the sodium salt, solvents, additives and their respective ratios^[76, 77]. The total ionic conductivity is expressed as the sum over the number of charge carriers, the relevant mobility and the charge of the carriers. Due to the smaller charge/radius ratio of Na ions in comparison with Li ions, the solvation shell and the total binding energies of Na ions are smaller providing larger mobility and higher feasibility of rapid transport of Na ions^[78].

The non-aqueous liquid electrolytes have been commercialized for sodium ion batteries. The common compounds of solvents for non-aqueous liquid electrolytes are propylene carbonate (PC), ethylene carbonate (EC), diethyl carbonate (DEC) and dimethyl carbonate (DMC). They are shown as molecular plots in Fig. 1.7^[44, 74, 79-81].

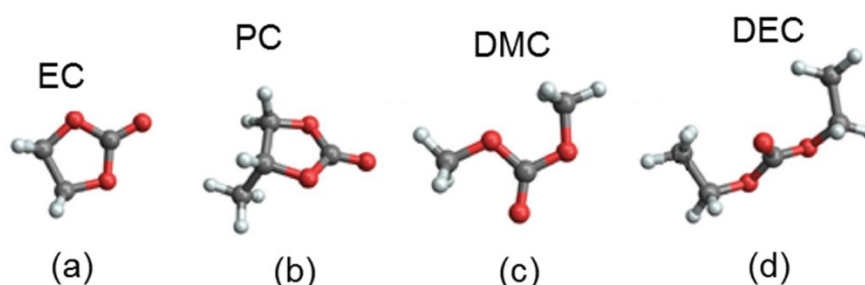


Fig. 1.7 Schematic depiction of molecular structure of solvents as non-aqueous electrolyte for sodium ion batteries: ethylene carbonate (a), Propylene carbonate (b), dimethyl carbonate (c) and diethyl carbonate (d)^[74]

On the other hand, the ionic liquids, which are made up of medium or large organic cations and weakly coordinating anions, are investigated as solvents for sodium ion batteries. Their molecular formula is $\text{Na}_x\text{Cation}_{1-x}\text{WCA}$ ($0.1 < x < 0.25$). The molecular structures of the two most common ionic liquid cations are schematically illustrated in Fig. 1.8^[77]. The non-flammability is the most attractive advantage of ionic liquid solvents as electrolyte for sodium ion batteries. However, the high viscosity is a result of the complex and strong ion-ion interactions and decreases the mobility of Na ions during cycling. In order to improve the mechanical stability of sodium ion batteries, the solid polymer electrolytes and gel polymer electrolytes are investigated without any separator in the cell. The poor interfacial contact between the electrolytes and the electrodes, the low conductivities, the high viscosity and the low dielectric constants are the main drawbacks hindering their practical utilization as electrolyte for sodium ion batteries.

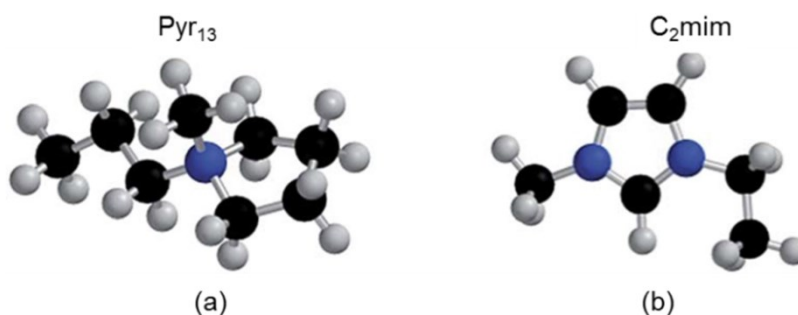


Fig. 1.8 Schematic depiction of the molecular structure of two most common ionic liquid cations employed in electrolytes for sodium ion batteries: Pyr₁₃ (a) and C₂mim (b)^[77]

The majority of electrolyte salts for sodium ion batteries are NaClO_4 , NaPF_6 , NaBF_4 , NaFSI and NaTFSI ^[82-85]. Fluorinated ethylene carbonate (FEC), solid electrolyte interphase (SEI) enhancer, is the most efficient and common additive in electrolyte for sodium ion batteries^[86]. However, the common effective additive for lithium ion batteries, like vinylene carbonate (VC), is detrimental in sodium ion batteries^[79].

1.2 Structure investigations of cathodes in sodium ion batteries

In sodium ion batteries, Na ions are extracted from the cathodes during charge and inserted into the cathodes during discharge. With the extraction and insertion of Na, *TM* or other compositions in cathodes are oxidized and reduced, respectively. This leads to structural changes and affects the cycling performance of cathodes during the cycling. Hence, the investigation of the crystal structure, the occupancy of atoms and the structural evolution of cathode materials is efficient and effective for better

understanding of electrochemical performance of them as cathodes and anodes for sodium ion batteries.

1.2.1 X-ray diffraction and neutron diffraction

X-ray diffraction (XRD) is a common method to investigate the crystal structure of cathodes for sodium ion batteries. Using XRD technique, we obtain structure information like the symmetry of elements, the occupancy of atoms, the lattice parameters as well as the displacement of atoms^[14, 87]. The positions of diffraction peaks in XRD patterns provide information of interatomic distance, while the atom types and positions determine the intensities of diffraction peaks. The understanding of crystal structure of materials for sodium ion batteries is the basis for investigation of structure evolution of cathodes during cycling. Recently, the structure evolution during cycling of cathodes has been extensively investigated by *operando* XRD. Fig. 1.9 demonstrates an example of *operando* XRD measurements of cathode for sodium ion batteries along with the charge and discharge curves^[88].

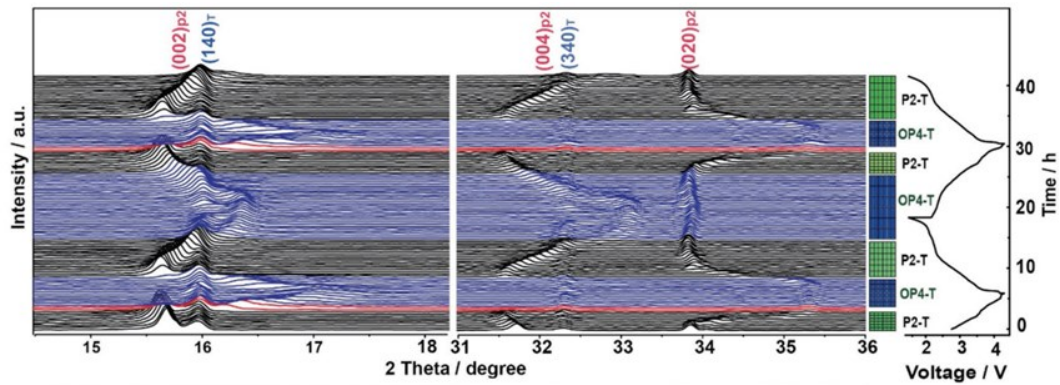


Fig. 1.9 *Operando* X-ray diffraction patterns collected during cycling of $\text{Na}_{0.6}\text{MnO}_2$ electrode in the voltage range 1.5 and 4.3 V ^[88]

During charge and discharge, the appearance and disappearance of reflection peaks indicate the phase transitions of cathode materials. By refining of XRD results, the expansion and shrinkage of particles within the *a-b* plane and along the *c* axis are reflected by changes of lattice parameters. However, the preparation of cells for *operando* XRD measurement is relatively complicated.

1.2.2 X-ray absorption spectroscopy

X-ray absorption spectroscopy (XAS) is a synchrotron-based characterization technique which consists of X-ray absorption near edge structure (XANES) and extended X-ray absorption fine structure (EXAFS)^[89]. Fig. 1.10 is an example of XANES and EXAFS

spectra at Ni K-edge in sodium ion battery material at different charge and discharge states^[90].

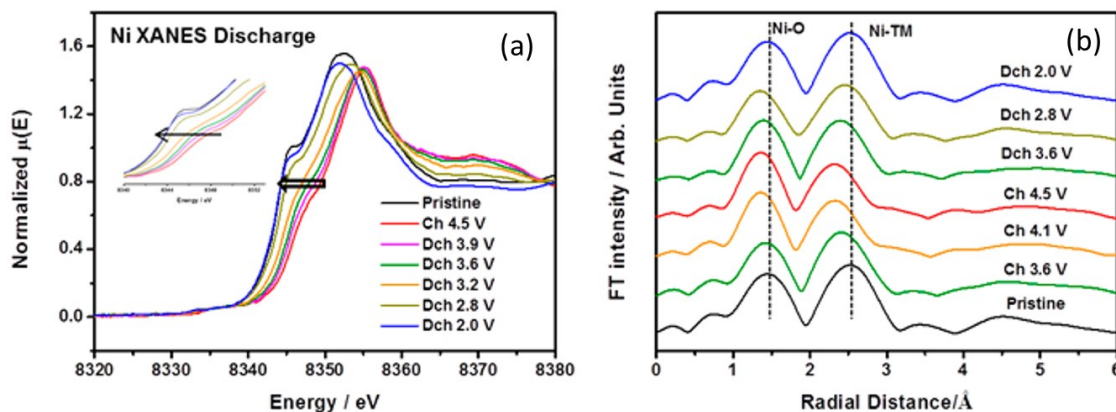


Fig. 1.10 Normalized X-ray absorption near edge spectra (a) and extended X-ray absorption fine structure spectra after Fourier transform (b) of $\text{Na}_{0.78}\text{Ni}_{0.23}\text{Mn}_{0.69}\text{O}_2$ at Ni K-edge at different charge and discharge states^[90]

In Fig. 1.10(a), the pre-edge of each spectrum at Ni K-edge representing the photoelectron transition from 1s to 3d orbital is unobvious. Sometimes, the pre-edge of XANES spectra splits into two peaks caused by the crystal field and the core hole effect^[91, 92]. The main peak of the K-edge is a result of photoelectron transition from the 1s to the 4p orbital of 3d transition metals. The changes in energy position are called energy shift and provide information about changes in valence state^[93]. The higher energy of the main peak indicates a higher valence state. When a core electron absorbs the energy of a photon, this electron is excited to an empty orbital. In the EXAFS region, this excited electron has significant kinetic energy which provides accurate information of local geometry. The shape of X-ray absorption spectra is described by the Fermi's Golden Rule. Fig. 1.10(b) provides local structure information around Ni, such like the type of coordinated atoms, the coordination number, the interatomic distance and the distortion of crystal lattice^[94, 95].

1.2.3 Others

Except the investigation of the crystal structure by XRD and the local structure by XAS, imaging techniques, like scanning electron microscopy (SEM) and transmission electron microscopy (TEM) are utilized to visually demonstrate the morphology of materials for sodium ion batteries. A focused ion beam (FIB) is applied to cut the particles of cathodes. In combination of energy dispersive X-ray (EDX) spectroscopy and SEM, the

concentration and distribution of elements in cross section is investigated in cathodes for sodium ion batteries.

1.3 Structural stability of cathodes for sodium ion batteries

As we mentioned in the beginning, the capacities of sodium ion batteries can be improved by increasing their volume. Hence, the cycling performance is the key to the practical utilization of sodium ion batteries. In order to obtain better cycling performance of sodium ion batteries, the structural stabilities of cathodes has to be urgently improved.

On the one hand, extraction and insertion of Na lead to changes in electrostatic interaction between Na and other atoms. This is responsible for expansion and shrinkage of cathodes during cycling. That means, hindering the dimensional change of cathode particles can improve the cycling performance of sodium ion batteries. Surface modification, such like coating with Al_2O_3 or carbon on the surface of cathode particles, is one common method to hinder the expansion of cathode particles and lead to better cycling performance of sodium ion batteries^[96-98].

On the other hand, insertion and extraction of Na accompany the oxidation and reduction of transition metals or other atoms in cathodes during cycling. The structural changes of compositions with high redox activity are supposed to be larger than low redox activity compositions. Hence, substitution or doping affects the redox activity of different elements which is also effective to improve structural stability of cathodes during cycling. For layered Na_xTMO_2 , the common elements suitable for substitution or doping are Al, Cu, Mg, Zn and Ti^[87, 99-103].

A core-shell design is a potential method to improve the structural stability of cathodes for sodium ion batteries. The core-shell designed materials consist of a core with high redox activity material contributing the capacity and a shell with low redox activity material stabilizing the structure. The concentration of transition metals gradually changes from the core to the shell. The gradient core-shell design has been confirmed as a powerful way for the inhibition of capacity fading during cycling of LiTMO_2 materials^[104-107]. However, the core-shell design in layered Na_xTMO_2 has never been reported.

According to Wang's investigation, selecting *TM* ions with similar ionic radii to obtain the disordered arrangement of *TM* ions in P2-type Na_xTMO_2 has a positive impact on improving the cycling performance of sodium ion batteries^[108].

1.4 Motivation of the thesis and outline

The main goals of this thesis are to decrease the preparation cost of layered cathodes for sodium ion batteries, to figure out the reason for cycling fading in layered cathodes, to improve the structural stability of layered cathodes and to utilize the improved layered cathode for ultrafast sodium ion batteries.

This thesis begins with a brief introduction of sodium ion batteries. This is followed by a detailed introduction of synthesis of P3-type $\text{Na}_{0.67}\text{Mn}_{0.67}\text{Ni}_{0.33}\text{O}_2$ materials and relevant electrochemical measurements and structure analysis measurements, like SEM, TEM, XRD and XAS. The correlation between electrochemical performance and structural evolution of P3-type $\text{Na}_{0.67}\text{Mn}_{0.67}\text{Ni}_{0.33}\text{O}_2$ materials was investigated in this thesis.

2 Experimental

2.1 Synthesis

2.1.1 Synthesis of P2-type $\text{Na}_{0.67}\text{Mn}_{0.67}\text{Ni}_{0.33}\text{O}_2$

P2-type $\text{Na}_{0.67}\text{Mn}_{0.67}\text{Ni}_{0.33}\text{O}_2$ samples were prepared by a solid-state reaction using mixed transition metal hydroxide precursors and sodium carbonate (98%, Aldrich). The transition metal hydroxide precursors were prepared by the co-precipitation method. Manganese (II) nitrate solution (50%, Alfa Aesar) and nickel (II) nitrate hexahydrate (98%, Alfa Aesar) ($M_{\text{Mn}}/M_{\text{Ni}} = 2:1$) were mixed in deionized water and stirred for 6 hours. This mixed solution was dropped into sodium hydroxide (98%, Alfa Aesar) solution and the dispersion was stirred for 12 hours. Then, the precipitation particles were filtered and washed with deionized water and dried overnight at 80 °C. The $\text{Mn}_{0.67}\text{Ni}_{0.33}(\text{OH})_2$ precipitate was used as precursor and mixed with stoichiometric sodium carbonate. The mixed powder was pressed into pellets and calcined at 950 °C for 12 hours to obtain P2-type $\text{Na}_{0.67}\text{Mn}_{0.67}\text{Ni}_{0.33}\text{O}_2$, respectively. Finally, the obtained materials were cooled to room temperature, grinded in air and stored in a glove box.

2.1.2 Synthesis of P3-type $\text{Na}_{0.67}\text{Mn}_{0.67}\text{Ni}_{0.33}\text{O}_2$ without core-shell structure

In this thesis, three different P3-type $\text{Na}_{0.67}\text{Mn}_{0.67}\text{Ni}_{0.33}\text{O}_2$ materials without core-shell structure were prepared by a solid-state reaction using mixed transition metal hydroxide precursors and sodium carbonate (98%, Aldrich).

The first P3-type $\text{Na}_{0.67}\text{Mn}_{0.67}\text{Ni}_{0.33}\text{O}_2$ (P3-MN-1) was investigated in chapter 3. The transition metal hydroxide precursors of this P3-type material were prepared by Manganese (II) nitrate solution (50%, Alfa Aesar) and nickel (II) nitrate hexahydrate

(98%, Alfa Aesar) using the same preparation processed with those of P2-type $\text{Na}_{0.67}\text{Mn}_{0.67}\text{Ni}_{0.33}\text{O}_2$ in section 2.1.1. However, the mixed transition metal hydroxide precursors and sodium carbonate were calcined at 750 °C for 12h.

The similar method described in section 2.1.1 was utilized to prepare the second P3-type $\text{Na}_{0.67}\text{Mn}_{0.67}\text{Ni}_{0.33}\text{O}_2$ (P3-MN-2), which was investigated in chapter 4. Manganese (II) acetate tetrahydrate (98%, Alfa Aesar), nickel (II) acetate tetrahydrate (98%, Alfa Aesar) and sodium hydroxide (98%, Alfa Aesar) were used as raw materials to prepare the hydroxide precursors. The mixed transition metal hydroxide precursors and sodium carbonate were calcined at 700 °C for 24h.

The third P3-type $\text{Na}_{0.67}\text{Mn}_{0.67}\text{Ni}_{0.33}\text{O}_2$ (P3-MN-3) was investigated in chapter 5. The difference between the second and the third P3-type materials was the raw materials. Manganese (II) nitrate solution (50%, Alfa Aesar) and nickel (II) nitrate hexahydrate (98%, Alfa Aesar) were utilized to prepare the transition metal hydroxide.

2.1.3 Synthesis of P3-type $\text{Na}_{0.67}\text{Mn}_{0.67}\text{Ni}_{0.33}\text{O}_2$ with core-shell structure

In this thesis, we prepared two different core-shell designed P3-type materials. The first core-shell designed P3-type $\text{Na}_{0.67}\text{Mn}_{0.67}\text{Ni}_{0.33}\text{O}_2$ (P3-1-CS) was synthesized as following. Firstly, manganese (II) acetate tetrahydrate (98%, Alfa Aesar) and nickel (II) acetate tetrahydrate (98%, Alfa Aesar) were dissolved into deionized water with a Mn:Ni molar ratio of 2:1 and stirred for 1 hour. And then, the solution of manganese (II) acetate and nickel acetate was used as raw material to prepare mixed solutions with Mn:Ni molar ratios of 1:4, 2:1 and 11:2, respectively. These three solutions were stirred for 1 hour. The high Ni solution with the Mn:Ni molar ratio of 1:4 was dropped into sodium hydroxide solution and the dispersion was stirred for 3 hours. Then, the solution with the Mn:Ni molar ratio of 2:1 was dropped into the dispersion and the obtained dispersion was stirred for 3 hours. Finally, the solution with the Mn:Ni molar ratio of 11:2 was dropped into the dispersion and the obtained dispersion was stirred for 6 hours. All these steps were finished in the air. The schematic preparation processes of the core-shell designed precursors are illustrated in Fig. 2.1. The obtained precipitation particles were filtered and washed with deionized water and dried overnight at 80 °C. The core-shell designed $\text{Mn}_{0.67}\text{Ni}_{0.33}(\text{OH})_2$ precipitates were used as precursors and mixed with stoichiometric sodium carbonate (98%, Aldrich), respectively. The mixed powders were pressed into pellets and calcined at 700 °C for 24 hours to obtain the P3-type $\text{Na}_{0.67}\text{Mn}_{0.67}\text{Ni}_{0.33}\text{O}_2$ with core-shell structure. Finally, the obtained materials were

cooled to room temperature, grinded in air and stored in a glove box. This special P3-type material was investigated in chapter 4.

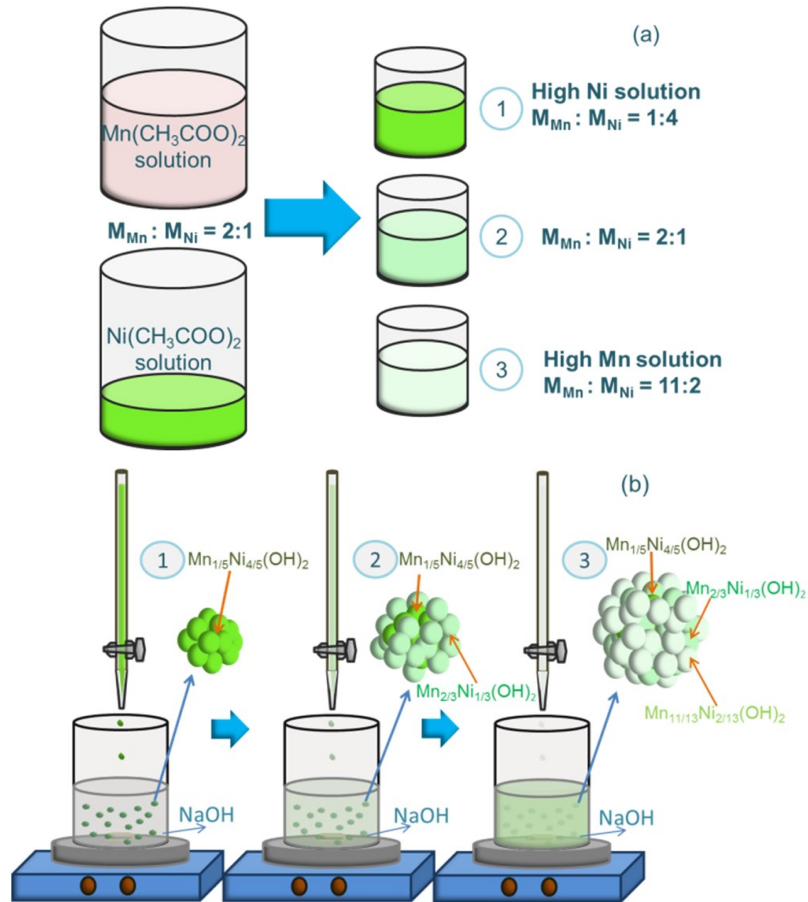


Fig. 2.1 Schematic preparation of first type of precursor for P3-type $Na_{0.67}Mn_{0.67}Ni_{0.33}O_2$ with core-shell structure: mixture of transition metal solutions with different molar ratios between Mn and Ni (a) and co-precipitation of the core-shell designed hydroxide precursor (b)

The second core-shell designed P3-type $Na_{0.67}Mn_{0.67}Ni_{0.33}O_2$ (P3-2-CS) was synthesized in the following. Manganese (II) nitrate solution (50%, Alfa Aesar) and nickel (II) nitrate hexahydrate (98%, Alfa Aesar), sodium hydroxide (98%, Alfa Aesar) and sodium carbonate (98%, Aldrich) were used as raw materials to prepare the special transition metal hydroxide precursors. In order to simplify the preparation process, we only prepared the core-shell designed precursor in two steps. Manganese (II) nitrate solution and nickel (II) nitrate were, respectively, dissolved in deionized water with a Mn:Ni molar ratio of 2:1 and stirred for 1 hours. Then, these two separate solutions were used to prepare two mixed solutions with Mn and Ni molar ratio of 1:6 and 13:1, respectively. These two mixed solutions were stirred for 1 hour. The mixed solution with a Mn:Ni molar ratio of 1:6 was dropped into sodium hydroxide (98%, Alfa Aesar) solution and the dispersion was stirred for 3 hours. Then, the mixed solution with a Mn:Ni molar

ratio of 13:1 was dropped into the previously obtained dispersion. Then, the obtained dispersion was stirred for another 9 hours. Fig. 2.2 schematically illustrates the preparation of the second type of precursor for P3-type $\text{Na}_{0.67}\text{Mn}_{0.67}\text{Ni}_{0.33}\text{O}_2$ with core-shell structure.

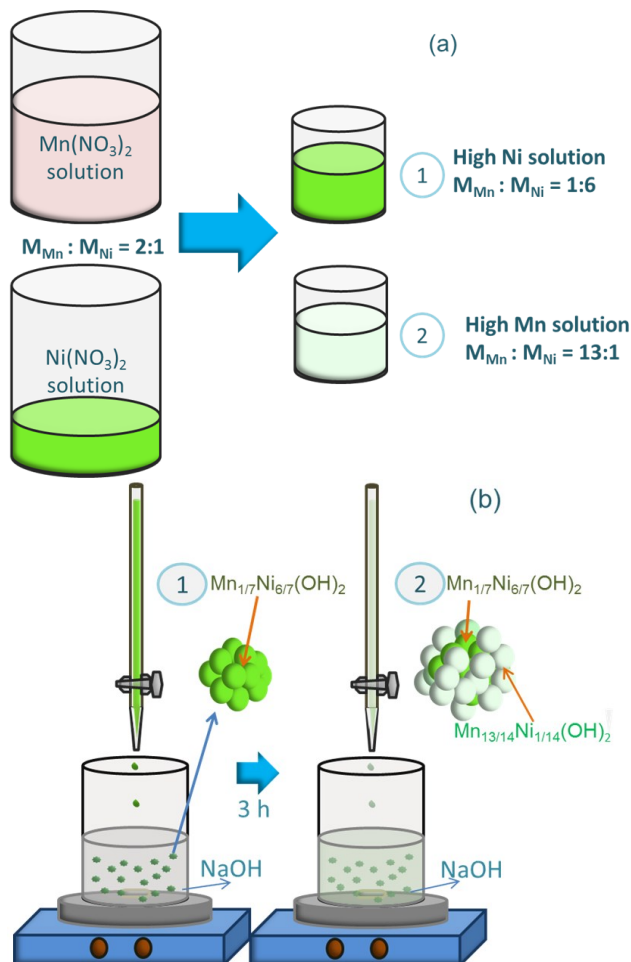


Fig. 2.2 Schematic preparation of the second type of precursor for P3-type $\text{Na}_{0.67}\text{Mn}_{0.67}\text{Ni}_{0.33}\text{O}_2$ with core-shell structure: mixture of transition metal solutions with different molar ratios between Mn and Ni (a) and co-precipitation of the core-shell designed hydroxide precursor (b)

Then obtained designed precipitation particles were filtered and washed with deionized water and dried overnight at 80 °C. The core-shell designed $\text{Mn}_{0.67}\text{Ni}_{0.33}(\text{OH})_2$ precipitates were used as precursors and mixed with stoichiometric sodium carbonate (98%, Aldrich). The mixed powders were pressed into pellets and calcined at 700 °C for 24 hours to obtain the second type of core-shell designed P3-type $\text{Na}_{0.67}\text{Mn}_{0.67}\text{Ni}_{0.33}\text{O}_2$. Finally, the obtained materials were cooled to room temperature, grinded in air and stored in a glove box. P3-2-CS material is investigated in chapter 5.

2.2 Characteristics

The morphology of different types of $\text{Na}_{0.67}\text{Mn}_{0.67}\text{Ni}_{0.33}\text{O}_2$ was measured by scanning electron microscopy from ZEISS operated at acceleration voltage of 5 kV. Transmission electron microscopy (TEM) images were recorded in a Philips CM30 microscope operated at 300 kV and equipped with an energy dispersive X-ray (EDX) detector. Focused ion beam (ZEISS Crossbeam 340) was performed to demonstrate the core-shell structure in P3-type $\text{Na}_{0.67}\text{Mn}_{0.67}\text{Ni}_{0.33}\text{O}_2$ materials.

Powder X-ray diffraction (XRD) was carried out on a Bruker D8 advance in the 2θ range from 10° to 90° using Cu $K\alpha$ radiation. The XRD data of different types of $\text{Na}_{0.67}\text{Mn}_{0.67}\text{Ni}_{0.33}\text{O}_2$ was refined using the Fullprof program and Rietveld method. High-temperature XRD measurements were carried out from 650°C to 950°C (Bruker D8 advance with a furnace) in the 2θ range from 10° to 90° using Cu $K\alpha$ radiation. The XRD patterns were collected at increasing temperature every 10°C . The sample for high-temperature XRD measurements was a pellet which was produced from the precursor of the first P3-type material without core-shell design.

2.3 Electrochemistry

In order to prepare the electrode, the obtained P2-type and P3-type $\text{Na}_{0.67}\text{Mn}_{0.67}\text{Ni}_{0.33}\text{O}_2$ materials together with conductive carbon (TIMCAL Super P) and polyvinylidene difluoride (PVdF, ARKEMA KYNAR®) binder, (weight ratio 80:10:10) was mixed in 1-methyl-2-pyrrolidinone (NMP, ACROS Organics) and cast onto Al foil, respectively. After being dried, the electrode tapes were punched into discs with 12 mm diameter, pressed in a hydraulic press, and dried at 120°C under vacuum overnight. 2032-type coin cells were assembled in Ar-filled glove box using 1 M NaPF_6 in ethylene carbonate to dimethyl carbonate (EC:DMC = 1:1 in weight) with 1 wt.% fluoroethylene carbonate (FEC) as the electrolyte. The mass loading of the active material was around $3\text{ mg}\cdot\text{cm}^{-2}$. Metallic sodium served as counter electrode. All measurements were repeated 3 times for each state.

The electrochemical tests for chapter 3 were performed at 20°C in the following way. The cells of P2-type $\text{Na}_{0.67}\text{Mn}_{0.67}\text{Ni}_{0.33}\text{O}_2$ and P3-MN-1 were galvanostatically charged and discharged using Maccor series 4000 battery testers (USA) at 0.1 C rate (nominal current density $1\text{ C} = 100\text{ mA}\cdot\text{g}^{-1}$) in the first 3 cycles and 1 C rate from the 4th to 120th cycles in the voltage range 1.5 - 4.5 V. The rate capabilities of P2-type and P3-type $\text{Na}_{0.67}\text{Mn}_{0.67}\text{Ni}_{0.33}\text{O}_2$ were tested at constant charge rate of 0.1 C and different discharge

rate of 0.1 C, 0.2 C, 0.5 C, 1C, 2 C, 5 C, 10 C, 20 C and 0.1 C each for 5 cycles in voltage range 1.5 - 4.5 V.

In the following, the cells of P3-MN-2 and P3-1-CS were galvanostatically charged and discharged at 0.1 C rate in the first 3 cycles and 1 C rate from the 4th to 200th cycles in the voltage range 1.5 - 4.5 V and from the 4th to 250th cycles in the voltage range 2.0 - 4.1 V in comparison with the second type of P3-type material without core-shell structure. These two different P3-type $\text{Na}_{0.67}\text{Mn}_{0.67}\text{Ni}_{0.33}\text{O}_2$ were cycled at 0.1 C rate for three cycles and then cycled at charge rate of 0.1 C and discharge rate of 20 C from the 4th to 400 cycles as well as charge rate of 20 C and discharge rate of 20 C from the 4th to 1000 cycles in the voltage range 2.0 - 4.1 V. The rate capabilities of the normal and the gradient core-shell designed P3-type $\text{Na}_{0.67}\text{Mn}_{0.67}\text{Ni}_{0.33}\text{O}_2$ were tested at constant charge rate of 0.1 C and different discharge rate of 0.1 C, 0.2 C, 0.5 C, 1C, 2 C, 5 C, 10 C, 20 C and 0.1 C each for 5 cycles in voltage ranges 1.5 - 4.5 V and 2.0 - 4.1 V, respectively. These results are demonstrated in chapter 4.

In chapter 5, P3-MN-3 and P3-2-CS materials were cycled at 0.1 C for three cycles and then cycled at different charge and discharge rates in the voltage range 2.0 - 4.1 V which were charged at 1 C (1 C = 100 mA·g) and discharged at 1 C from the 4th to 350th cycles, charged at 20 C and discharged at 1 C from the 4th to 450th cycles, charged at 1 C and discharged at 20 C from the 4th to 900th cycles as well as charged at 20 C and discharged at 20 C from the 4th to 1500th cycles. The cells of P3-2-CS material were galvanostatically charged at 1 C and discharged at 1 C, charged at 20 C and discharged at 1 C, charged at 1 C and discharged at 20 C as well as charged at 20 C and discharged at 20 C in the voltage range 2.0 - 4.1 V, respectively.

2.4 Ex situ XAS

The specimens for ex situ XAS measurements were electrodes which were charged and discharged to different states in 2032 coin cells. For each charge and discharge state, two electrodes were prepared. All specimens for XAS measurement were prepared one week before the measurement in order to minimize aging of the specimens. The thickness of electrodes during preparation was kept as 150 μm . The electrodes of P2-type $\text{Na}_{0.67}\text{Mn}_{0.67}\text{Ni}_{0.33}\text{O}_2$ and P3-NM-1 were charged to 4.0 and 4.5 V and discharged to 2.0 and 1.5 V at 0.1 C (1 C = 100 mA·g⁻¹), respectively. The electrodes of P3-2-CS were charged to 4.1 V at 1 C and 20 C as well as discharged to 2.0 V at 1 C and 20 C,

respectively. Then, these electrodes are taken out of the cell in the glovebox, cleaned by DMC, stuck by Kapton tape one by one and then stored in a box filled with argon.

Ex situ XAS measurements of different types of $\text{Na}_{0.67}\text{Mn}_{0.67}\text{Ni}_{0.33}\text{O}_2$ in transmission mode at Mn and Ni K-edge were performed at KMC-2 XANES endstation at BESSY II, Helmholtz-Zentrum Berlin^[109]. Si-Ge (111) double crystal monochromator was used to monochromatize the focused X-ray beam. Energy bandwidth of the monochromator is 1/4000. To suppress the higher harmonics the second monochromator crystal was detuned to about 65% of the maximal intensity. Metallic Mn and Ni standard foils were simultaneously measured along with the samples at Mn and Ni K-edge, respectively, for the absolute energy calibration.

Evaluation of P2-type $\text{Na}_{0.67}\text{Mn}_{0.67}\text{Ni}_{0.33}\text{O}_2$, P3-MN-1 and P3-2-CS was performed using DEMETER package^[110]. The XANES data at Mn and Ni K-edge at different charge and discharge states was calibrated to 6539 and 8333 eV, respectively, and normalized using the ATHENA program. The k^3 -weighted EXAFS data of P3-type materials after the Fourier transformation was fitted using the Artemis program with different paths calculated by the FEFF program in the fitting range 1 - 5 Å. The EXAFS data at Mn and Ni K-edge of P3-type $\text{Na}_{0.67}\text{Mn}_{0.67}\text{Ni}_{0.33}\text{O}_2$ at various charged and discharged states was weighted by factors of 0.67 of P3-type $\text{Na}_{0.67}\text{MnO}_2$ and 0.33 of P3-type $\text{Na}_{0.67}\text{NiO}_2$, respectively, based on the overall stoichiometry of P3-type $\text{Na}_{0.67}\text{Mn}_{0.67}\text{Ni}_{0.33}\text{O}_2$. The crystal structure of P3-type $\text{Na}_{0.67}\text{MnO}_2$ and $\text{Na}_{0.67}\text{NiO}_2$ was determined by the Rietveld refinement of XRD data and related crystal structure information of the pristine P3-type $\text{Na}_{0.67}\text{Mn}_{0.67}\text{Ni}_{0.33}\text{O}_2$ reported in the literature^[111].

According to the equations below, the normalized oscillatory component of the absorption coefficient μ above the absorption edge is estimated^[112]:

$$\chi(k) = \frac{\mu(k) - \mu_0(k)}{\mu_0(k)} = S_0^2 \sum_j N_j \frac{F_j(k)}{k R_j^2} \sin(2k R_j + \phi_j(k)) \exp^{\frac{-2R_j}{\lambda(k)}} \exp^{-2\sigma_j^2 k^2} \quad (2.1)$$

$$k = \sqrt{\frac{2m_e(E - E_0)}{\hbar^2}} \quad (2.2)$$

In equation (1), $\mu(k)$ is the observed absorption coefficient and $\mu_0(k)$ is the free atom absorption coefficient. R_j is the distance between the absorbing atom and the j-type backscattering atoms. S_0^2 is the amplitude reduction factor. N_j is the number of j-type atoms. $F_j(k)$ is the back scattering amplitude of the j-type atoms. $\phi_j(k)$ is the overall

phase shift. $\lambda(k)$ is the inelastic mean free path of photoelectron. σ_j^2 is the mean squared relative displacement between the absorbing atom and the scattering atoms. In equation (2), m_e is the electron mass, E is the incident photon energy, E_0 is the threshold energy and \hbar is the reduced Plank's constant. In this thesis, $\chi(k)$ is multiplied by k^3 to emphasize the data at high k -range.

During the fitting of EXAFS data at Mn and Ni K-edge of the P3-MN-1 and P3-2-CS at pristine state, the calculated S_0^2 should be in the range 0.7 - 1.1 and the σ_j^2 should be larger than 0. The distance between the absorbing atom to the coordinated atoms should be consistent with the crystal structure of the corresponding materials. After fitting the EXAFS data of the pristine P3-type $\text{Na}_{0.67}\text{Mn}_{0.67}\text{Ni}_{0.33}\text{O}_2$ materials at the Mn and Ni K-edge, the calculated S_0^2 values at Mn and Ni K-edge are kept constant to calculate the distance between the absorbing atom and coordinated atoms and assess the local structural changes of these $\text{Na}_{0.67}\text{Mn}_{0.67}\text{Ni}_{0.33}\text{O}_2$ materials during the cycling.

After fitting the EXAFS data, the distance between TM and O as well as that between TM and TM are obtained and utilized to calculate the angle between TM -O bonds. Fig. 2.3 schematically demonstrates the crystal structure of P3-type Na_xTMO_2 ^[113]. In the crystal structure of P3-type material, the distance between two nearest occupied O within the a - b plane is equal to the distance between two nearest occupied TM atoms, see the green and blue triangles in Fig. 3. The blue triangle is an isosceles triangle and the green triangle is an equilateral triangle. TM atoms occupy at the center of octahedral TMO_6 units. The projection of TM into the O plane is located at the center of the green triangle, marked by a red box. In addition, the changes of distance between TM and TM are related to the dimensional changes of TMO_6 units within the a - b plane.

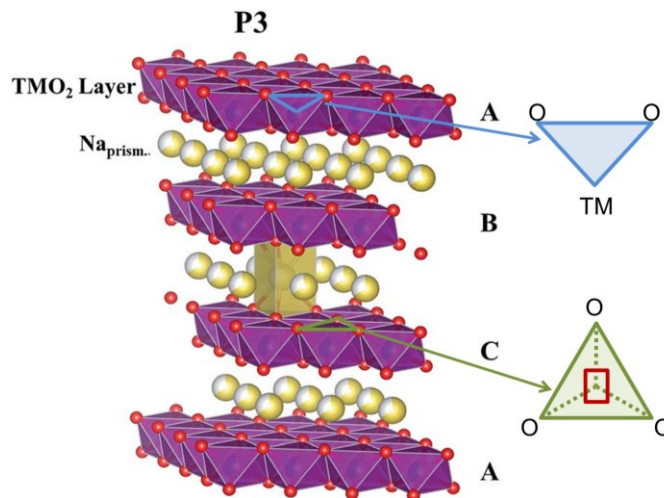


Fig. 2.3 Schematic depiction of the structure of P3-type Na_xTMO_2 ^[113]

2.5 *Operando* XRD

Operando synchrotron XRD experiment was carried out at mySpot endstation at BESSY II, Helmholtz-Zentrum Berlin^[114]. The powder diffraction pattern was acquired using the Eiger 9M area detector in Bragg geometry. The X-ray wavelength was 0.72932 Å. The sample was prepared with a special 2032 coin cell, which contained a hole ($\Phi = 10$ mm) on the positive shell covered by Kapton foil from the inner side using super AB glue, reported in detail by Wang et al.^[115]. The P3-type $\text{Na}_{0.67}\text{Mn}_{0.67}\text{Ni}_{0.33}\text{O}_2$ powder was mixed with super P and PVdF (weight ratio = 70:20:10) in NMP. The electrolyte solution was 1 M NaPF_6 in 1:1 weight ratio of EC:DMC with 1 vol.% FEC. Metal Na and glass fiber filter were used as anode and separator, respectively. The cell was charged and discharged in the voltage range of 1.5 - 4.5 V at 0.1 C at 20 °C. During the cycling of the cell, diffracted photons exited the cell through the same hole on the electrode and were reflected to the detector.

3 P3-type $\text{Na}_{0.67}\text{Mn}_{0.67}\text{Ni}_{0.33}\text{O}_2$ for sodium ion batteries

3.1 Motivation

Extensively studied P2- and O3-type Na_xTMO_2 materials are synthesized at temperature higher than 850 °C which calls for high production cost and energy expenditure^[100, 103, 116, 117]. On the contrary, P3-type and P2/P3-type Na_xTMO_2 materials demonstrating attractive electrochemical performance, e.g. P3-type $\text{Na}_{2/3}\text{Mg}_{1/3}\text{Mn}_{2/3}\text{O}_2$, P2/P3-type $\text{Na}_{0.45}\text{Ni}_{0.22}\text{Co}_{0.11}\text{Mn}_{0.66}\text{O}_2$ and P2/P3-type $\text{Na}_{0.66}\text{Co}_{0.5}\text{Mn}_{0.5}\text{O}_2$, can be produced at temperature lower than 750 °C^[113, 118, 119]. Thus, the investigation of pure P3-type Na_xTMO_2 materials resulting in a strategy to achieve sodium ion battery materials in an economic way is urgently to be carried out.

Due to the large radii of Na atoms, the poor cycling performance is common in layered Na_xTMO_2 materials^[120]. Generally, the reasons for capacity fading in P2- and O3-type Na_xTMO_2 are investigated from the sight of structure by X-ray diffraction (XRD), neutron diffraction (ND) and neutron pair distribution function (NPDF)^[121-123]. However, the influence of the structural variations of TMO_2 layers on the capacity fading is seldom reported but significant. During charge and discharge, Na ions are repeatedly extracted from and inserted into the layered Na_xTMO_2 particles accompanied by oxidation and reduction of TM and O atoms, which change the structure of TMO_6 units through the alternately electrostatic attraction and repulsion. Hence, X-ray absorption spectroscopy (XAS) providing information about local structure around TM atoms^[124] is

indispensable for better understanding of the electrochemical behavior of layered Na_xTMO_2 , especially for P3-type Na_xTMO_2 materials synthesized at lower temperature.

In addition, Wang et al. reported that the disordered arrangement of *TM* ions promotes better Na storage and cycling performance of P2-type $\text{Na}_{0.6}\text{Cr}_{0.6}\text{Ti}_{0.4}\text{O}_2$ ^[108]. This indicates the ordered arrangement of *TM* ions is responsible for the capacity fading in P2-type Na_xTMO_2 . The goal of the present chapter is to figure out the relationship between the ordered arrangement of *TM* ions and the capacity fading in P3-type Na_xTMO_2 .

In consideration of environment protection, Co-free $\text{Na}_{0.67}\text{Mn}_{0.67}\text{Ni}_{0.33}\text{O}_2$ was intentionally selected in this work. The ordered arrangement of *TM* atoms has been confirmed in $\text{Na}_{0.67}\text{Mn}_{0.67}\text{Ni}_{0.33}\text{O}_2$ by ND measurement²³. For the purpose of saving energy, the calcination temperature was fixed at 750 °C to obtain pure P3 material. The redox mechanism of Mn and Ni ions in P3-type $\text{Na}_{0.67}\text{Mn}_{0.67}\text{Ni}_{0.33}\text{O}_2$ is investigated by X-ray absorption near edge structure (XANES) spectroscopy. Extended X-ray absorption fine structure (EXAFS) measurements are performed to study the local structural variation around Mn and Ni atoms and to investigate the reasons for capacity fading in P3-type material.

3.2 Results

3.2.1 Characteristics

In order to determine the synthesis temperature of pure P3-type $\text{Na}_{0.67}\text{Mn}_{0.67}\text{Ni}_{0.33}\text{O}_2$ in the present work and to investigate the evolution between P3 and P2 phases, the *in situ* high temperature XRD was performed from 650 to 950 °C in 2θ range 10° - 90°, illustrated in Fig. 3.1. In the temperature range 650 - 750 °C, all peaks in XRD patterns of $\text{Na}_{0.67}\text{Mn}_{0.67}\text{Ni}_{0.33}\text{O}_2$ are located at Bragg positions similar to those of P3-type $\text{Na}_{0.67}\text{TMO}_2$ ^[113]. The intensities of the (107) and (108) peaks, located at $2\theta \approx 52^\circ$ and $2\theta \approx 56^\circ$, respectively, decrease with the increasing temperature from 760 to 830 °C. The peak located at 48° is visible at 760 °C and the intensity of this peak increases with temperature. Simultaneously, the intensity of the reflection peaks at 35.5° , 38° and 62° becomes larger with increase of temperature. At 840 °C, the (101), (012), (105), (107) and (108) reflection peaks in the P3 phase disappear. In the temperature range 840 - 950 °C, we cannot observe any reflection of the P3 phase and all reflections of $\text{Na}_{0.67}\text{Mn}_{0.67}\text{Ni}_{0.33}\text{O}_2$ are located at Bragg positions similar to those of P2-type

$\text{Na}_{0.67}\text{TMO}_2^{[100]}$. During the increase of temperature, all reflection peaks slightly shift to smaller 2θ angle.

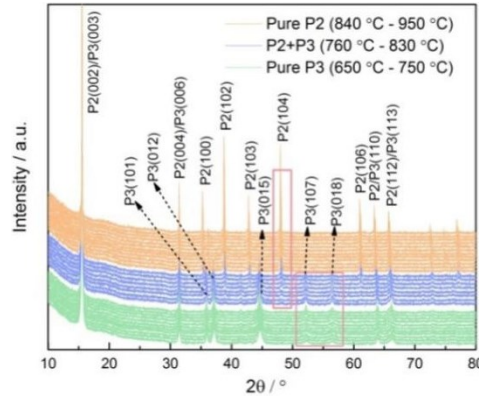


Fig. 3.1 *In situ* X-ray diffraction patterns of $\text{Na}_{0.67}\text{Mn}_{0.67}\text{Ni}_{0.33}\text{O}_2$ with temperature increase from 650 to 950 °C

In order to obtain pure P3-type $\text{Na}_{0.67}\text{Mn}_{0.67}\text{Ni}_{0.33}\text{O}_2$, the annealing temperature is supposed to be lower than 760 °C. In the present chapter, we prepared pure P3-type and P2-type $\text{Na}_{0.67}\text{Mn}_{0.67}\text{Ni}_{0.33}\text{O}_2$ materials at 750 and 950 °C, respectively. The XRD patterns of $\text{Na}_{0.67}\text{Mn}_{0.67}\text{Ni}_{0.33}\text{O}_2$ prepared at 950 and 750 °C along with the corresponding SEM micrographs of these two materials are illustrated in Fig. 3.2(a) – Fig. 3.2(d), respectively.

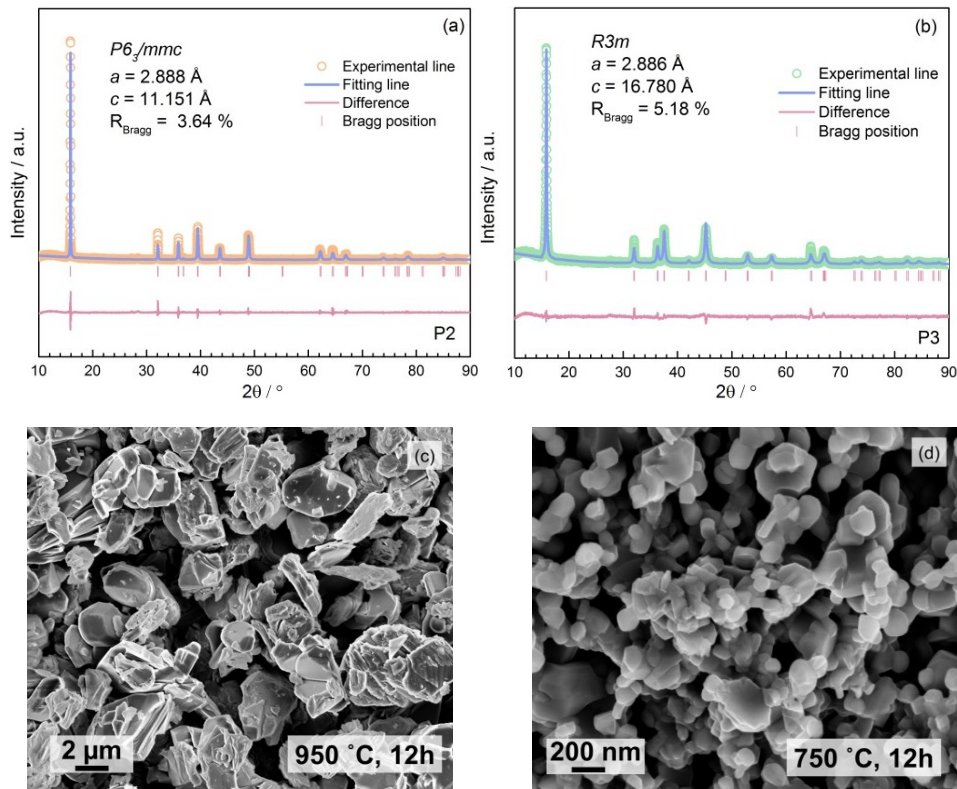


Fig. 3.2 X-ray diffraction patterns of P2-type (a) and P3-type (b) $\text{Na}_{0.67}\text{Mn}_{0.67}\text{Ni}_{0.33}\text{O}_2$ and scanning electron micrograph of P2-type (c) and P3-type (d) $\text{Na}_{0.67}\text{Mn}_{0.67}\text{Ni}_{0.33}\text{O}_2$

As shown in Fig. 3.2(a), all the reflection peaks in the XRD pattern are in agreement with the P2-type $\text{Na}_{0.67}\text{TMO}_2$ using the $P6_3/mmc$ space group^[111]. The lattice parameters of $\text{Na}_{0.67}\text{Mn}_{0.67}\text{Ni}_{0.33}\text{O}_2$ synthesized at 950 °C were determined by Rietveld refinement to $a = 2.888 \text{ \AA}$ and $c = 11.151 \text{ \AA}$. With regard to the material synthesized at 750 °C, all the reflection peaks in the XRD pattern shown in Fig. 3.2(b) are consistent with the P3-type $\text{Na}_{0.67}\text{TMO}_2$ indexed by the hexagonal crystal structure using the $R3m$ space group^[125]. The lattice parameters of P3-type $\text{Na}_{0.67}\text{Mn}_{0.67}\text{Ni}_{0.33}\text{O}_2$ are determined by Rietveld refinement to $a = 2.886 \text{ \AA}$ and $c = 16.780 \text{ \AA}$.

As shown in Fig. 3.2(c), the particle size of P2-type $\text{Na}_{0.67}\text{Mn}_{0.67}\text{Ni}_{0.33}\text{O}_2$ synthesized at 950 °C is of the order several micrometers. However, the particles of P3-type material prepared at 750 °C are much smaller than those of P2-type $\text{Na}_{0.67}\text{Mn}_{0.67}\text{Ni}_{0.33}\text{O}_2$, shown in Fig. 3.2(d). The particle size of P3-type $\text{Na}_{0.67}\text{Mn}_{0.67}\text{Ni}_{0.33}\text{O}_2$ is of the order of a few hundred nanometers.

3.2.2 Electrochemistry

After understanding the difference in crystal structure and morphology between P3-type and P2-type $\text{Na}_{0.67}\text{Mn}_{0.67}\text{Ni}_{0.33}\text{O}_2$ materials, their electrochemical performance is compared to explore the feasibility of lower temperature synthesized P3-type material as cathodes for sodium ion batteries.

Fig. 3.3 illustrates the initial charge and discharge curves of P2-type and P3-type $\text{Na}_{0.67}\text{Mn}_{0.67}\text{Ni}_{0.33}\text{O}_2$ materials in the voltage range 1.5 - 4.5 V at 0.1 C (1 C = 100 mA·g⁻¹) and the corresponding cycling performance of P3-type $\text{Na}_{0.67}\text{Mn}_{0.67}\text{Ni}_{0.33}\text{O}_2$ from the 1st cycle to the 120th cycle (at 0.1 C from the 1st to the 3rd cycle and at 1C from the 4th to the 120th cycle) in comparison with the performance of P2-type $\text{Na}_{0.67}\text{Mn}_{0.67}\text{Ni}_{0.33}\text{O}_2$. As shown in Fig. 3.3(a), the charge capacity of P3-type $\text{Na}_{0.67}\text{Mn}_{0.67}\text{Ni}_{0.33}\text{O}_2$ at 0.1 C is 154 mAh·g⁻¹ in the 1st cycle, which is slightly higher than that of P2-type material (150 mAh·g⁻¹). P3-type $\text{Na}_{0.67}\text{Mn}_{0.67}\text{Ni}_{0.33}\text{O}_2$ delivers discharge capacity of 233 mAh·g⁻¹ at 0.1 C in the voltage range 1.5 - 4.5 V in the 1st cycle, which is obviously higher than that of P2-type material (217 mAh·g⁻¹). The higher discharge capacity of P3-type material is a result of redox reaction under lower discharge voltage, observed as a plateau at discharge voltage of 1.9 V. The discharge capacities in P2-type or P3-type $\text{Na}_{0.67}\text{Mn}_{0.67}\text{Ni}_{0.33}\text{O}_2$ are higher than those charge capacities. As shown in Fig. 3.3(b), the discharge capacity points in P2-type and P3-type materials, respectively, overlap with the charge capacity points during the cycling from the 4th to the 120th cycle. In the

first three cycles, these two types of $\text{Na}_{0.67}\text{Mn}_{0.67}\text{Ni}_{0.33}\text{O}_2$ are cycled at 0.1 C and demonstrate larger discharge capacities than those cycled at 1 C in the following. P3-type $\text{Na}_{0.67}\text{Mn}_{0.67}\text{Ni}_{0.33}\text{O}_2$ has larger capacities than P2-type material during the first 40 cycles. However, the capacities of P3-type material decline continuously and gradually during cycling. The capacity retention of P3-type $\text{Na}_{0.67}\text{Mn}_{0.67}\text{Ni}_{0.33}\text{O}_2$ is 43% after 120 cycles of charge and 51% after 120 cycles of discharge in comparison with the capacities in the 4th cycle. P2-type material demonstrates different capacity fading trend in comparison with that of P3-type material. During the cycling, the capacities of P2-type $\text{Na}_{0.67}\text{Mn}_{0.67}\text{Ni}_{0.33}\text{O}_2$ drop more drastic than that of P3-type material in the first 20 cycles. The capacities of P2-type material slightly increase from the 21st to the 120th cycle. The capacity retention of P2-type material is 63% after 120 cycles of charge and 74% after 120 cycles of discharge in comparison with the capacities in the 4th cycle. The capacity retention of P3-type material is obviously lower than that of P2-type material.

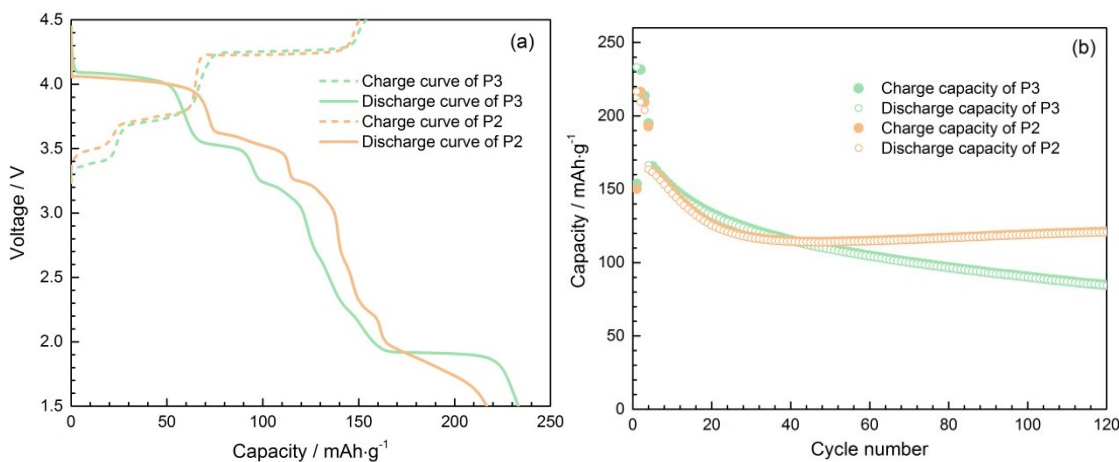


Fig. 3.3 Initial charge and discharge curves of P3-type $\text{Na}_{0.67}\text{Mn}_{0.67}\text{Ni}_{0.33}\text{O}_2$ in the voltage range 1.5 - 4.5 V at 1 C (1 C = $100 \text{ mA}\cdot\text{g}^{-1}$) and the corresponding cycling performance of P3-type $\text{Na}_{0.67}\text{Mn}_{0.67}\text{Ni}_{0.33}\text{O}_2$ at 0.1 C from 1st and 3rd cycles and at 1 C from the 4th to 120th cycles in comparison with those of P2-type $\text{Na}_{0.67}\text{Mn}_{0.67}\text{Ni}_{0.33}\text{O}_2$

The rate capability and the relevant discharge capacity retention of P3-type $\text{Na}_{0.67}\text{Mn}_{0.67}\text{Ni}_{0.33}\text{O}_2$ are compared with those of P2-type material at a constant charge rate (0.1 C, 1 C = $100 \text{ mA}\cdot\text{g}^{-1}$) and different charge rates from 0.1 C to 20 C each for 5 cycles in the voltage range 1.5 - 4.5 V, illustrated in Fig. 3.4. The initial discharge capacity of P3-type material remains larger than that of P2-type material at 0.1 C, as shown in Fig. 3.4(a). The discharge capacity of P3-type material decreases drastically from $234 \text{ mAh}\cdot\text{g}^{-1}$ in the 1st cycle to $176 \text{ mAh}\cdot\text{g}^{-1}$ in the 5th cycle, while the capacity of P2-type material remains above $190 \text{ mAh}\cdot\text{g}^{-1}$ after 5 cycles. From the 11th to the 25th cycles, the discharge capacities of P3-type $\text{Na}_{0.67}\text{Mn}_{0.67}\text{Ni}_{0.33}\text{O}_2$ remain slightly larger

than those of P2-type $\text{Na}_{0.67}\text{Mn}_{0.67}\text{Ni}_{0.33}\text{O}_2$. From the 26th to the 35th cycles, P2-type $\text{Na}_{0.67}\text{Mn}_{0.67}\text{Ni}_{0.33}\text{O}_2$ delivers higher discharge capacities than P3-type material. Although P3-type $\text{Na}_{0.67}\text{Mn}_{0.67}\text{Ni}_{0.33}\text{O}_2$ reveals larger discharge capacities than P2-type material at 20 C from the 36th to the 40th cycles, the capacities of P3-type material is only 20 $\text{mAh}\cdot\text{g}^{-1}$ in the 40th cycle. After discharge of these two types of $\text{Na}_{0.67}\text{Mn}_{0.67}\text{Ni}_{0.33}\text{O}_2$ at 20 C, they were discharged at 0.1 C again. In the 41st cycle, the discharge capacities of P3-type and P2-type $\text{Na}_{0.67}\text{Mn}_{0.67}\text{Ni}_{0.33}\text{O}_2$ return to 111 and 120 $\text{mAh}\cdot\text{g}^{-1}$, respectively. P3-type material demonstrates severe capacity fading at 0.1 C in the 41st - 45th cycles, while the discharge capacities of P2-type material remain relatively constant. The discharge capacities of P2-type and P3-type materials are 118 and 96 $\text{mAh}\cdot\text{g}^{-1}$ in the 45th cycle, respectively.

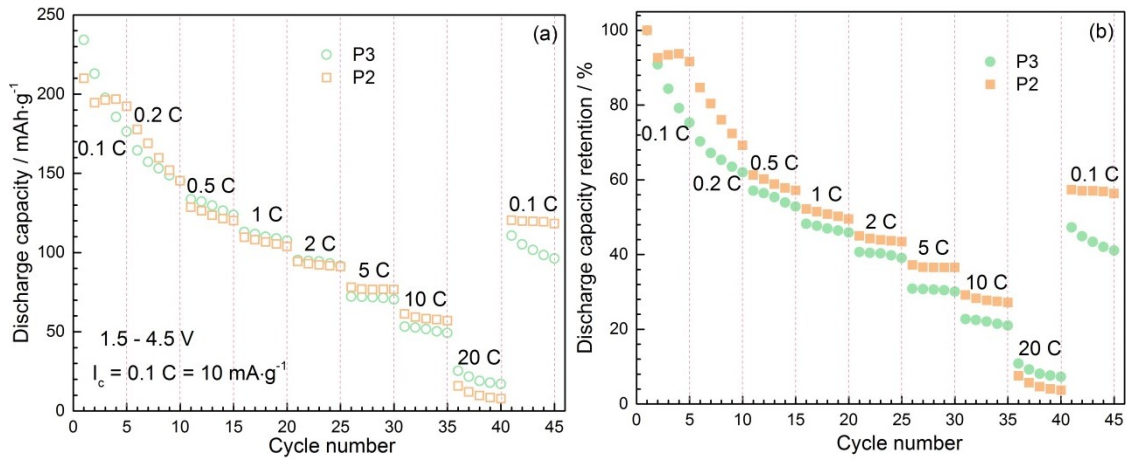


Fig. 3.4 Rate capabilities (a) and the corresponding discharge capacity retention (b) of P3-type $\text{Na}_{0.67}\text{Mn}_{0.67}\text{Ni}_{0.33}\text{O}_2$ at constant charge rate of 0.1 C and different discharge rates from 0.1 C to 20 C each for 5 cycles in the voltage range 1.5 - 4.5 V in comparison with P2-type $\text{Na}_{0.67}\text{Mn}_{0.67}\text{Ni}_{0.33}\text{O}_2$

As shown in Fig. 3.4(b), the discharge capacity retention of P2-type $\text{Na}_{0.67}\text{Mn}_{0.67}\text{Ni}_{0.33}\text{O}_2$ remains larger than that of P3-type material at different discharge rates, except discharge at 20 C. The discharge capacity retention of P3-type $\text{Na}_{0.67}\text{Mn}_{0.67}\text{Ni}_{0.33}\text{O}_2$ is 7% after 40 cycles at different discharge rates in comparison with the discharge capacity of this material in the 1st cycle. This extremely low capacity retention is larger than that of P2-type material after 40 cycles at different discharge rates, which is only 3%. In the 41st cycle, the discharge rate is decreased to 0.1 C and the discharge capacity retention increases to 47% in P3-type material and 57% in P2-type material. The discharge capacity retention of P2-type and P3-type materials is 56% and 41% after 45 cycles, respectively.

3.2.3 XANES

XANES spectra of P2-type and P3-type $\text{Na}_{0.67}\text{Mn}_{0.67}\text{Ni}_{0.33}\text{O}_2$ at Mn and Ni K-edge at different charge and discharge states are normalized using the ATHENA program and illustrated in Fig. 3.5 with related Mn oxides and Ni oxides reference compounds, respectively.

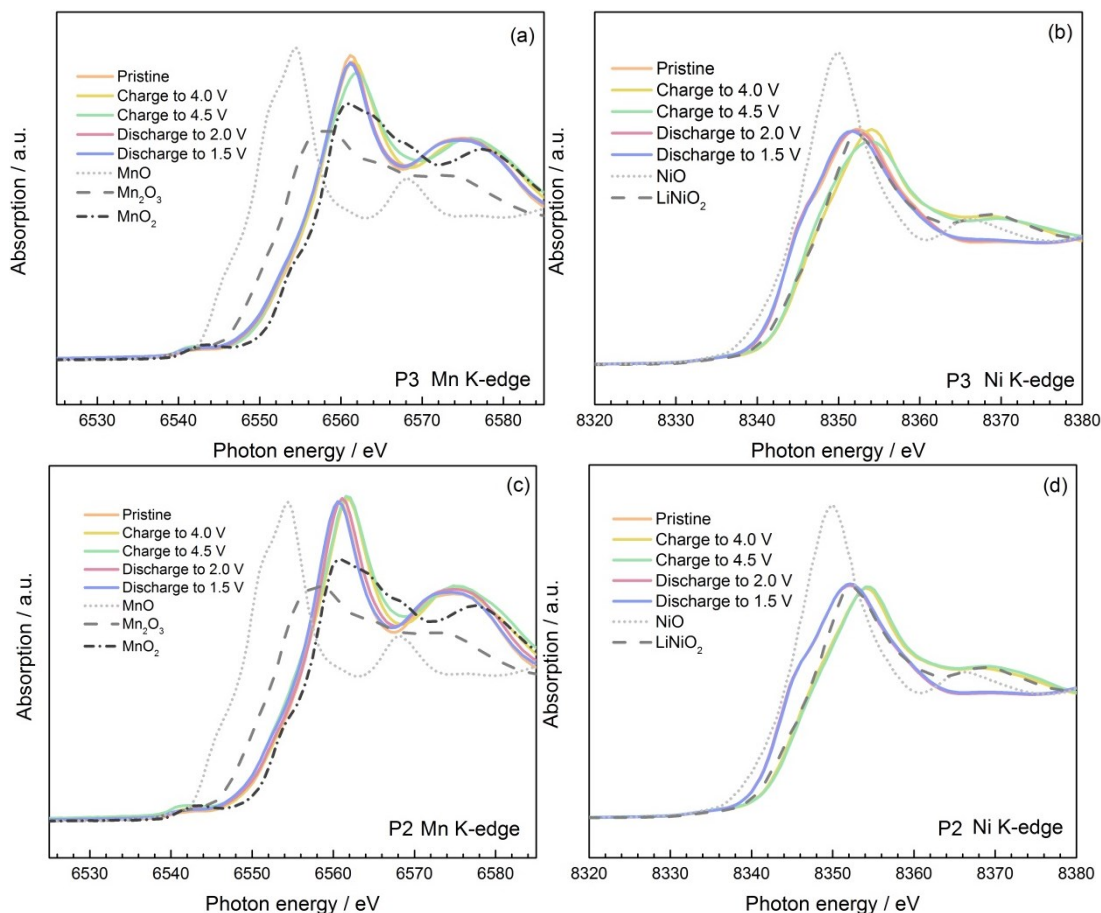


Fig. 3.5 Normalized X-ray absorption near edge structure spectra of P3-type $\text{Na}_{0.67}\text{Mn}_{0.67}\text{Ni}_{0.33}\text{O}_2$ at various states during the first charge and discharge at Mn (a) and Ni (b) K-edge and those of P2-type $\text{Na}_{0.67}\text{Mn}_{0.67}\text{Ni}_{0.33}\text{O}_2$ at Mn (c) and Ni (d) K-edge along with related Mn oxides and Ni oxides reference compounds

The pre-edge of the Mn and Ni spectra in Fig. 3.5 is related to the photoelectron transition from 1s to 3d orbital, which is obvious at the Mn K-edge of P2-type and P3-type $\text{Na}_{0.67}\text{Mn}_{0.67}\text{Ni}_{0.33}\text{O}_2$, but invisible at the Ni K-edge. The main edges (white line) corresponding to the photoelectron transition from 1s to unoccupied 4p orbital provide information about valence states of Mn and Ni in these two materials^[126]. The changes in energy position at Mn and Ni K-edge between different charge and discharge states are named as chemical shifts which demonstrate the changes of average valance states of Mn and Ni, respectively, in these two materials^[127]. The main peak at Mn K-edge in

pristine P3-type $\text{Na}_{0.67}\text{Mn}_{0.67}\text{Ni}_{0.33}\text{O}_2$ is located between those of Mn_2O_3 and MnO_2 , illustrated in Fig. 3.5(a). The main peak at Ni K-edge in pristine P3-type $\text{Na}_{0.67}\text{Mn}_{0.67}\text{Ni}_{0.33}\text{O}_2$ is located between those of NiO and LiNiO_2 , shown in Fig. 3.5(b). The main peaks of both Mn and Ni K-edge shift to higher energy position during charge and shift to lower energy position during discharge. At charge voltage of 4.0 V, the intensity of the main peak at Mn K-edge is slightly lower than that of the pristine state and that of the Ni K-edge remains about the same as that of the pristine state. The intensities of the main peaks at Mn and Ni K-edge become smaller after charge to 4.5 V in comparison with those of the pristine state. The curve of Mn K-edge at discharge voltage of 2.0 V overlaps with that of 1.5 V. The intensities of these two spectra are slightly smaller than that of Mn K-edge in pristine state. The intensity changes of spectra at Mn and Ni K-edge in P3-type material is a result of distortion and coordination changes, respectively, around Mn and Ni atoms^[93].

In P2-type $\text{Na}_{0.67}\text{Mn}_{0.67}\text{Ni}_{0.33}\text{O}_2$, the shape of the spectra at the Mn and Ni K-edge is similar to the corresponding spectra of P3-type material, illustrated in Fig. 3.5(c) and Fig. 3.5(d). The main peaks at Mn and Ni K-edge in P2-type material shift to higher energy positions during charge and return to lower energy positions during discharge, respectively. The changes in intensity of the main peaks at the Mn and Ni K-edge at charge voltage of 4.5 V are smaller in P2-type material in comparison with those of P3-type material at state of 4.5 V.

The energy positions of the main peaks of P2-type and P3-type $\text{Na}_{0.67}\text{Mn}_{0.67}\text{Ni}_{0.33}\text{O}_2$ at different charge and discharge states at Mn and Ni K-edge are illustrated in Fig. 3.6.

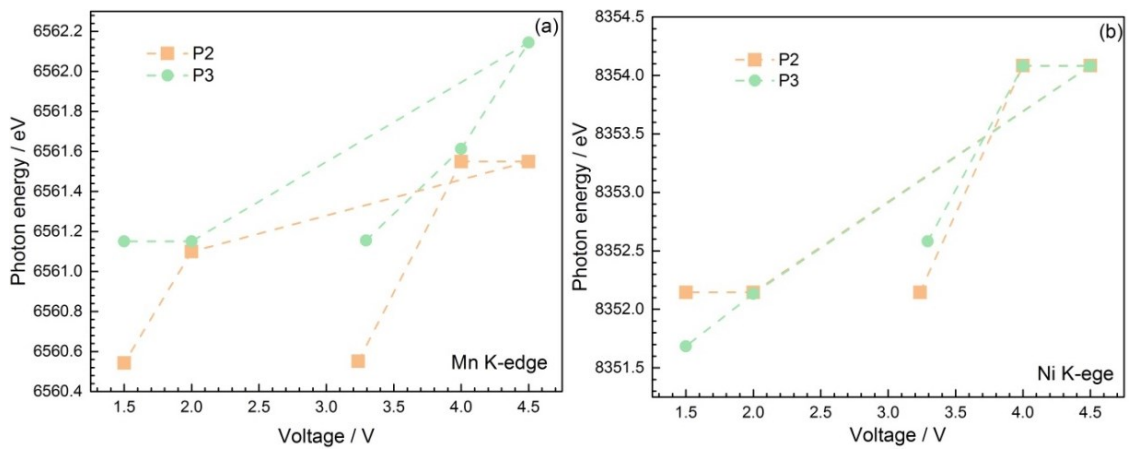


Fig. 3.6 Peak positions of Mn (a) and Ni (b) K-edge of P2-type and P3-type $\text{Na}_{0.67}\text{Mn}_{0.67}\text{Ni}_{0.33}\text{O}_2$ at different charge and discharge states in the 1st cycle

Here, we qualitatively compare the trend of energy shift during cycling of P2-type and P3-type materials. With increase of charge voltage to 4.0 V, the energy of the Mn and Ni K-edge in P2-type and P3-type materials increases indicating oxidation of Mn and Ni in these two materials. In the charge voltage range 4.0 - 4.5 V, the energy of P3-type material at Mn K-edge increase. However, the energy of P2-type material at Mn and Ni K-edge and P3-type material at Ni K-edge remains relatively constant. In the discharge voltage range 4.5 - 2.0 V, the energy of the main peaks of P2-type and P3-type materials at Mn and Ni K-edge decreases indicating reduction of Mn and Ni in P3-type and P2-type $\text{Na}_{0.67}\text{Mn}_{0.67}\text{Ni}_{0.33}\text{O}_2$. During discharge from 2.0 to 1.5 V, the energy of the main peak at Mn K-edge remains constant in P3-type material and decreases in P2-type material, while that at Ni K-edge remains constant in P2-type material and decreases in P3-type material.

3.2.4 EXAFS

Fig. 3.7 illustrates the k^3 -weighted EXAFS data of P3-type and P2-type $\text{Na}_{0.67}\text{Mn}_{0.67}\text{Ni}_{0.33}\text{O}_2$ after Fourier transformation (FT) at the Mn K-edge and Ni K-edge at different states of charge and discharge. The first maxima, shown in Fig. 3.7(a) and Fig. 3.8(c), are the result of photoelectron scattering between the absorbing Mn and the nearest coordinated atoms in P3-type and P2-type materials, respectively. The first maxima, illustrated in Fig. 3.7(b) and Fig. 3.7(d), are the result of photoelectron scattering between the absorbing Ni and the nearest coordinated atoms in P3-type and P2-type materials, respectively. The second maxima in Fig. 3.7(a) and Fig. 3.7(c) come from the photoelectron scattering between Mn and atoms in the second coordination shell and those in Fig. 3.7(b) and Fig. 3.7(d) come from the photoelectron scattering between Ni and atoms occupying the second coordination shell.

Although the amplitudes of the first maxima in Fig. 3.7(a) change with charge and discharge voltage, their shapes are similar to each other. The shape of the first maximum at Mn K-edge in P2-type material becomes different after charge to 4.5 V in comparison with other charge and discharge states, see Fig. 3.7(c). The first maxima in Fig. 3.7(b) and Fig. 3.7(d) obviously shift to the left during charge and shift to the right during discharge. During the cycling, the changes in distance between Ni and the nearest coordinated atoms are more drastic than those between Mn and the nearest coordinated atoms. The amplitudes of the first maxima at Ni K-edge remarkably decrease during charge and increase during discharge. During charge, the second

maxima in Fig. 3.7(a) and Fig. 3.7(c) slightly shift to the left indicating slight decrease in distance between Mn and atoms coordinating in the second nearest shell. The same trend of the second maxima in Fig. 3.7(b) and Fig. 3.7(d) is observed during charge indicating smaller distance between Ni and atoms in the second coordination shell. The amplitude ratios between the first and the second maxima in P3-type and P2-type materials are both smaller than 1 at different charge and discharge states, except that of P3-type material at Mn after charge to 4.5 V. The ratio between the first and the second maxima in P3-type material is larger than 1 at Mn K-edge at charge voltage of 4.5 V indicating the different changes of coordination around Mn and Ni in P3-type material after charge to 4.5 V. In the range 3 - 5 Å, the spectra in P2-type material at Mn and Ni K-edge after discharge to 1.5 V overlap with those of pristine state. With regard to P3-type material, the shape of the spectra in the range 3 - 5 Å at Mn and Ni K-edge after discharge to 4.5 V is different from those at Mn and Ni K-edge in the pristine state, respectively.

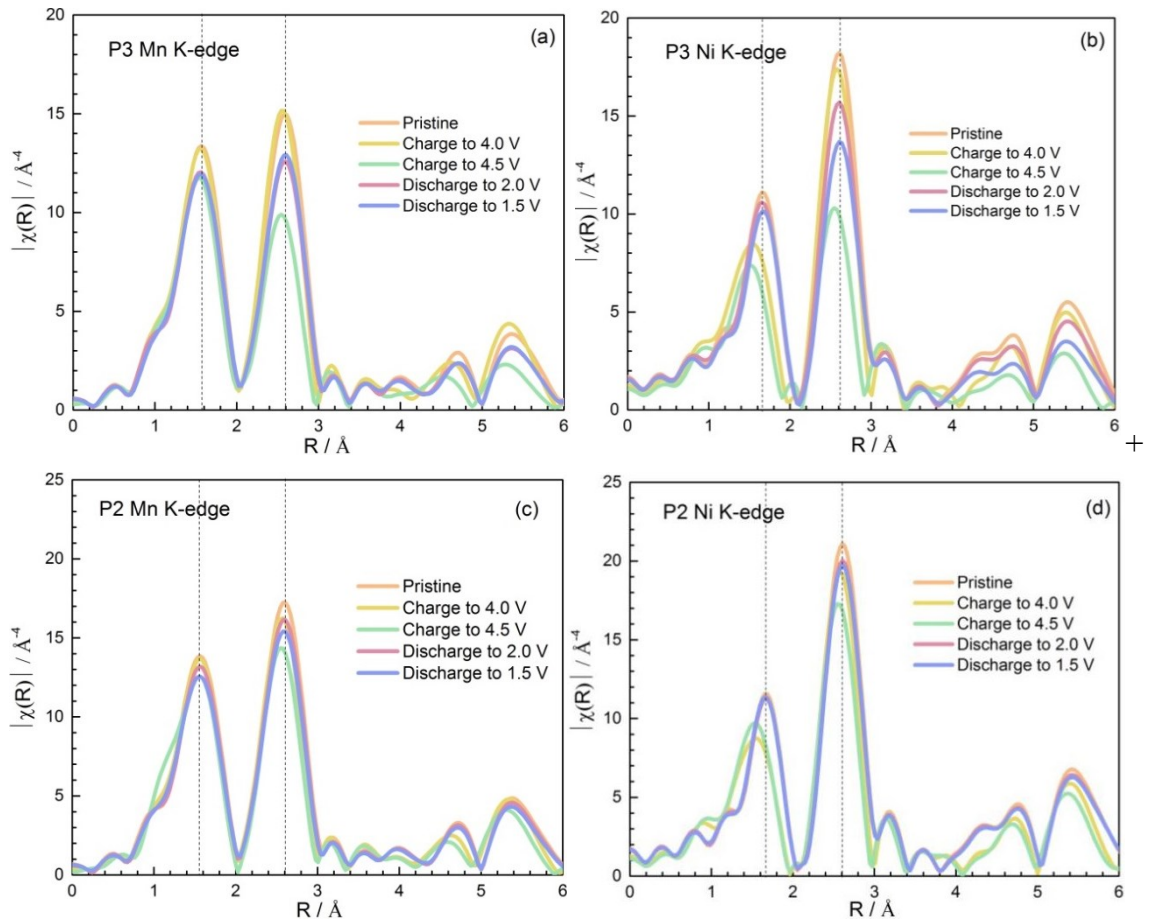


Fig. 3.7 The k^3 -weighted extended X-ray absorption fine structure spectra of P3-type $\text{Na}_{0.67}\text{Mn}_{0.67}\text{Ni}_{0.33}\text{O}_2$ after Fourier transformation at the Mn (a) and Ni (b) K-edge and those of P2-type $\text{Na}_{0.67}\text{Mn}_{0.67}\text{Ni}_{0.33}\text{O}_2$ at the Mn (c) and Ni (d) K-edge at different states of charge and discharge

3.2.5 Local structure in P3-type $\text{Na}_{0.67}\text{Mn}_{0.67}\text{Ni}_{0.33}\text{O}_2$

Fig. 3.8 illustrates the fitted k^3 -weighted EXAFS data of P3-type $\text{Na}_{0.67}\text{Mn}_{0.67}\text{Ni}_{0.33}\text{O}_2$ after FT at the Mn K-edge in the 1 - 5 Å range at different states of charge and discharge.

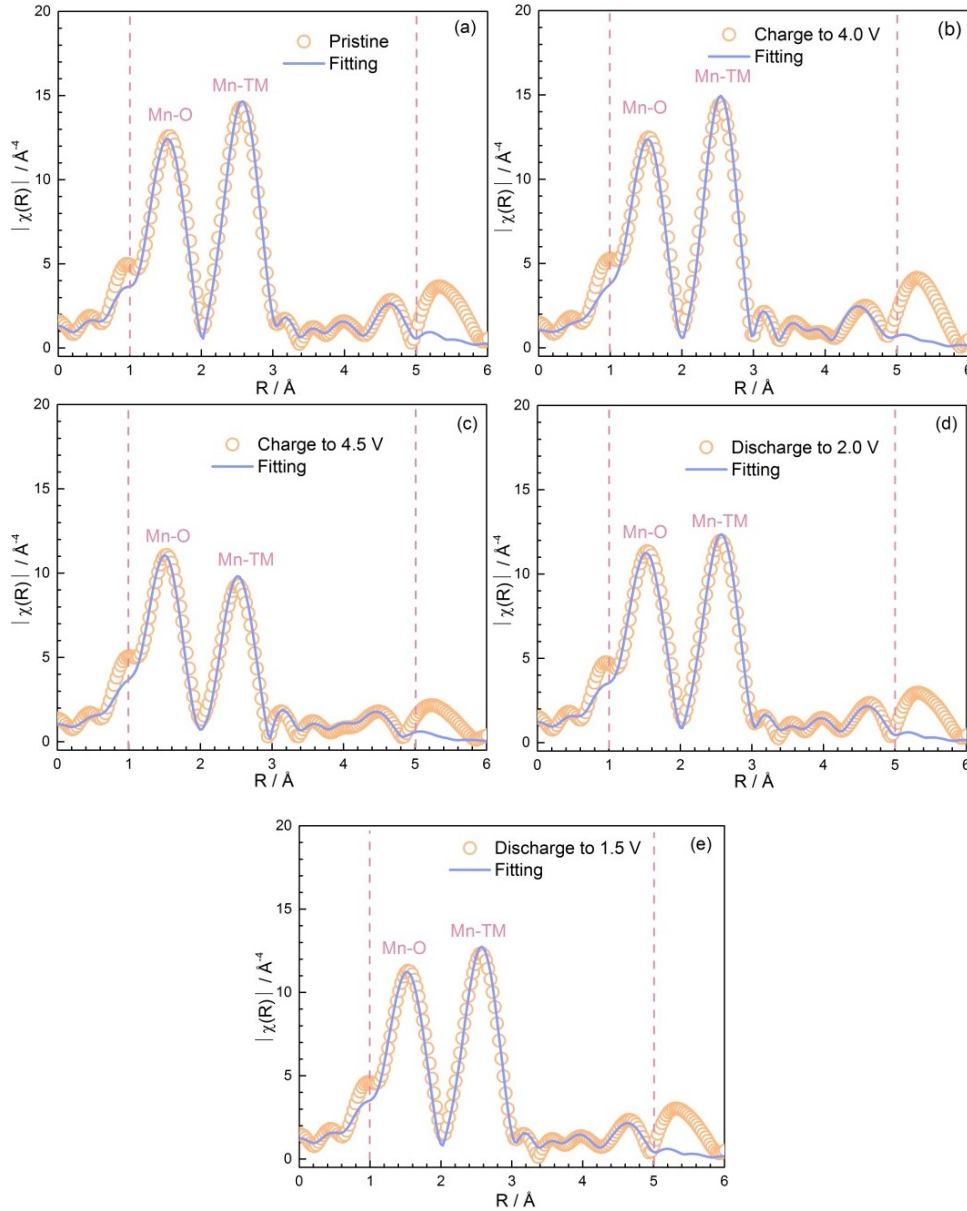


Fig. 3.8 Fourier transformation of the extended X-ray absorption fine structure spectra along with the fitting profiles (fitting range of 1 - 5 Å) of P3-type $\text{Na}_{0.67}\text{Mn}_{0.67}\text{Ni}_{0.33}\text{O}_2$ at the Mn K-edge in pristine material (a), after charged to 4.0 V (b), charged to 4.5 V (c), discharged to 2.0 V (d) and discharged to 1.5 V (e)

The amplitude reduction factor for Mn obtained by fitting the EXAFS data in pristine P3-type $\text{Na}_{0.67}\text{Mn}_{0.67}\text{Ni}_{0.33}\text{O}_2$ is $S_0^2 = 0.96 \pm 0.11$ with $R = 0.0061$, which is in the physically reasonable range of $0.7 < S_0^2 < 1.1$ ^[128]. The scattering model of Mn K-edge in the pristine state is used to evaluate the local structural variation around Mn at different

charge and discharge states. All calculated R values at different charge and discharge states at Mn K-edge are smaller than 0.02 indicating the fitting results are physically reliable^[112, 129]. The first maxima in Fig. 8 are related to the scattering of photoelectrons from the absorbing Mn atom to the nearest six occupied O atoms. The second maxima are a result of photoelectron scattering from the absorbing Mn atom to the nearest six occupied TM atoms.

Fig. 3.9 illustrates the fitted k^3 -weighted EXAFS data of P3-type $\text{Na}_{0.67}\text{Mn}_{0.67}\text{Ni}_{0.33}\text{O}_2$ after FT at the Ni K-edge in the 1 - 5 Å range at different states of charge and discharge.

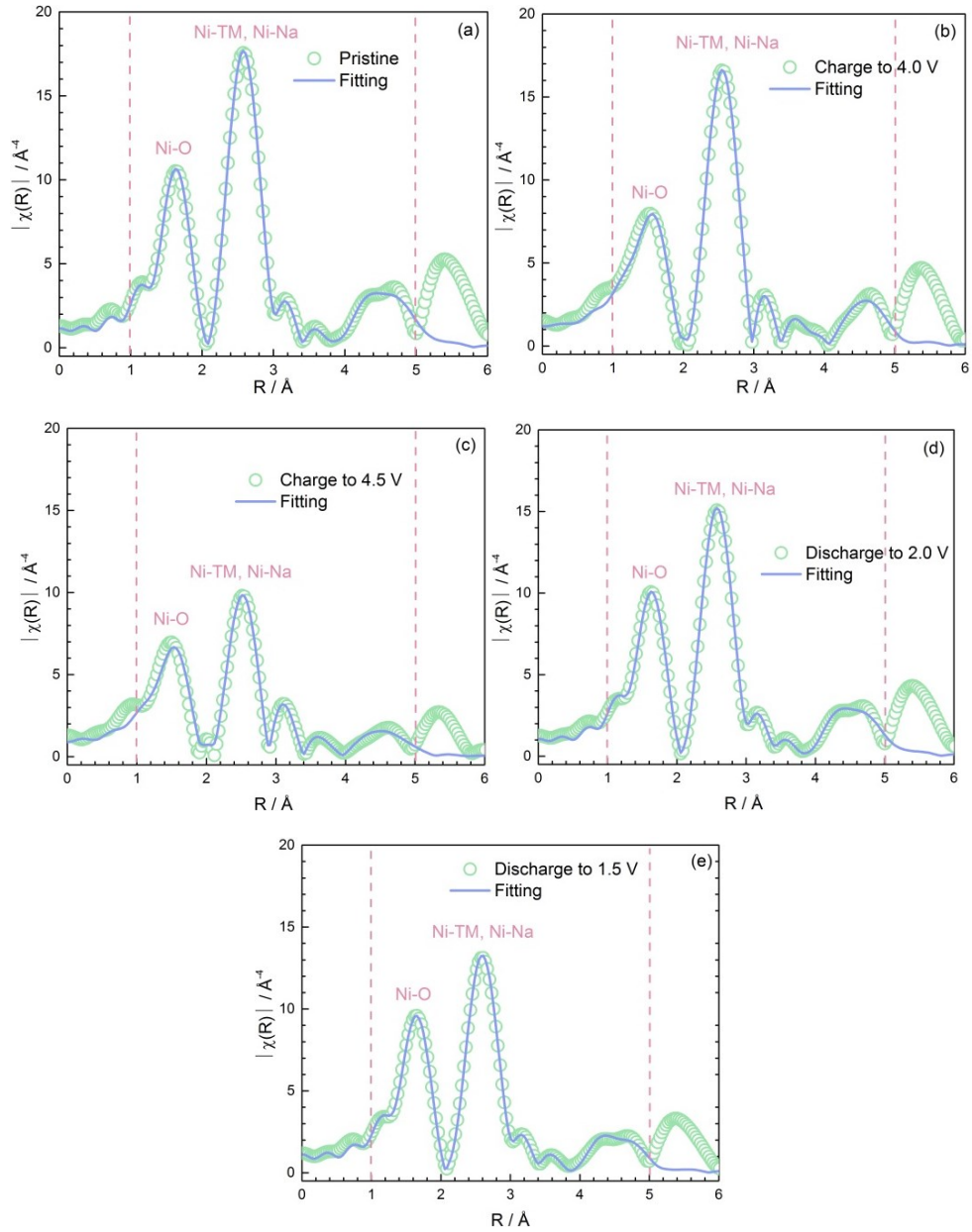


Fig. 3.9 Fourier transformation of the extended X-ray absorption fine structure spectra along with the fitting profiles (fitting range of 1 - 5 Å) of P3-type $\text{Na}_{0.67}\text{Mn}_{0.67}\text{Ni}_{0.33}\text{O}_2$ at the Ni K-edge in pristine material (a), after charged to 4.0 V (b), charged to 4.5 V (c), discharged to 2.0 V (d) and discharged to 1.5 V (e)

The amplitude reduction factor for Ni obtained by fitting the EXAFS data of the pristine P3-type $\text{Na}_{0.67}\text{Mn}_{0.67}\text{Ni}_{0.33}\text{O}_2$ is $S_0^2 = 0.99 \pm 0.13$ with $R = 0.0018$ which is also in the physically reasonable range. The scattering model in pristine P3-type material is used to evaluate the local structural changes around Ni during the cycling. The amplitude reduction factors are constant as 0.99 ± 0.13 at different charge and discharge states of P3-type material. The calculated R values at Ni K-edge at different charge and discharge states are both smaller than 0.02. Similar to the first shell around Mn atoms, the first maxima in Fig. 3.9 represent six O atoms occupying the first coordination shell around a Ni atom. The second maxima are related to the scattering of photoelectrons from the absorbing Ni to the nearest coordinated six *TM* atoms and four Na atoms.

Fig. 3.10 is a schematic illustration of the local structure around Mn and Ni in pristine P3-type $\text{Na}_{0.67}\text{Mn}_{0.67}\text{Ni}_{0.33}\text{O}_2$. The blue dot represents the absorbing *TM* atom. In the blue marked *TM* layer, there are six *TM* atoms around the central absorbing atom, which contribute to the amplitudes of the second maxima in Fig. 3.8 and Fig. 3.9. The yellow marked layer with three oxygen atoms is located above the *TM* layer. Another three oxygen atoms are located within a red marked layer below the *TM* layer. The brown rings stand for the sites of three Na atoms below the red marked oxygen layer and the brown box represents the site of Na atom above the yellow marked layer. These four Na sites are occupied when the central atom is Ni, but they remain unoccupied when the central atom is Mn.

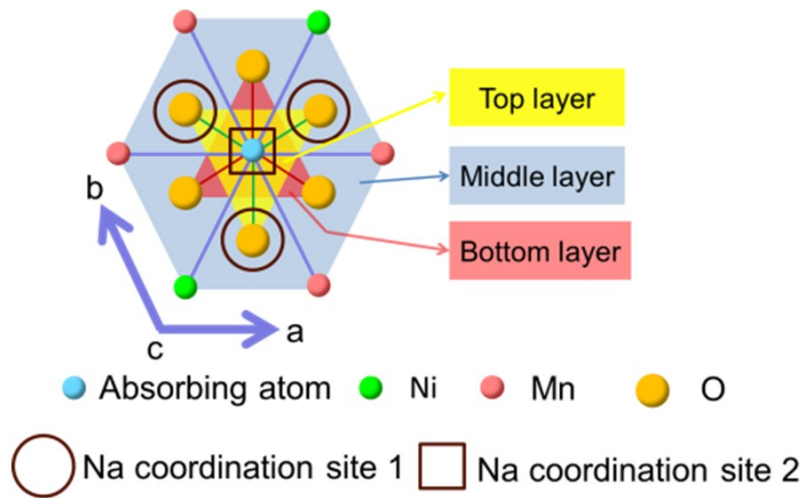


Fig. 3.10 Schematic depiction of the local structure of P3-type $\text{Na}_{0.67}\text{Mn}_{0.67}\text{Ni}_{0.33}\text{O}_2$ around Mn and Ni

In the following, the structural variation of TMO_6 units during cycling of P3-type $\text{Na}_{0.67}\text{Mn}_{0.67}\text{Ni}_{0.33}\text{O}_2$ is discussed by quantitative analysis of the EXAFS results. Fig.

3.11 schematically shows the local structure variation of P3-type $\text{Na}_{0.67}\text{Mn}_{0.67}\text{Ni}_{0.33}\text{O}_2$ at different states of charge and discharge according to the fitting results of EXAFS data at Mn and Ni K-edge. In pristine P3-type $\text{Na}_{0.67}\text{Mn}_{0.67}\text{Ni}_{0.33}\text{O}_2$, the calculated length of Mn-O and Ni-O bonds is $1.906 \pm 0.007 \text{ \AA}$ and $2.077 \pm 0.008 \text{ \AA}$, respectively. The distance between Ni and the nearest coordinated *TM* is $2.905 \pm 0.010 \text{ \AA}$ and that between Mn and the nearest occupied *TM* is $2.901 \pm 0.007 \text{ \AA}$. The average angle between Mn-O bonds is calculated in octahedral TMO_6 units as 99.11° and that between Ni-O bonds is calculated as 88.75° .

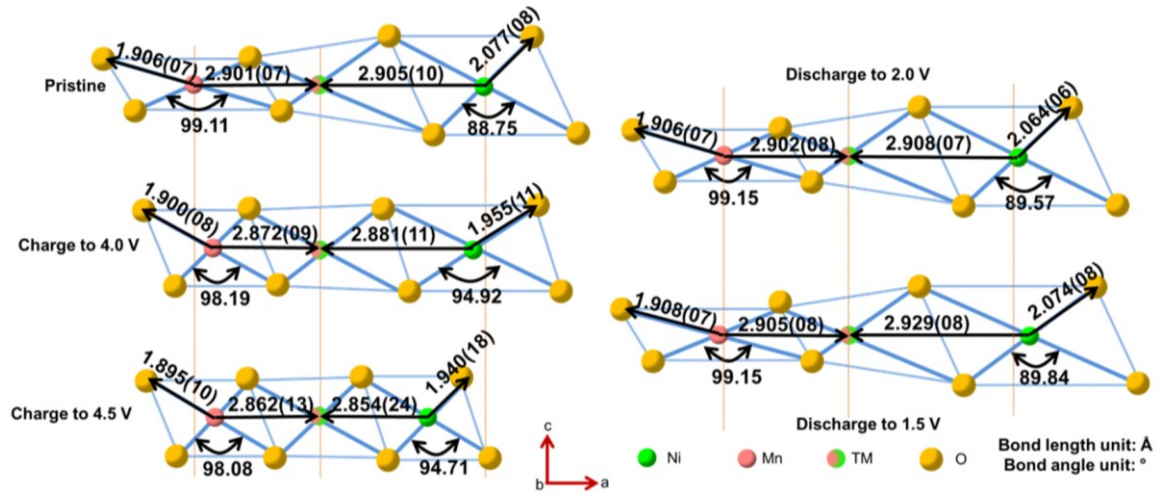


Fig. 3.11 Schematic depiction of the changes of Mn-O, Mn-*TM*, Ni-O and Ni-*TM* bonds in P3-type $\text{Na}_{0.67}\text{Mn}_{0.67}\text{Ni}_{0.33}\text{O}_2$ at various charge and discharge states obtained by fitting EXAFS data at Mn and Ni K-edge

After charge to 4.0 V, the calculated length of Mn-O and Ni-O bonds is $1.900 \pm 0.008 \text{ \AA}$ and $1.955 \pm 0.011 \text{ \AA}$, respectively. The distance between Ni and the nearest coordinated *TM* is $2.872 \pm 0.009 \text{ \AA}$ and that between Mn and the nearest occupied *TM* is $2.881 \pm 0.011 \text{ \AA}$. The average angle between Mn-O bonds is 98.19° and that between Ni-O bonds is 94.92° .

At state of 4.5 V, the uncertainty of calculated interatomic distance becomes larger. The calculated length of Mn-O and Ni-O bonds is $1.895 \pm 0.010 \text{ \AA}$ and $1.940 \pm 0.018 \text{ \AA}$, respectively. The distance between Ni and the nearest coordinated *TM* is $2.862 \pm 0.013 \text{ \AA}$ and that between Mn and the nearest occupied *TM* is $2.854 \pm 0.024 \text{ \AA}$. The average angle between Mn-O bonds is 98.08° and that between Ni-O bonds is 94.71° .

After discharge to 2.0 V, the average interatomic distance between atoms is similar to that of pristine. The length of Mn-O and Ni-O bonds is $1.906 \pm 0.007 \text{ \AA}$ and $2.064 \pm$

0.006 Å, respectively. The distance between Ni and the nearest coordinated *TM* is 2.902 ± 0.008 Å and that between Mn and the nearest occupied *TM* is 2.908 ± 0.007 Å. The average angle between Mn-O bonds is 99.15° and that between Ni-O bonds is 89.57° .

At state of 1.5 V, the average interatomic distance between Ni and *TM* continues increase, while that between Mn and *TM* remains relatively constant. The length of Mn-O and Ni-O bonds is 1.908 ± 0.007 Å and 2.074 ± 0.008 Å, respectively. The distance between Ni and the nearest coordinated *TM* is 2.905 ± 0.008 Å and that between Mn and the nearest occupied *TM* is 2.929 ± 0.008 Å. The average angle between Mn-O bonds is 98.15° and that between Ni-O bonds is 89.84° .

Fig. 3.12 illustrates the changes of the Debye-Waller factor σ for Mn-O, Ni-O, Mn-*TM* and Ni-*TM* bonds in P3-type $\text{Na}_{0.67}\text{Mn}_{0.67}\text{Ni}_{0.33}\text{O}_2$ at different charge and discharge states obtained by fitting EXAFS data at Mn and Ni K-edge, respectively. The σ^2 parameter of Mn-O bonds is smaller than that of Ni-O bonds in pristine state. However, the σ^2 parameter of Mn-*TM* bonds is slightly larger than that of Ni-*TM* bonds. The σ^2 parameters of Mn-O, Ni-O, Mn-*TM* and Ni-*TM* bonds increase during charge. During discharge, the σ^2 parameters of Mn-O and Mn-*TM* bonds become smaller. The σ^2 parameters of Ni-O and Ni-*TM* bonds decrease during discharge from 4.5 to 2.0 V and slightly increase during discharge from 2.0 to 1.5 V.

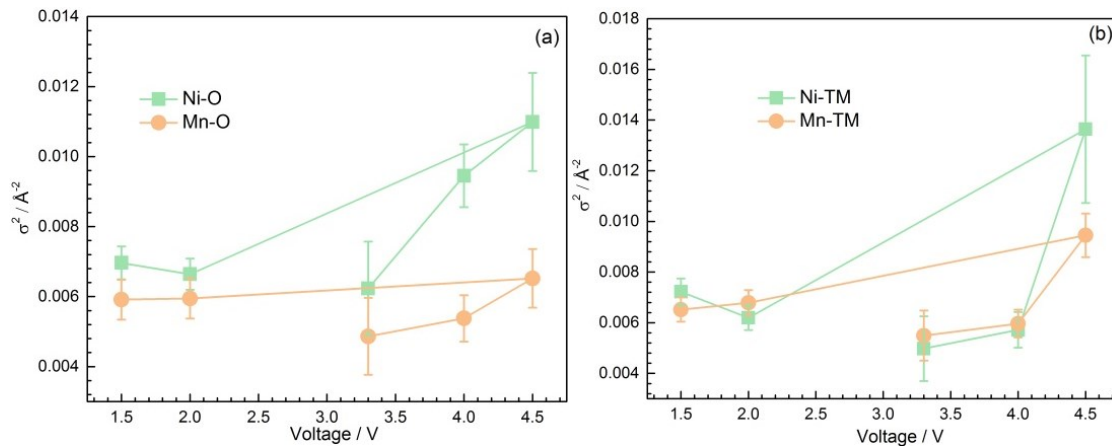


Fig. 3.12 Changes of the Debye-Waller factor for Mn-O, Ni-O, Mn-*TM* and Ni-*TM* bonds in P3-type $\text{Na}_{0.67}\text{Mn}_{0.67}\text{Ni}_{0.33}\text{O}_2$ at different charge and discharge states

3.3 Discussion

Because we prepared P2-type and P3-type $\text{Na}_{0.67}\text{Mn}_{0.67}\text{Ni}_{0.33}\text{O}_2$ at different temperatures (950 and 750°C) with the same calcination time, the crystal structure of $\text{Na}_{0.67}\text{Mn}_{0.67}\text{Ni}_{0.33}\text{O}_2$ is only determined by the temperature during calcination. The

higher annealing temperature (950 °C) is responsible for larger particle size of P2-type $\text{Na}_{0.67}\text{Mn}_{0.67}\text{Ni}_{0.33}\text{O}_2$ in comparison with the lower annealing temperature (750 °C) synthesized P3-type material, see Fig. 3.2. In P2-type and P3-type materials, Na atoms both occupy the prismatic units. In P2- $\text{Na}_{0.67}\text{Mn}_{0.67}\text{Ni}_{0.33}\text{O}_2$, Na atoms occupy two different types of sites, edge-sharing and face-sharing sites, respectively. In different P2-type $\text{Na}_{0.67}\text{TMO}_2$ materials, the ratio between Na atoms occupying edge-sharing and face-sharing sites is different^[122, 130]. There is only one type of occupancy of Na atoms in P3-type $\text{Na}_{0.67}\text{Mn}_{0.67}\text{Ni}_{0.33}\text{O}_2$.

Although Na atoms in P2-type and P3-type $\text{Na}_{0.67}\text{Mn}_{0.67}\text{Ni}_{0.33}\text{O}_2$ occupy different positions, the extraction of Na ions in these two structures is similar, which can be concluded from the similar initial charge curve at 0.1 C shown in Fig. 3.3(a). The initial charge capacities of P2-type and P3-type materials are both larger than those of initial discharge capacities, respectively. The number of inserted Na atoms after discharge to 1.5 V is larger than that of extracted Na ions after charge to 4.5 V. This leads to the crystal structures of P3-type and P2-type materials after discharge to 1.5 V are different from the pristine materials, respectively. The discharge capacity of P3-type $\text{Na}_{0.67}\text{Mn}_{0.67}\text{Ni}_{0.33}\text{O}_2$ becomes larger than that of P2-type material after discharge to 1.9 V. That means, the structure changes in P3-type material is more drastic than that of P2-type material in the discharge voltage 2.0 - 1.5 V. This is the reason for larger capacity fading during cycling of P3-type $\text{Na}_{0.67}\text{Mn}_{0.67}\text{Ni}_{0.33}\text{O}_2$ in comparison P2-type $\text{Na}_{0.67}\text{Mn}_{0.67}\text{Ni}_{0.33}\text{O}_2$. The poorer structural stability of P3-type material is reflected by the poorer rate capability in comparison with that of P2-type material. The specific discharge capacity of P3-type material is higher than those of P2-type material in the first 40 cycles, shown in Fig. 3.3(b). That means, P3-type material is a promising cathode which is prepared with lower energy consumption. However, the reason for poor cycling performance of P3-type material is urgently explored to enlarge the capacity retention and prolong cycling life.

We compared the XANES results at different charge and discharge states in P3-type and P2-type $\text{Na}_{0.67}\text{Mn}_{0.67}\text{Ni}_{0.33}\text{O}_2$ to figure out the reason for larger specific capacity in P3-type material. As shown in Fig. 3.5, the average valance state of Mn is between +3 and +4 in both P2-type and P3-type material and that of Ni in P2-type and P3-type materials is between +2 and +3. In Fig. 3.6, we observe lower energy of the peak at Mn and Ni K-edge in P2-type material. However, it is difficult to compare the valence state of Mn and Ni in P2-type and P3-type materials through comparing the energy position of the main

peaks at the Mn and Ni K-edge. The reason is the local structure around *TM* in P2-type and P3-type materials are different from each other. The different coordination around Mn and Ni also affects the width and the shape of white line in the spectra of P2-type and P3-type materials at Mn and Ni K-edge, respectively.

Here, the energy shifts of the main peak qualitatively demonstrate the redox reaction of Mn and Ni atoms in P2-type and P3-type materials. The energy shift at the Mn K-edge is smaller than that at the Ni K-edge, both in P2-type and P3-type materials after charge to 4.5 V, indicating the main oxidation activity of Ni in both P2-type and P3-type materials. After charge to 4.5 V, the main peaks of Ni K-edge in P3-type and P2-type materials are both located at higher energy in comparison with that of LiNiO_2 indicating some Ni atoms have been oxidized to Ni^{4+} . The slightly larger charge capacity of P3-type material after charge to 4.5 V is a result of oxidation of Mn, which is reflected by the increase in energy of Mn K-edge in P3-type material with charge voltage increase from 4.0 to 4.5V, see Fig. 3.6. During discharge, Ni atoms in P3-type and P2-type materials demonstrate the main reduction activity and contribute to the capacity of these materials. In the discharge voltage range 2.0 - 1.5 V, Ni atoms in P3-type material continue to be reduced and mainly contribute the discharge capacity of P3-type material. The large reduction activity of Ni is the reason for larger capacity of P3-type material, though the reduction of Mn in P2-type material is more obvious.

The k^3 -weighted EXAFS data of P3-type and P2-type $\text{Na}_{0.67}\text{Mn}_{0.67}\text{Ni}_{0.33}\text{O}_2$ after FT at the Mn K-edge and Ni K-edge is in agreement with XANES data which indicates Ni atoms demonstrate the main redox activity during charge of P2-type and P3-type materials while the redox activity of Mn is relatively low. The distance between Ni and the atoms in the first shell is obviously changing during charge and discharge, illustrated in Fig. 3.7(b) and Fig. 3.7(d), while that between Mn and the atoms in its first shell is relatively constant during charge and discharge. The amplitude changes of the first and the second maxima of P3-type material at Mn and Ni K-edge are more drastic than those of P2-type material indicating severe local structural changes during the cycling of P3-type material. The difference in amplitude and shape of spectra at Mn and Ni K-edge in comparison between the pristine state and the state of 1.5 V is smaller in P2-type material indicating better local structural recoverability in P2-type material which is responsible for better cycling performance.

In order to elucidate the reason for poor cycling performance of P3-type material during the cycling, the k^3 -weighted EXAFS data of P3-type $\text{Na}_{0.67}\text{Mn}_{0.67}\text{Ni}_{0.33}\text{O}_2$ after FT at the Mn K-edge and Ni K-edge is fitted using the Artemis program. The first maxima in Fig. 3.8 and Fig. 3.9 are related to the scattering of photoelectrons from the absorbing Mn or Ni atoms, respectively, by the nearest occupied O atoms. Because of the dominant redox activity of Ni atoms compared with Mn atoms in P3-type $\text{Na}_{0.67}\text{Mn}_{0.67}\text{Ni}_{0.33}\text{O}_2$, the variations in position of the first maxima in the FT of the k^3 weighted EXAFS spectra, see Fig. 3.9, are ascribed to the oxidation and reduction of Ni atoms during charge and discharge. The redox of Ni leads to changes in the electrostatic attraction between Ni and O atoms, which are observed as shrinkage and elongation of Ni-O bonds, respectively. The changes in amplitude and shape of maxima are also determined by the variation in coordination number and distortion of the crystal lattice around Mn and Ni atoms^[131]. The amplitudes of the second maxima in Fig. 3.8 and Fig. 3.9 are ascribed to the scattering of photoelectrons from the, respectively, absorbing Mn and Ni atoms by the nearest coordinated *TM* and Na atoms.

In P3-type $\text{Na}_{0.67}\text{Mn}_{0.67}\text{Ni}_{0.33}\text{O}_2$, Mn and Ni occupy the centers of octahedral TMO_6 units, similar to the occupancy of *TM* ions in other layered Na_xTMO_2 materials^[132-134]. In fact, including Ni-Na scattering paths in the 2 - 3 Å range in the fitting procedure, we found considerable improvement of the quality of the fits to the Ni K-edge EXAFS data of pristine P3-type $\text{Na}_{0.67}\text{Mn}_{0.67}\text{Ni}_{0.33}\text{O}_2$. The best fits were obtained when all four nearest Na sites around Ni are occupied. In contrast, the quality of the fits at the Mn K-edge was improved by excluding the scattering between Mn and Na in the fitting range of 2 - 3 Å, pointing to unoccupied nearest Na coordination sites around Mn.

In combination of ordered arrangement of Mn and Ni in P3-type material, the preferential occupation of Na around Ni is assumed to be the result of the electrostatic repulsion between *TM* and Na atoms. The valence state of *TM* in P3-type $\text{Na}_{0.67}\text{Mn}_{0.67}\text{Ni}_{0.33}\text{O}_2$ calculated by charge balance is +3.33. The average valence state of Mn atoms in pristine P3-type $\text{Na}_{0.67}\text{Mn}_{0.67}\text{Ni}_{0.33}\text{O}_2$ is higher than +3 and close to +4, while the average valence state of Ni is between +2 and +3. This indicates Mn atoms in pristine P3-type $\text{Na}_{0.67}\text{Mn}_{0.67}\text{Ni}_{0.33}\text{O}_2$ mainly exist as Mn^{4+} with small amount of Mn^{3+} . With regard to Ni atoms, Ni^{2+} and Ni^{3+} coexist in pristine P3-type $\text{Na}_{0.67}\text{Mn}_{0.67}\text{Ni}_{0.33}\text{O}_2$. The valence state of Mn^{4+} is larger than that of Ni^{2+} indicates the electrostatic repulsion between Mn^{4+} and Na^+ is larger than that between Ni^{2+} and Na^+ . The larger electrostatic repulsion between Mn^{4+} and Na^+ is supposed to be the reason for unoccupied Na sites

around Mn. The results from our EXAFS measurements therefore suggest that the presence of Na vacancies around Mn atoms as well as Na atoms around Ni is the energetically most favorable arrangement in pristine P3-type $\text{Na}_{0.67}\text{Mn}_{0.67}\text{Ni}_{0.33}\text{O}_2$.

In the following, the structural changes of TMO_6 units in view of interatomic distance and bond angle during cycling of P3-type $\text{Na}_{0.67}\text{Mn}_{0.67}\text{Ni}_{0.33}\text{O}_2$ are discussed by fitting EXAFS data at Mn and Ni K-edge. In the present work, we used the scattering model of pristine P3-type $\text{Na}_{0.67}\text{Mn}_{0.67}\text{Ni}_{0.33}\text{O}_2$ to assess the local structural changes around Mn and Ni at different charge and discharge states. This analysis method is reported in fitting the EXAFS data of layered LiTMO_2 without consideration of phase transitions during cycling^[135, 136]. During cycling of layered Na_xTMO_2 materials, no matter the pristine P2-, P3- and O3-type materials or the OP4 interphase, the structure of TMO_6 units is regarded as octahedral units^[14, 119]. Using the Artemis program, all calculated R values at different charge and discharge states at Mn and Ni K-edge are smaller than 0.02 indicating the scattering model is suitable for providing physically reliable results^[112, 129].

In pristine, the length of Mn-O bonds is smaller than that of Ni-O bonds which is in agreement with XANES at the Ni and Mn K-edge. The average valence state of Mn in P3-type material is larger than that of Ni indicating larger electrostatic attraction between Mn and O and shorter Mn-O bonds. After calculation, the average angle between Mn-O bonds in pristine P3-type material is 99.11° which is larger than that of Ni-O bonds (88.75°).

During charge to 4.0 V, the average length of Ni-O bonds decreases from 2.077 to 1.955 Å which is ascribed to the oxidation of Ni. However, the average change in length of Mn-O bonds is only 0.006 Å. This small value indicates low oxidation activity of Mn. The decline in the average distance between Mn and *TM* from 2.901 to 2.872 Å is responsible for shrinkage of MnO_6 units within the *a-b* plane. Similarly, the contraction of the average distance between Ni and *TM* from 2.905 to 2.881 Å represents the compression of NiO_6 units within the *a-b* plane. The shrinkage of MnO_6 and NiO_6 units is the reason for the shrinkage of TMO_2 layers at state of 4.0 V. During charge to 4.0 V, the average angle between Mn-O bonds decreases by 0.92° , while that of Ni-O bonds increases by 6.17° .

Continuing charge to 4.5 V, the average distance between Ni and *TM* as well as that between Mn and *TM* both become smaller, though the uncertainty of these value

increases. This indicates TMO_2 layers compress within the a - b plane. The larger uncertainty of interatomic distance indicates changes in coordination structure around Ni and Mn. In order to obtain more accurate local structure information around Ni, we tried to fit the EXAFS data of the sample charged to 4.5 V using the crystal structures of different MnO_2 and NiO_2 materials or neglecting the scattering path between TM and Na in the matched pristine scattering model. However, only using the same model and the same scattering paths as that of pristine model can obtain the physically reasonable results. The more accurate local structure information around Ni and Mn should be investigated in the future. At state of 4.5 V, the occupancy of Na sites is expected to be vacancies, the considered scattering between Ni and Na is the other reason for larger uncertainty of the calculated interatomic distance. In the charge voltage 4.0 - 4.5 V, the decline in average length of Mn-O bonds is small indicating low redox activity. The average length of Ni-O bonds decreases by 0.015 Å indicating the oxidation of Ni.

The dimensional changes in MnO_6 and NiO_6 units during discharge are reverse to those of charge. From 4.5 to 2.0 V, the slight change in length of Mn-O bonds indicates low reduction activity of Mn. The obvious elongation of Ni-O bonds indicates the main reduction activity of Ni. The increase in average angle between Mn-O bonds is 1.07°, while the decrease in average angle between Ni-O bonds is 5.14°. NiO_6 and MnO_6 units expand within the a - b plane, reflected by longer distance between Ni and TM as well as that between Mn and TM . This indicates TMO_2 layers stretch within the a - b plane. The dimension of TMO_2 layers within the a - b plane at state of 2.0 V becomes slightly larger than that of pristine state.

During discharge to 1.5 V, we observe a slight change in distance between Mn and TM , while the average distance between Ni and TM continues increasing to 2.929 Å. This leads to further expansion of TMO_2 layers which have negative effect on structural recoverability of P3-type material. The average length of Ni-O bonds increases by 0.01 Å indicating reduction of Ni. The length of Mn-O bonds remains relatively constant which is in agreement with XANES results. Mn atoms have no reduction activity in the discharge voltage range of 2.0 - 1.5 V.

Although we observe dimensional changes of MnO_6 and NiO_6 units by EXAFS measurements, the reason for these changes is difficult to be quantitatively compared. During cycling, the extraction and insertion of Na lead to changes in the electrostatic interaction between Na and TMO_6 units affecting the dimension of TMO_6 units. For P3-

type $\text{Na}_{0.67}\text{Mn}_{0.67}\text{Ni}_{0.33}\text{O}_2$, Na atoms prefer to occupy around Ni, while those sites around Mn are unoccupied by Na. This indicates the dimensional changes in NiO_6 units caused by the changes in electrostatic interaction between Na and TMO_6 units are severe than that of MnO_6 units. With extraction and insertion of Na, TM atoms are supposed to be oxidized or reduced to maintain the charge balance of layered Na_xTMO_2 materials and electrostatic equilibrium between atoms, accompanying by changes of bond length and bond angle in TMO_6 units. Due to the main redox activity of Ni and low redox activity of Mn in P3-type material, the changes in electrostatic attraction between TM and O lead to more drastic dimensional changes in NiO_6 units than that of MnO_6 units. In addition, the ionic radii and oxygen activity also affect the dimensional changes of TMO_6 units^[90, 137, 138].

Besides, the dimensional changes in TMO_6 units lead to changes in NaO_6 units. During cycling of layered Na_xTMO_2 , the slide of TMO_2 layers is supposed to be the reason for phase transitions, which are observed as structural changes in occupancy of Na sites^[14, 139]. For one NaO_6 unit, the structural changes of this unit are affected by changes in TMO_6 units above and below this unit. During the calculation, we hypothesize TMO_6 units in P3-type material are ideal octahedral units. In these TMO_6 units, they have equal length of TM -O bonds and equal angle between TM -O bonds. In this simplest situation, the shrinkage and expansion of TMO_6 units within the a - b plane and along the c axis change the dimension and structure of NaO_6 units during cycling of P3-type material. In the actual situation, the length of TM -O bonds in one TMO_6 unit is different from each other. There is a difference in the angle between TM -O bonds. Thus, the dimensional changes of TMO_6 units lead to more drastic changes in NaO_6 units which affect the structural stability of P3-type material. That means, hindering the dimensional changes in TMO_6 units is useful for decreasing the dimensional changes in NaO_6 units. For P3-type $\text{Na}_{0.67}\text{Mn}_{0.67}\text{Ni}_{0.33}\text{O}_2$, two strategies are feasible to improve the cycling performance of this material. The first one is to change the ordered arrangement of Mn and Ni into disordered distribution, which hinders the preferential occupancy of Na around Ni. This decreases the influence of changes in electrostatic interaction between Na and NiO_6 units on dimensional changes in NiO_6 units. The other one is to decrease the redox activity of Ni resulting in smaller shrinkage and elongation of Ni-O bonds. However, more Mn atoms are expected to be oxidized and reduced to compensate the charge and contribute the capacity during cycling.

The distortion of Mn-O bonds is smaller than those of Ni-O at different charge and discharge indicating the better structural stability of MnO_6 than that of NiO_6 , see Fig. 3.12(a). The distortion of Ni-O, Mn-O, Ni-*TM* and Mn-*TM* bonds both increases after discharge in comparison with those in pristine state which is a result of larger insertion of Na in P3-type $\text{Na}_{0.67}\text{Mn}_{0.67}\text{Ni}_{0.33}\text{O}_2$ after discharge in comparison with charge.

3.4 Conclusions

P3-type $\text{Na}_{0.67}\text{Mn}_{0.67}\text{Ni}_{0.33}\text{O}_2$ delivers higher specific capacity with at lower annealing temperature (750 °C) than P2-type material in the voltage range 1.5 - 4.5 V. During the cycling, the redox of Ni atoms mainly compensates the charge with extraction and insertion of Na in P2-type and P3-type materials. Based on the local structure investigation of P3-type material by EXAFS, the shrinkage and expansion of MnO_6 and NiO_6 units lead to the dimensional variation of TMO_2 layers and affect the structural recoverability of P3 phase after discharge. Hence, hindering the shrinkage of TMO_2 layers within the *a-b* plane during charge and expansion of TMO_2 layers during discharge is supposed to be an effective way to improve the cycling performance of layered Na_xTMO_2 . Due to the ordered arrangement of *TM* in P3-type $\text{Na}_{0.67}\text{Mn}_{0.67}\text{Ni}_{0.33}\text{O}_2$, Na atoms prefer to occupy around Ni while Na sites around Mn remain as vacancies. This leads to different electrostatic interaction between Na and TMO_6 units affecting the dimensional changes of TMO_6 units. Hence, one feasible strategy to improve the cycling performance of layered Na_xTMO_2 materials is to change the ordered arrangement of *TM* into disordered distribution. The other possible method to improve the cycling performance of P3-type $\text{Na}_{0.67}\text{Mn}_{0.67}\text{Ni}_{0.33}\text{O}_2$ is to decrease the redox activity of Ni and increase the redox activity of Mn.

4 Core-shell design in P3-type $\text{Na}_{0.67}\text{Mn}_{0.67}\text{Ni}_{0.33}\text{O}_2$

4.1 Motivation

Although P3-type $\text{Na}_{0.67}\text{Mn}_{0.67}\text{Ni}_{0.33}\text{O}_2$ has high specific capacity and is prepared at a lower synthesis temperature, the severe capacity fading is urgently to be improved. No matter the surface modification or the substitution both indicate extra consumption of raw materials during the preparation of P3-type $\text{Na}_{0.67}\text{Mn}_{0.67}\text{Ni}_{0.33}\text{O}_2$. In chapter 3, we confirm the ordered arrangement of Mn and Ni ions in P3-type $\text{Na}_{0.67}\text{Mn}_{0.67}\text{Ni}_{0.33}\text{O}_2$ is responsible for the preferential occupancy of Na around Ni which affects the dimensional changes of TMO_6 units. In combination of Wang's previous work on P2-type $\text{Na}_{0.6}\text{Cr}_{0.6}\text{Ti}_{0.4}\text{O}_2$, selecting *TM* ions with similar ionic radii is effective to obtain the disordered arrangement of *TM* ions in P2-type Na_xTMO_2 and improve their Na storage and cycling performance^[108]. A special method, which is useful to obtain P3-type $\text{Na}_{0.67}\text{Mn}_{0.67}\text{Ni}_{0.33}\text{O}_2$ with disordered arrangement of *TM*, is urgently to be explored. One promising method is to synthesize core-shell designed materials, which consist of a core with high redox activity material contributing the capacity and a shell with low redox activity material remaining the stable structure. The core-shell design has been confirmed as a powerful way for inhibition of capacity fading during the cycling of LiTMO_2 materials^[104-107]. However, the core-shell designed Na_xTMO_2 is never reported previously. The core-shell design was performed in P3-type $\text{Na}_{0.67}\text{Mn}_{0.67}\text{Ni}_{0.33}\text{O}_2$ which changes the ordered arrangement of Mn and Ni into a special disordered distribution without any substitution or the ionic radii management. In addition, the lower synthesis

temperature of P3-type $\text{Na}_{0.67}\text{Mn}_{0.67}\text{Ni}_{0.33}\text{O}_2$ further lowers the energy consumption during preparation.

In the present chapter, the difference between the normal and the gradient core-shell designed P3-type $\text{Na}_{0.67}\text{Mn}_{0.67}\text{Ni}_{0.33}\text{O}_2$ is compared by scanning electron microscopy (SEM). Focused ion beam (FIB) and energy dispersive X-ray (EDX) spectroscopy are performed to analyze the concentration of Mn ion from the surface to the core in the normal and the core-shell designed P3-type materials. The phase transition of P3-type $\text{Na}_{0.67}\text{Mn}_{0.67}\text{Ni}_{0.33}\text{O}_2$ after core-shell design is qualitatively investigated by *operando* X-ray diffraction (XRD) and elucidates the reason for better capacity properties of the gradient core-shell designed P3-type $\text{Na}_{0.67}\text{Mn}_{0.67}\text{Ni}_{0.33}\text{O}_2$ in comparison with the normal P3-type $\text{Na}_{0.67}\text{Mn}_{0.67}\text{Ni}_{0.33}\text{O}_2$.

4.2 Results

4.2.1 Characteristics

Fig. 4.1 illustrates XRD patterns of the core-shell designed P3-type $\text{Na}_{0.67}\text{Mn}_{0.67}\text{Ni}_{0.33}\text{O}_2$ in comparison with that of the normal P3-type material.

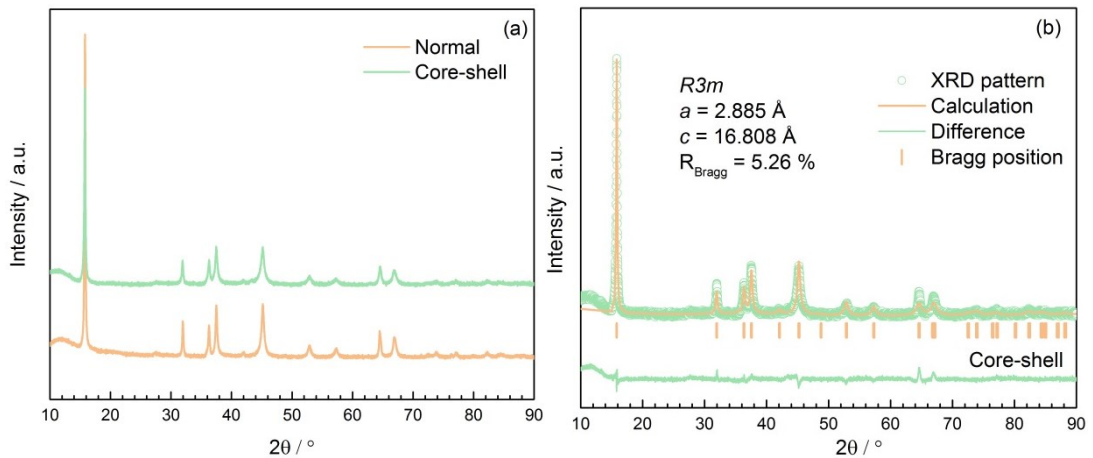


Fig. 4.1 X-ray diffraction patterns of the normal and the core-shell designed P3-type $\text{Na}_{0.67}\text{Mn}_{0.67}\text{Ni}_{0.33}\text{O}_2$ (a) and Rietveld refinement results of the core-shell designed P3-type $\text{Na}_{0.67}\text{Mn}_{0.67}\text{Ni}_{0.33}\text{O}_2$ (b)

As shown in Fig. 4.1(a), each reflection peak in the core-shell designed P3-type material is located at 2θ angle similar to that of the normal P3-type material, which indicates similar crystal structure between the normal and the core-shell designed materials. Fig. 4.1(b) illustrates that all the reflections in XRD pattern of the core-shell designed P3-type material are indexed in the hexagonal system using $R3m$ space group which is in agreement with P3-type $\text{Na}_{2/3}\text{TMO}_2$ material^[125].

Fig. 4.2 shows the difference in morphology and cross section between the normal and the core-shell designed P3-type $\text{Na}_{0.67}\text{Mn}_{0.67}\text{Ni}_{0.33}\text{O}_2$ particles.

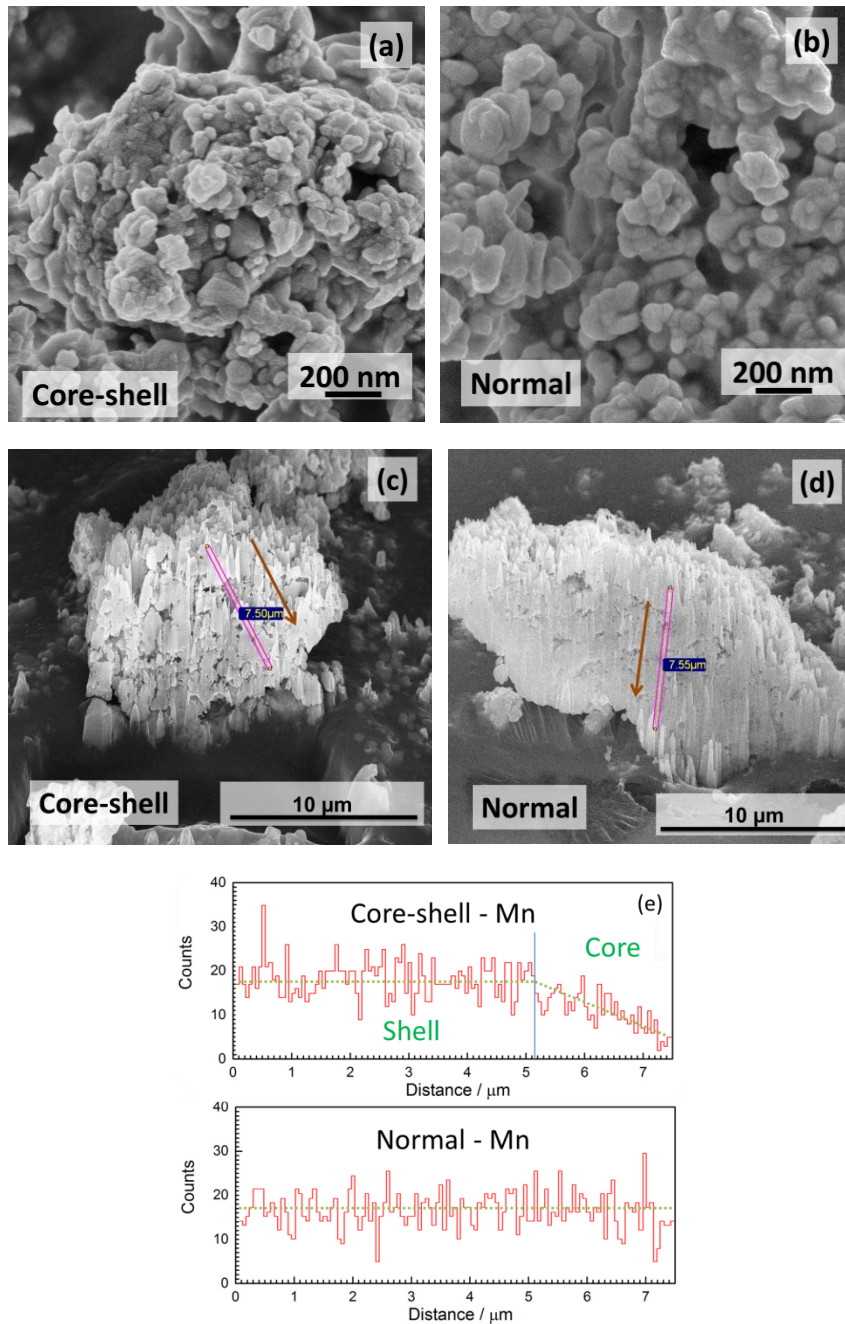


Fig. 4.2 Scanning electron microscopy images of the gradient core-shell (a) and the normal (b) P3-type $\text{Na}_{0.67}\text{Mn}_{0.67}\text{Ni}_{0.33}\text{O}_2$ as well as the cross section images of the gradient core-shell (c) and the normal (d) P3-type material with the concentration changes of Mn from the shell to the core of them obtained by energy dispersive X-ray (e)

Unlike the homogenous particles in the normal P3-type $\text{Na}_{0.67}\text{Mn}_{0.67}\text{Ni}_{0.33}\text{O}_2$, the particles on the surface of the core-shell designed P3-type $\text{Na}_{0.67}\text{Mn}_{0.67}\text{Ni}_{0.33}\text{O}_2$ are smaller and these small particles cover some large particles. The focused ion beam (FIB) was used to cut the particles of the normal and the core-shell designed P3-type

$\text{Na}_{0.67}\text{Mn}_{0.67}\text{Ni}_{0.33}\text{O}_2$ and the SEM images demonstrate the half part of the cross section in Fig. 4.2(c) and Fig. 4.2(d), respectively. We observe many pores in the core-shell designed P3-type $\text{Na}_{0.67}\text{Mn}_{0.67}\text{Ni}_{0.33}\text{O}_2$, while the inner part of the normal P3-type $\text{Na}_{0.67}\text{Mn}_{0.67}\text{Ni}_{0.33}\text{O}_2$ demonstrates less pores.

In order to further confirm the existence of core-shell layers, the concentration of Mn from the surface to the core is compared by line scan EDX between the normal and the core-shell designed P3-type $\text{Na}_{0.67}\text{Mn}_{0.67}\text{Ni}_{0.33}\text{O}_2$ recorded from the surface to the core, as illustrated in Fig. 4.2(e). The Mn composition in the normal P3-type $\text{Na}_{0.67}\text{Mn}_{0.67}\text{Ni}_{0.33}\text{O}_2$ fluctuates around a certain value from the surface to the center. In the shell of the special designed P3-type material, the average concentration of Mn remains relatively constant. In the core of the special designed P3-type material, the average concentration of Mn decreases.

Fig. 4.3 illustrates the normalized XANES spectra of P3-type $\text{Na}_{0.67}\text{Mn}_{0.67}\text{Ni}_{0.33}\text{O}_2$ in the core-shell state and in the normal state at Mn and Ni K-edge in comparison with Mn oxides and Ni oxides reference compounds, respectively.

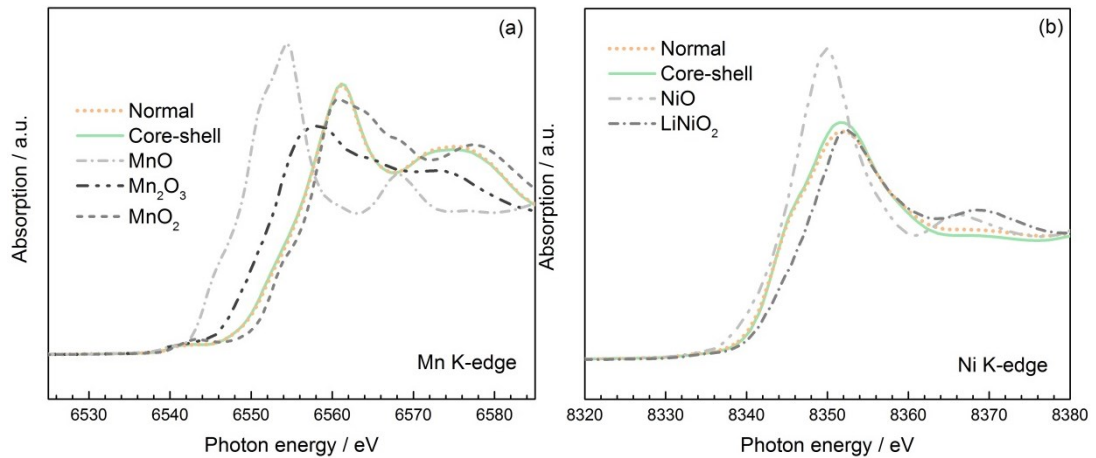


Fig. 4.3 Normalized X-ray absorption near edge structure spectra of the core-shell designed P3-type $\text{Na}_{0.67}\text{Mn}_{0.67}\text{Ni}_{0.33}\text{O}_2$ and of the normal P3-type $\text{Na}_{0.67}\text{Mn}_{0.67}\text{Ni}_{0.33}\text{O}_2$ at Mn (a) and Ni (b) K-edge with relevant oxide references

The pre-edge, representing the electron transition from 1s to 3d orbital, is unobvious at both Mn and Ni K-edge. The main peaks in Fig. 4.3(a) and Fig. 4.4(b) correspond to the electron transition from the 1s to the unoccupied 4p orbital at Mn and Ni K-edge, respectively. The Mn K-edge of the core-shell designed P3-type material is coincident with that of the normal P3-type material. The peak position of Ni K-edge in the core-shell designed material is located at the same energy position as that of the normal P3-type material, while the intensity of Ni K-edge in the core-shell designed P3-type

material is higher. This indicates the average valence state of Ni in the gradient core-shell designed material is the same as that of the normal P3-type material.

4.2.2 Electrochemistry

Fig. 4.4 displays the initial charge and discharge curves of the core-shell designed P3-type $\text{Na}_{0.67}\text{Mn}_{0.67}\text{Ni}_{0.33}\text{O}_2$ in the voltage ranges 1.5 - 4.5 V and 2.0 - 4.1 V at 0.1 C ($1\text{ C} = 100\text{ mA}\cdot\text{g}^{-1}$) and the corresponding cycling performance at 1 C in the voltage ranges 1.5 - 4.5 V from the 4th to the 200th cycle and 2.0 - 4.1 V from the 4th to the 250th cycle in comparison with the normal P3-type $\text{Na}_{0.67}\text{Mn}_{0.67}\text{Ni}_{0.33}\text{O}_2$.

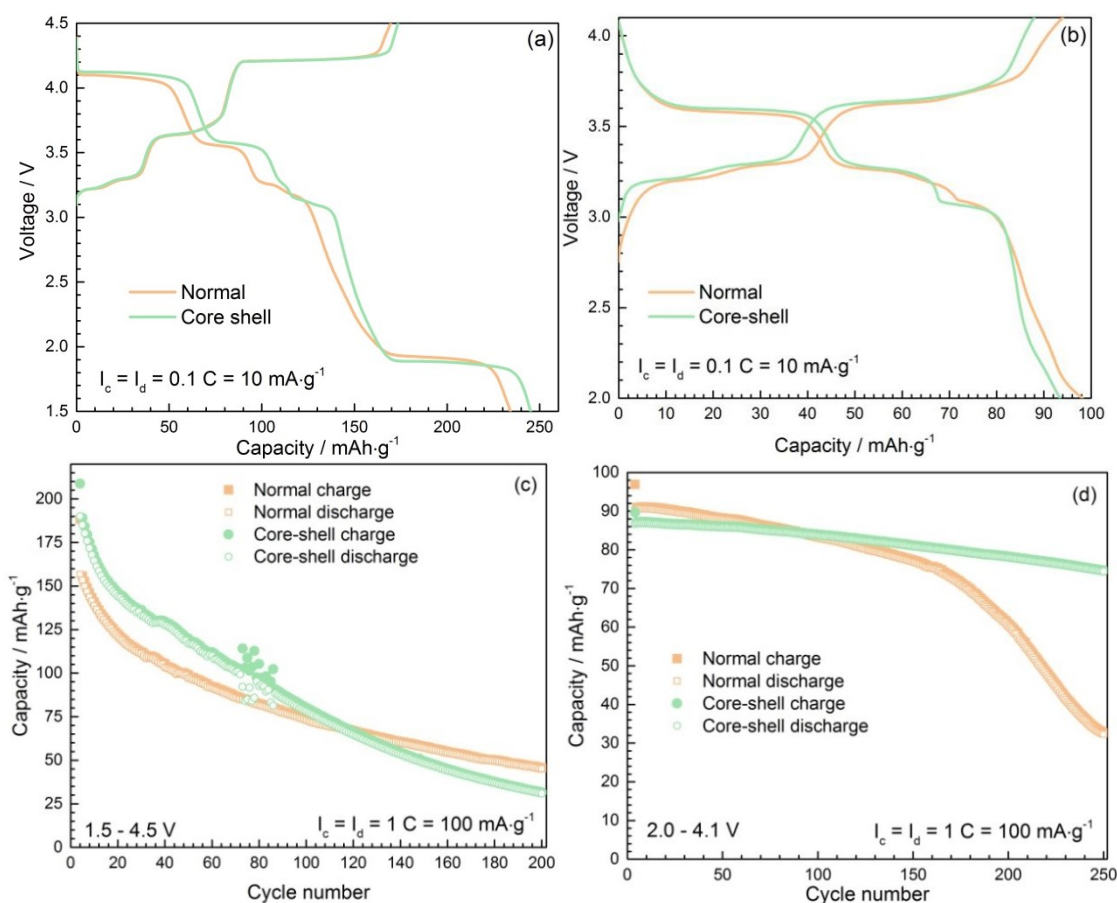


Fig. 4.4 First charge and discharge curves of the core-shell designed P3-type $\text{Na}_{0.67}\text{Mn}_{0.67}\text{Ni}_{0.33}\text{O}_2$ in the voltage ranges 1.5 - 4.5 V (a) and 2.0 - 4.1 V (b) at 0.1 C ($1\text{ C} = 100\text{ mA}\cdot\text{g}^{-1}$) in comparison with the normal P3-type $\text{Na}_{0.67}\text{Mn}_{0.67}\text{Ni}_{0.33}\text{O}_2$ and the corresponding cycling performance at 1C in the voltage ranges 1.5 - 4.5 V from the 4th to the 200th cycle (c) and 2.0 - 4.1 V from 4th to the 250th cycle (d)

As shown in Fig. 4.4(a) and Fig. 4.4(b), the core-shell designed P3-type $\text{Na}_{0.67}\text{Mn}_{0.67}\text{Ni}_{0.33}\text{O}_2$ delivers initial capacities of 173 $\text{mAh}\cdot\text{g}^{-1}$ during charge and 245 $\text{mAh}\cdot\text{g}^{-1}$ during discharge in the voltage range 1.5 - 4.5 V. They are larger than the corresponding values of the normal P3-type material. However, the capacities of the

core-shell designed P3-type $\text{Na}_{0.67}\text{Mn}_{0.67}\text{Ni}_{0.33}\text{O}_2$ are 88 and 93 $\text{mAh}\cdot\text{g}^{-1}$ during charge and discharge, respectively, in the voltage range 2.0 - 4.1 V. The capacities of the core-shell designed P3-type material are smaller than those of the normal P3-type material in the voltage range 2.0 - 4.1 V.

Although the core-shell designed P3-type $\text{Na}_{0.67}\text{Mn}_{0.67}\text{Ni}_{0.33}\text{O}_2$ demonstrates larger initial capacities in the voltage range 1.5 - 4.5 V, the capacity decay in the gradient core-shell designed P3-type $\text{Na}_{0.67}\text{Mn}_{0.67}\text{Ni}_{0.33}\text{O}_2$ is more drastic than that of the normal P3-type material, illustrated in Fig. 4.4(c). After 120 cycles, the core-shell designed material demonstrates smaller capacities than the normal P3-type material. The discharge capacity retention of the core-shell designed material after 200 cycles in the voltage range 1.5 - 4.5 V is only 16% in comparison with the discharge capacity in the 4th cycle.

In contrast, the cycling performance of the core-shell designed P3-type $\text{Na}_{0.67}\text{Mn}_{0.67}\text{Ni}_{0.33}\text{O}_2$ in the voltage range 2.0 - 4.1 V is obviously better than that of the normal P3-type material, though the core-shell designed $\text{Na}_{0.67}\text{Mn}_{0.67}\text{Ni}_{0.33}\text{O}_2$ demonstrates slightly lower capacities in comparison with the normal P3-type material, shown in Fig. 4.4(d). After 150 cycles of slight capacity decay, the capacity of the normal P3-type material decreases strongly. However, the capacity fading of the core-shell designed P3-type material is unobvious in Fig. 4.4(d). The discharge capacity of the core-shell designed P3-type material is 74 $\text{mAh}\cdot\text{g}^{-1}$ after 250 cycles in the voltage range 2.0 - 4.1 V which is much higher than that of the normal P3-type material. The discharge capacity retention of the core-shell designed P3-type $\text{Na}_{0.67}\text{Mn}_{0.67}\text{Ni}_{0.33}\text{O}_2$ is 86% after 250 cycles in comparison with the capacity of the 4th cycle.

Fig. 4.5 illustrates the rate capabilities and the relevant capacity retention of the normal and the core-shell designed P3-type $\text{Na}_{0.67}\text{Mn}_{0.67}\text{Ni}_{0.33}\text{O}_2$ in the voltage ranges 1.5 - 4.5 V and 2.0 - 4.1 V at constant charge rate of 0.1 C (1 C = 100 $\text{mA}\cdot\text{g}^{-1}$) and at various discharge rates from 0.1 C to 20 C each for 5 cycles, respectively. In the voltage range 1.5 - 4.5 V, the core-shell designed P3-type $\text{Na}_{0.67}\text{Mn}_{0.67}\text{Ni}_{0.33}\text{O}_2$ delivers higher discharge capacities at different discharge rates as shown in Fig. 4.5(a). However, the capacity decay in the core shell designed P3-type $\text{Na}_{0.67}\text{Mn}_{0.67}\text{Ni}_{0.33}\text{O}_2$ is also severe at different discharge rates in comparison with the normal P3-type material in the voltage range 1.5 - 4.5 V, especially during the first 5 cycles at 0.1 C. The discharge capacity of the normal P3-type $\text{Na}_{0.67}\text{Mn}_{0.67}\text{Ni}_{0.33}\text{O}_2$ decreases from 234 $\text{mAh}\cdot\text{g}^{-1}$ in the 1st cycle to

17 mAh·g⁻¹ in the 40th cycle in the voltage range 1.5 - 4.5 V, while the discharge capacity of the core-shell designed P3-type Na_{0.67}Mn_{0.67}Ni_{0.33}O₂ is 239 and 30 mAh·g⁻¹ in the 1st and the 40th cycles, respectively. When the discharge current decrease to 10 mA·g⁻¹ (0.1 C), the discharge capacity of the core-shell designed P3-type Na_{0.67}Mn_{0.67}Ni_{0.33}O₂ returns back to 142 mAh·g⁻¹ in the 41st cycle and remains as 134 mAh·g⁻¹ in the 45th cycle, which is at least 30 mAh·g⁻¹ higher than that of the normal P3-type Na_{0.67}Mn_{0.67}Ni_{0.33}O₂.

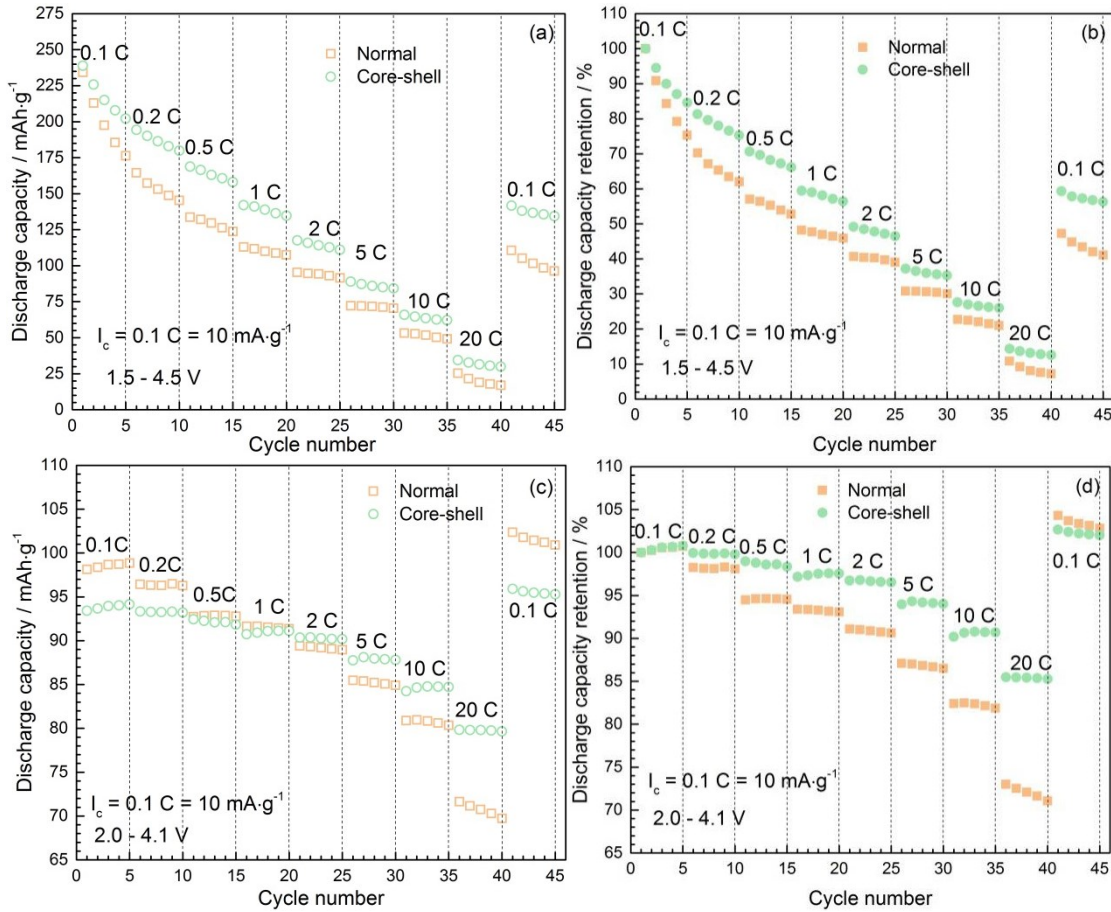


Fig. 4.5 Rate capabilities of the core-shell designed P3-type Na_{0.67}Mn_{0.67}Ni_{0.33}O₂ at different discharge rates in the voltage range 1.5 - 4.5 V (a) and 2.0 - 4.1 V (c) and corresponding discharge capacity retention in the voltage range 1.5 - 4.5 V (b) and 2.0 - 4.1 V (d) in comparison with the normal P3-type Na_{0.67}Mn_{0.67}Ni_{0.33}O₂

As shown in Fig. 4.5(b), the capacity retention of the core-shell designed P3-type Na_{0.67}Mn_{0.67}Ni_{0.33}O₂ is larger than that of the normal P3-type Na_{0.67}Mn_{0.67}Ni_{0.33}O₂. The capacity of the normal P3-type material remains less than 50% after 16 cycles, while that of the core-shell designed P3-type material remains larger than 50% after 20 cycles. The capacity retention of the core-shell designed P3-type Na_{0.67}Mn_{0.67}Ni_{0.33}O₂ is around 14% at 20 C from the 35th to 40th cycles which is slightly larger than that of the normal

P3-type material. From the 41st to 45th cycles, the capacity retention becomes larger than 55%.

In the voltage range 2.0 - 4.1 V, see Fig. 4.5(c), the initial discharge capacity of the core-shell designed P3-type material is only 94 mAh·g⁻¹ which is obviously smaller than that of the normal P3-type material (98 mAh·g⁻¹). In the first 5 cycles, the discharge capacities of these two materials both increase. During discharge at 0.2 C from the 6th to the 10th cycle, the capacity gap between the normal and the core-shell designed materials becomes smaller. From the 21st to the 25th cycles, the discharge capacities of the core-shell designed P3-type material are larger than that of the normal P3-type material. At discharge rate of 20 C, the discharge capacity of the core-shell designed P3-type material is larger than 80 mAh·g⁻¹, while that of the normal P3-type material is smaller than 73 mAh·g⁻¹. However, the capacity of the normal P3-type material becomes larger than that of the core-shell designed P3-type material from the 41st cycle at discharge rate of 0.1 C.

As shown in Fig. 4.5(d), the capacity retention in the core-shell designed P3-type material is obviously larger than that of the normal P3-type material during first 40 cycles at different discharge rates. With increase of discharge rates, the gap of capacity retention between the normal and the core-shell designed P3-type material becomes larger. At discharge rate of 20 C, the capacity retention of the core-shell designed P3-type material remains larger than 85%, while that of the normal P3-type material remains smaller than 75%. From the 41st to the 45th cycles at 0.1 C, the capacity retention of the normal and the core-shell designed P3-type material are larger than 100%.

According to the outstanding capability of the core-shell designed P3-type material at 20 C in the voltage range 2.0 - 4.1 V, illustrated in Fig. 4.5(c), the cycling performance of these two materials during the slow and fast cycling was compared in this voltage range 2.0 - 4.1 V. Fig. 4.6 illustrates the cycling performance of the core-shell designed P3-type Na_{0.67}Mn_{0.67}Ni_{0.33}O₂ in the voltage range 2.0 - 4.1 V at different charge rates of 0.1 C and 20 C and discharge rate of 20 C in comparison with the normal P3-type Na_{0.67}Mn_{0.67}Ni_{0.33}O₂. The cycling performance of the core-shell designed P3-type Na_{0.67}Mn_{0.67}Ni_{0.33}O₂ is obviously improved at different charge rates in the voltage range 2.0 - 4.1 V in comparison with the normal P3-type Na_{0.67}Mn_{0.67}Ni_{0.33}O₂. During slow charge and fast discharge, the capacities of the gradient core-shell designed P3-type

$\text{Na}_{0.67}\text{Mn}_{0.67}\text{Ni}_{0.33}\text{O}_2$ is smaller than that of the normal P3-type material at the beginning, see Fig. 4.6(a). After 80 cycles of slow charge and fast discharge, the capacities of the normal P3-type material are smaller than the corresponding values of the core-shell designed P3-type material and the capacities of the normal P3-type material starts to decrease drastically. The capacity of the core-shell designed P3-type material are $60 \text{ mAh}\cdot\text{g}^{-1}$ after 400 cycles of slow charge and fast discharge, which remains as 77% of the discharge capacity in the 4th cycle. However, the capacity of the normal P3-type material decreases to $23 \text{ mAh}\cdot\text{g}^{-1}$ after 400 cycles.

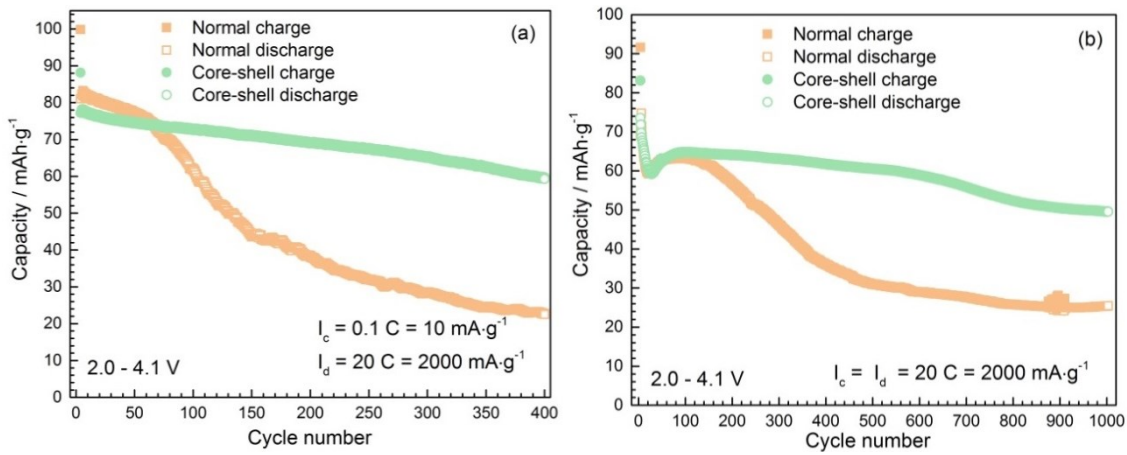


Fig. 4.6 Cycling performance of the core-shell designed P3-type $\text{Na}_{0.67}\text{Mn}_{0.67}\text{Ni}_{0.33}\text{O}_2$ in the voltage range 2.0 - 4.1 V at charge rate of 0.1 C ($1 \text{ C} = 100 \text{ mA}\cdot\text{g}^{-1}$) and discharge rate of 20 C (a) and at charge rate of 20 C and discharge rate of 20 C (b) in comparison with the normal P3-type $\text{Na}_{0.67}\text{Mn}_{0.67}\text{Ni}_{0.33}\text{O}_2$

As shown in Fig. 4.6(b), the core-shell designed P3-type material demonstrates drastic capacity decay from 83 to $59 \text{ mAh}\cdot\text{g}^{-1}$ during fast charge and fast discharge for 20 cycles. The capacity of the normal P3-type material has similar fading trend as the core-shell designed P3-type material. Then, the capacity of these two materials slightly increases in the following tens of cycles. From the 120th cycle, the capacity of the core-shell designed P3-type material decreases gradually and slowly. The capacity of the core-shell designed P3-type material is $50 \text{ mAh}\cdot\text{g}^{-1}$ after 1000 cycles of fast charge and discharge which is 2 times of the normal P3-type material. The discharge capacity of the core-shell designed P3-type $\text{Na}_{0.67}\text{Mn}_{0.67}\text{Ni}_{0.33}\text{O}_2$ after 1000 cycles of fast charge and discharge remains as 67% of the discharge capacity in the 4th cycle.

4.2.3 Operando XRD

Fig. 4.7 shows the structure evolution of the normal and the core-shell designed P3-type $\text{Na}_{0.67}\text{Mn}_{0.67}\text{Ni}_{0.33}\text{O}_2$ recorded by *operando* synchrotron XRD measurements during the

first cycle at 0.1 C in the voltage range 1.5 - 4.5 V with the charge and discharge curves, respectively. The changes in intensity and width of reflections correspond to the phase transitions during charge and discharge which are in analogy to the intercalation of sodium in other layered Na_xTMO_2 ^[121, 122, 140].

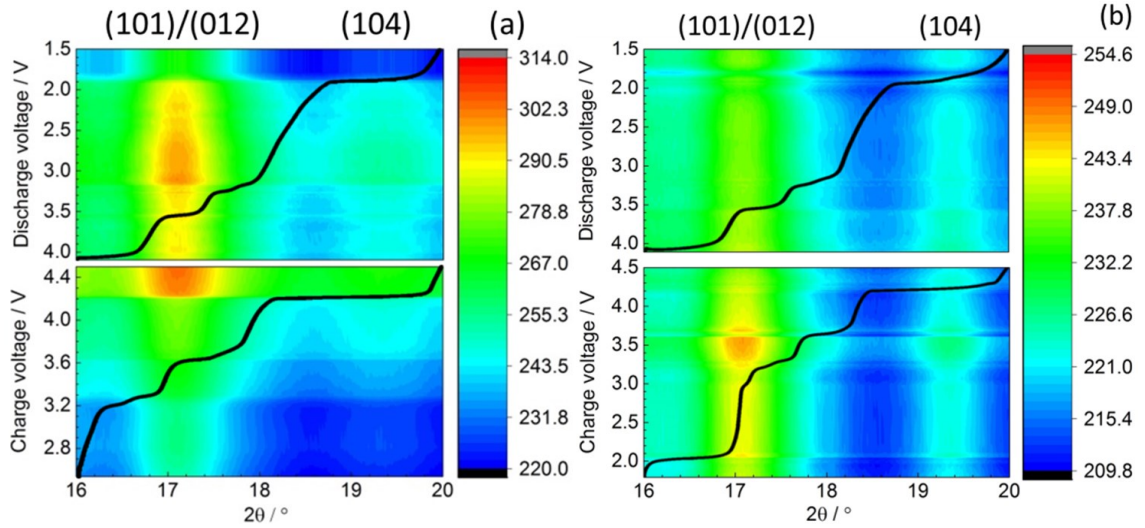


Fig. 4.7 Operando X-ray diffraction evolution of the normal (a) and the core-shell designed (b) P3-type $\text{Na}_{0.67}\text{Mn}_{0.67}\text{Ni}_{0.33}\text{O}_2$ with charge and discharge curves at 0.1 C (1 C = 100 $\text{mAh}\cdot\text{g}^{-1}$) in the voltage range 2.0 - 4.1 V.

As shown in Fig. 4.7(a), there are two peaks of high intensity located at the diffraction angles $2\theta = 17.2^\circ$ and 19.4° which, respectively, represent (101)/(012) and (104) reflections of the normal P3-type $\text{Na}_{0.67}\text{Mn}_{0.67}\text{Ni}_{0.33}\text{O}_2$ in agreement with the hexagonal crystal structure with $R3m$ space group. All plateaus of the charge and discharge curves in Fig. 4.7(a) are connected to the phase evolution of the normal P3-type $\text{Na}_{0.67}\text{Mn}_{0.67}\text{Ni}_{0.33}\text{O}_2$ observed as variations in intensity and width of (101)/(012) and (104) reflections during charge and discharge. During charge, constant intensity and width of (101)/(012) reflection in the voltage range 2.6 - 3.2 V are observed, though some Na ions must have been extracted from the normal P3-type material and contribute the charge capacity. Elevating the voltage to 3.6 V, the width of the (101)/(012) reflection increases. The intensity of (101)/(012) and (104) reflections in the voltage range 3.6 - 4.2 V slightly increases. At the charge voltage of 4.2 V, the intensity of (101)/(012) reflection sharply increases and the (104) reflection disappears.

After charge to 4.5 V, the voltage was switched off and the battery was rested for 10 min. We observe the intensities of the (101)/(012) reflection at discharge voltage of 4.1 V is smaller than that after charge to 4.5 V and the (104) reflection appear after the rest time.

In the discharge voltage range 4.1 - 3.2 V, the intensity variation of the (101)/(012) and (104) reflections remains relatively constant, while the width of the (104) reflection decreases during discharge to 3.6 V and then increases during discharge to 3.2 V. At discharge voltage of 3.2 V, the intensity of (101)/(012) reflection suddenly increases. During discharge from 3.2 to 1.9 V, the tapered width of (101)/(012) and (104) reflections is observed. At discharge voltage of 1.9 V, the intensity of (101)/(012) reflection drastically decreases. And the (104) reflection disappears after discharge to 1.9 V.

As shown in Fig. 4.7(b), two main reflection peaks, located at the diffraction angles $2\theta = 17.1^\circ$ and 19.3° , represent the (101)/(012) and (104) reflections of the core-shell designed $\text{Na}_{0.67}\text{Mn}_{0.67}\text{Ni}_{0.33}\text{O}_2$ indexed by the hexagonal crystal structure with $R3m$ space group. The initial voltage during charge of the core-shell designed P3-type $\text{Na}_{0.67}\text{Mn}_{0.67}\text{Ni}_{0.33}\text{O}_2$ (1.8 V) is lower than that of the normal P3-type material (2.5 V). Although Na atoms are extracted from the core-shell designed P3-type material in the charge voltage between 1.8 and 2.0 V, the changes in intensity and width of the (101)/(012) and (104) reflections remains relatively constant. In the charge voltage between 2.0 and 3.0 V, the extracted number of Na is smaller than in the charge voltage range 1.8 - 2.0 V and the intensity and the width of the (101)/(012) reflection remain constant. In the charge voltage between 3.0 and 4.5 V, the charge curve of the core-shell designed P3-type material reveals three plateaus which occur around 3.2, 3.6 and 4.1 V. The similar plateaus in the normal P3-type material are observed in Fig. 4.7(a). However, the XRD patterns demonstrates different changes in intensity and width of the (101)/(012) and (104) reflections between the core-shell and the normal P3-type materials. In the charge voltage 3.2 - 3.6 V, the intensity of the (101)/(012) and (104) reflections increases with charge voltage and the width of those reflections becomes wider. The intensity of the (101)/(012) and (104) reflections drop down sharply at charge voltage of 3.7 V. In the charge voltage range 3.7 - 4.2 V, the width of the (101)/(012) and (104) reflections becomes smaller with increase of voltage. In the charge voltage range 4.2 - 4.5 V, the width of the (104) reflection remains relatively constant and is larger than that at 4.2 V.

After charge, the cell of the core-shell designed P3-type material was rested for 10 min. We only observe slight increase in width of the (104) reflection. The difference in intensity of the (101)/(012) and (104) reflections is relatively small before and after the rest time. This trend is different from the normal P3-type material.

The discharge curve of the core-shell designed P3-type $\text{Na}_{0.67}\text{Mn}_{0.67}\text{Ni}_{0.33}\text{O}_2$ demonstrates plateaus similar to those of the normal P3-type material. However, we observe different changes in intensity and width of the (101)/(012) and (104) reflections in Fig. 4.7(b) during discharge of the core-shell designed P3-type material. In the discharge voltage range 4.1 - 3.6 V, the changes of the (101)/(012) reflection in intensity and width are unobvious, while the width of the (104) reflections becomes narrow with decreasing voltage. In the voltage range 3.6 - 2.1 V, we cannot observe obvious changes in intensity and width of the (101)/(012) and (104) reflections. At discharge voltage of 2.1 V, the intensity of the (101)/(012) reflection increases, while that of the (104) reflections decreases. In the discharge voltage range 2.0 - 1.8 V, the intensity of the (101)/(012) and (104) reflections is similar to that in the voltage range 3.5 - 2.1 V and remains relatively constant. At discharge voltage of 1.7 V, we observe increase in intensity of the (101)/(012) and decrease in intensity of (104) reflections again. With discharge voltage decreasing to 1.5 V, the width of the (101)/(012) reflections increases slightly, while the intensity of the (101)/(012) and (104) reflections remains constant.

4.3 Discussion

During the preparation of the core-shell designed P3-type $\text{Na}_{0.67}\text{Mn}_{0.67}\text{Ni}_{0.33}\text{O}_2$, the total molar ratio between Mn and Ni is constant and the same as for the normal P3-type material. In the normal P3-type material, the ordered arrangement of Mn and Ni exists in one TMO_2 layer. After core-shell design, the distribution of Mn and Ni is different from the core and the shell. Hence, the distribution of Mn and Ni in the core-shell designed P3-type material is regarded as disordered arrangement of Mn and Ni. The similar XRD patterns of the normal and the core-shell designed P3-type materials indicate the same crystal structure between the normal and the core-shell designed P3-type materials. Generally, the crystal structure of Na_xTMO_2 is determined by the annealing temperature, the type of TM , the ratio between different types of TM and the concentration of Na^[10-14]. Here, we confirm the structure of $\text{Na}_{0.67}\text{Mn}_x\text{Ni}_{1-x}\text{O}_2$ is only affected by the annealing temperature rather than by the changes in concentration of Mn and Ni.

The particles on the surface of the core-shell designed P3-type material are smaller than that of the normal P3-type material. As the Mn and the Ni ratio is the only parameter which differs in the core and the shell we assign the smaller particle size in the shell to

the higher Mn to Ni ratio on the surface. Obviously, the higher concentration of Mn in $\text{Na}_{0.67}\text{Mn}_x\text{Ni}_{1-x}\text{O}_2$ is supposed to refine the particles.

We observe a gradient in the concentration of Mn from the core to the shell in Fig. 4.2(e). This indicates the existence of core-shell structure in the special designed P3-type material. However, it is difficult to confirm the existence of gradient concentration of Ni by EDX. One reason is that the diffusion of Ni is faster than that of Mn in the core-shell designed P3-type material^[105]. After annealing at 700 °C, the distribution of Ni is supposed to be uniform from the core to the shell. In addition, the pores inside of the core-shell designed P3-type materials and the aggregation of nanoscale particles affects the accuracy of EDX measurements. In the following, we observe increase in the initial discharge capacity of the gradient core-shell P3-type $\text{Na}_{0.67}\text{Mn}_{0.67}\text{Ni}_{0.33}\text{O}_2$ in the voltage range 1.5 - 4.5 V and improvement in the cycling performance of this material in the voltage 2.0 - 4.1 V. This is supposed to be a result of the existence of the core-shell structure.

In the core-shell designed material, the average valences of Mn and Ni remains the same as those in the normal P3-type material observed as the same energy positions of Mn and Ni K-edge in normal and core-shell designed $\text{Na}_{0.67}\text{Mn}_{0.67}\text{Ni}_{0.33}\text{O}_2$. In consideration of electroneutrality of the Ni rich core, the Mn rich shell and the whole core-shell particle, the increasing number of Mn^{4+} is expected to be the same as the increasing number of Mn^{2+} which is half of the decreasing number of Mn^{3+} . The concentration changes of Ni^{2+} , Ni^{3+} and Ni^{4+} is presumably the same variation trend as that of Mn. The increasing number of Ni^{2+} is equal to that of Ni^{4+} which is half of the decreasing number of Ni^{3+} . According to the literature, Ni atoms in Na_xTMO_2 are oxidized to Ni^{4+} during charge and Mn atoms are reduced to Mn^{3+} during discharge^[90, 124]. That indicates Ni^{4+} and Mn^{4+} are hardly oxidized to higher valence states and contribute the charge capacity of the core-shell designed P3-type $\text{Na}_{0.67}\text{Mn}_{0.67}\text{Ni}_{0.33}\text{O}_2$. Similarly, the Ni^{2+} and Mn^{2+} are hardly reduced to provide the discharge capacity of the core-shell designed P3-type material. This is assumed to be one reason for lower capacities of the core-shell designed P3-type material in the voltage range 2.0 - 4.1 V. In addition, the concentration of Mn^{2+} and Ni^{2+} in the core-shell designed P3-type $\text{Na}_{0.67}\text{Mn}_{0.67}\text{Ni}_{0.33}\text{O}_2$ are larger than those in the normal P3-type material which is responsible for the larger capacities during the cycling of the gradient core-shell designed P3-type material in the voltage range of 1.5 - 4.5 V.

Besides, the different charge distribution in the core-shell designed material affects the cycling performance of it. During charge, Mn^{4+} and Ni^{4+} are difficultly oxidized which indicates Na would not diffuse to the vacancies around TM^{4+} . The structural changes of TM^{4+}O_6 units are relatively small in comparison with TM^{3+}O_6 and TM^{2+}O_6 units. This indicates smaller dimensional changes of TMO_6 units and is responsible for smaller capacity fading during charge. Similarly, the structural changes of TM^{2+}O_6 units during discharge are relatively small in comparison with TM^{3+}O_6 and TM^{4+}O_6 units due to low reduction activity of Ni^{2+} and Mn^{2+} during discharge.

According to structural investigation of P3-type $\text{Na}_{2/3}\text{Mg}_{1/3}\text{Mn}_{2/3}\text{O}_2$, NaO_6 units transform from prismatic structure into octahedral structure during charge and transform back to prismatic structure during discharge^[118]. Fig. 4.8 schematically illustrates the crystal structure changes of the normal P3-type $\text{Na}_{0.67}\text{Mn}_{0.67}\text{Ni}_{0.33}\text{O}_2$ during charge to 4.5 V and discharge to 1.5 V, respectively.

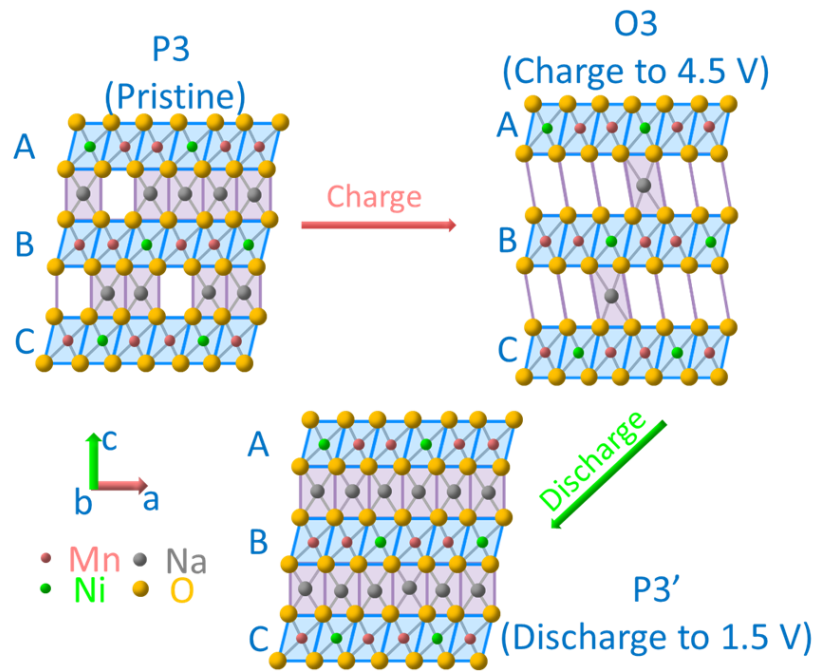


Fig. 4.8 Schematic structure images of the normal P3-type $\text{Na}_{0.67}\text{Mn}_{0.67}\text{Ni}_{0.33}\text{O}_2$ at different charge and discharge states

In the normal P3-type material, Na atoms occupy at the center of prismatic NaO_6 units and TM atoms occupy at the center of octahedral TMO_6 units. After charge to 4.2 V, the P3 phase starts to transform into the O3 phase. At charge voltage of 4.5 V, the main phase is O3 phase. The occupancy of Na sites is octahedral structure accompanying by the structural change between TMO_2 layers. The compression of O3 phase compared with P3 phase is a result of the shrinkage of TMO_2 layers within the a - b plane. After

discharge, the occupancy of Na sites transforms back to prismatic sites. The number of Na atoms in the P3' phase after discharge to 1.5 V is larger than that of the P3 phase in the pristine state. According to the *operando* XRD results of the normal P3-type $\text{Na}_{0.67}\text{Mn}_{0.67}\text{Ni}_{0.33}\text{O}_2$, see Fig. 4.7, the intensity of the (101)/(012) reflections sharply increases and the (104) reflection disappears at the charge voltage of 4.2 V indicating the P3 phase has mainly converted to the O3 phase. The transition from the P2 phase to the O2 phase also occurs during charge of P2-type $\text{Na}_{2/3}\text{Mn}_{2/3}\text{Ni}_{1/3}\text{O}_2$ to 4.2 V accompanied by the disappearance of the (104) reflection^[122, 141]. At 4.4 V, about 87% of the P3 phase in $\text{Na}_{2/3}\text{Mg}_{1/3}\text{Mn}_{2/3}\text{O}_2$ transformed into the O3 phase^[118]. Avoiding the phase transition between prismatic and octahedral phases during charge is expected to be an effective way for better cycling performance, which also explains the reason for larger capacity retention of the normal P3-type $\text{Na}_{0.67}\text{Mn}_{0.67}\text{Ni}_{0.33}\text{O}_2$ in the voltage range 2.0 - 4.1 V in comparison with the voltage range 1.5 - 4.5 V. Because of the extraction of Na ions, the omission of electrostatic attraction between Na and O ions is supposed to result in larger distance between TMO_2 layers.

Although the initial charge and discharge curves of the normal and the core-shell designed P3-type material demonstrates similar plateaus in the voltage range 1.5 - 4.5 V, see Fig. 4.4. The *operando* XRD patterns during the first cycle of these two materials are different from each other. Some people reported the plateaus during the cycling are results of second phase transition and the changes between two plateaus is a result of solid solution^[118]. The phase transitions between the P3 and the O3 phases are regarded as changes in structure of NaO_6 units. In combination of the electrochemical and *operando* XRD results in Fig. 4.7, part of the P3 phase in the core-shell designed material is assumed to transform into the O3 phase during charge to 3.6 V. This phase transition voltage is lower than that of the normal P3-type material. In addition, the O3 phase transforms back to the P3 phase at charge voltage 3.7 V which is not observed during charge of the normal P3-type material.

According to the investigation of dimensional changes in TMO_6 units of the normal P3-type $\text{Na}_{0.67}\text{Mn}_{0.67}\text{Ni}_{0.33}\text{O}_2$, the changes in structure of NaO_6 units at different voltage are affected by the dimensional changes of MnO_6 or NiO_6 units located above or below this NaO_6 unit, respectively. That means, the changes in concentration of Mn and Ni have impact on different dimensional and structural changes in NaO_6 units during cycling of the core-shell designed P3-type material.

In consideration of the gradient in concentration of Mn in the core-shell designed P3-type material, the changes in intensity and width of reflections in XRD patterns of the core-shell designed P3-type material is expected to reflect the diffusion of Na between the core, the interlayer, the shell and the electrolyte, which is schematically illustrated in Fig. 4.9. The light green, light red and dark red hexagons represent the Ni rich core, the interlayer and the Mn rich shell of the core-shell designed P3-type $\text{Na}_{0.67}\text{Mn}_{0.67}\text{Ni}_{0.33}\text{O}_2$, respectively. The ratio of Mn and Ni in the interlayer is between that in the core and that in the shell. The light blue part stands for the electrolyte. The red dotted boxes mark the electrochemical active layers at relevant voltages in which the diffusion of Na leads to phase transition in this layer.

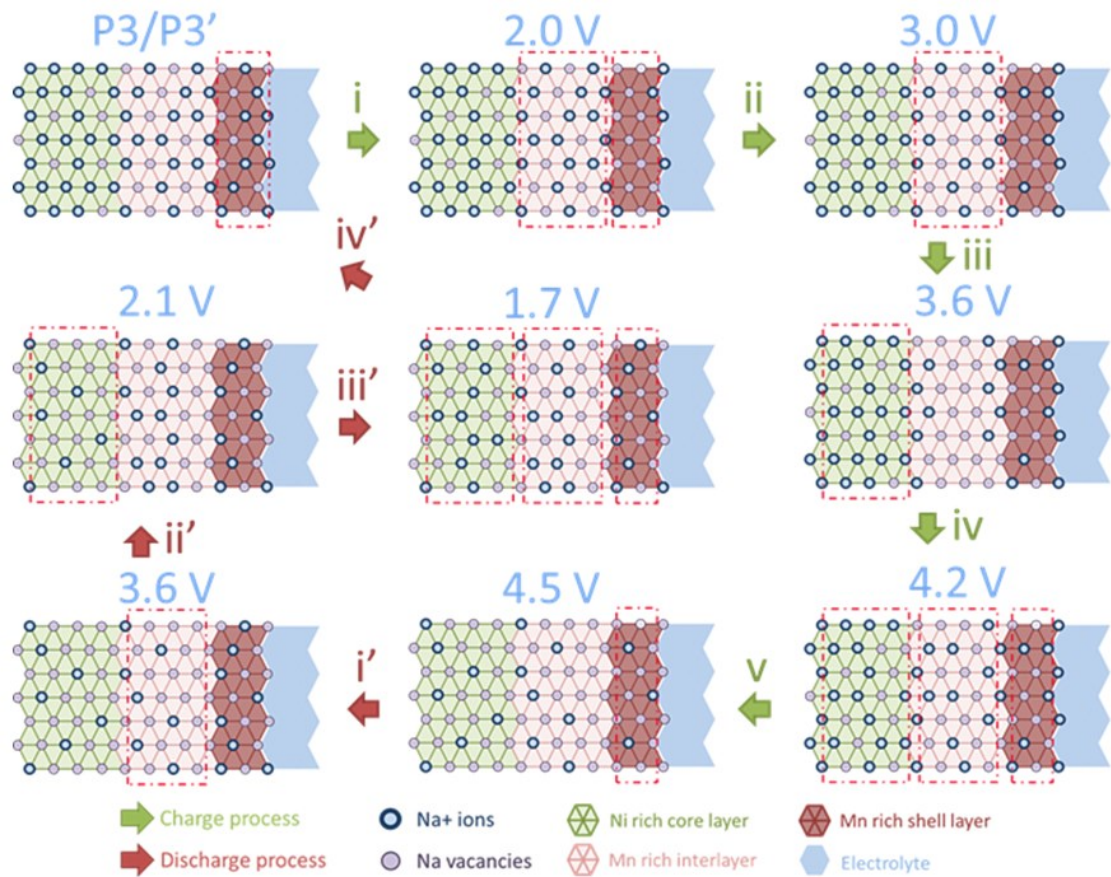


Fig. 4.9 Schematic diagram of Na diffusion in the gradient core-shell designed P3-type $\text{Na}_{0.67}\text{Mn}_{0.67}\text{Ni}_{0.33}\text{O}_2$ during the first cycle at 0.1 C

The migration of Na in the core-shell designed material during charge is assumed to be generalized into 5 steps. Na atoms are extracted from the surface of the core-shell designed P3-type particles to the electrolyte which produces Na vacancies on the surface below the charge voltage of 2.0 V. In the voltage range of 2.0 - 3.0 V, Na atoms in the interlayer diffuse into the Mn rich shell. The increasing number of the Na vacancies in the Mn rich interlayer does not change the structure of intermediate layer.

In the voltage range of 3.0 - 3.6 V, the number of Na vacancies in the interlayer increases. Some prismatic NaO_6 unit transform into octahedral units. At the charge voltage of 3.6 V, Na ions diffusing from the Ni rich core into the intermediate layer partially occupy at Na vacancies in the interlayer, which leads to octahedral NaO_6 units transform to prismatic units. In the charge voltage range of 4.2 - 4.5 V, the migration of Na ions between the core, interlayer, shell and the electrolyte keeps dynamic balance.

During discharge, the insertion of Na ions from the electrolyte and diffusion between the outer to the inner layers is assumed to be summarized into four steps with the intensity and width variation of the (101)/(012) and (104) reflections. Before discharging to 3.6 V, Na ions insert into the surface of the core-shell designed material. In the discharge voltage range of 3.6 - 2.1 V, the amount of Na ions inserted from electrolyte keeps almost the same as that of Na ions diffused between the Mn rich shell and intermediate layers. With further discharge, Na ions migrate into the Ni rich core at the discharge voltage of 2.1 V. The migration of Na ions between the Mn rich shell, the interlayer and the Ni rich core remains relative constantly which makes the occupancy of Na sites transfer into prismatic structure. The amount of re-inserted Na ions becomes larger than that in the pristine core-shell designed material when the discharge voltage reduces to 1.7 V.

The phase transition of the normal and the core-shell designed P3-type materials is not only ascribed to the glide of TMO_2 layers but also to the dimensional changes in TMO_2 layers. When the expansion or shrinkage of two TMO_6 units within the a - b plane, located above and below one NaO_6 unit, are identical to each other, the structure of NaO_6 in the P3 phase remains as prismatic but the dimension of these NaO_6 units would be affected, observed as elongation or compression along the c axis. When the dimensional changes of these two TMO_6 units within the a - b plane are different from each other, the prismatic NaO_6 units reveal distortion firstly and then transfer into octahedral structure or the octahedral NaO_6 reveal distortion and then transfer into prismatic structure. The reason for better cycling performance of the core-shell designed P3-type $\text{Na}_{0.67}\text{Mn}_{0.67}\text{Ni}_{0.33}\text{O}_2$ will be further discussed by investigating the changes in TMO_6 units in the core-shell designed P3-type $\text{Na}_{0.67}\text{Mn}_{0.67}\text{Ni}_{0.33}\text{O}_2$ in the next chapter.

4.4 Conclusions

In this chapter, we discuss the effect of core-shell design in P3-type $\text{Na}_{0.67}\text{Mn}_{0.67}\text{Ni}_{0.33}\text{O}_2$. The core-shell designed P3-type $\text{Na}_{0.67}\text{Mn}_{0.67}\text{Ni}_{0.33}\text{O}_2$ consists of Ni rich core and Mn

rich shell. In order to reduce the energy consumption, the preparation temperature was further decreased to 700 °C. Although the crystal structure of the gradient core-shell designed P3-type material is also indexed using $R3m$ space group. The XRD pattern of the core-shell designed P3-type material is similar to that of the normal P3-type material. The morphology and the electrochemical performance of the normal and the core-shell designed P3-type material are different from each other.

The core-shell designed P3-type $\text{Na}_{0.67}\text{Mn}_{0.67}\text{Ni}_{0.33}\text{O}_2$ has larger initial capacities in the voltage range 1.5 - 4.5 V and better cycling performance in the voltage range 2.0 - 4.1 V in comparison with the normal P3-type $\text{Na}_{0.67}\text{Mn}_{0.67}\text{Ni}_{0.33}\text{O}_2$. The capability of the core-shell designed P3-type $\text{Na}_{0.67}\text{Mn}_{0.67}\text{Ni}_{0.33}\text{O}_2$ is better than that of the normal P3-type material, especially at 20 C ($1\text{ C} = 100\text{ mA}\cdot\text{g}^{-1}$) in the voltage ranges 1.5 - 4.5 V and 2.0 - 4.1 V. Meanwhile, the core-shell designed P3-type $\text{Na}_{0.67}\text{Mn}_{0.67}\text{Ni}_{0.33}\text{O}_2$ shows longer cycling life and better capacity retention at different charge rates (0.1 C and 20 C).

Although the charge and discharge curves of the core-shell designed P3-type $\text{Na}_{0.67}\text{Mn}_{0.67}\text{Ni}_{0.33}\text{O}_2$ are similar to those of the normal P3-type $\text{Na}_{0.67}\text{Mn}_{0.67}\text{Ni}_{0.33}\text{O}_2$, the phase evolution of the core-shell designed P3-type material is different from that of the normal P3-type material which confirms the existence of core-shell structure. During the cycling of the normal P3-type $\text{Na}_{0.67}\text{Mn}_{0.67}\text{Ni}_{0.33}\text{O}_2$, we observe P3-O3 phase transition during charge and O3-P3' phase transition during discharge. During the cycling of the core-shell designed P3-type material, the occupancy of Na sites transfers from prismatic structure to octahedral structure in the charge voltage range 3.2 - 3.6 V and octahedral NaO_6 units transfer back to prismatic units at charge voltage of 3.7 V. The different phase transitions of the normal and the core-shell designed P3-type materials are ascribed to different diffusivity of Na in the Ni rich core, interlayer and the Mn rich shell.

5 Fast charge and discharge in P3-type $\text{Na}_{0.67}\text{Mn}_{0.67}\text{Ni}_{0.33}\text{O}_2$

5.1 Motivation

The feasibility of the core-shell design in Na_xTMO_2 for sodium ion batteries has been confirmed in the last chapter. However, the reasons for better cycling performance after core-shell design in Na_xTMO_2 materials should be further investigated.

In addition, the requirement of energy storage systems suitable for the fast cycling is flourishing with the industrialization of electric and hybrid electric vehicles. For instance, the mobile charge stations should provide fast charge service as quickly as possible to reduce the waiting time. On the other hand, the batteries of vehicles should be suitable for fast charge and keep working after fast charge. In the recent past, extensive investigations of anodes for sodium ion batteries during fast charge and discharge have been performed, while promising cathode material during fast cycling is seldom reported^[69, 142-144].

Considering the influence of the dimensional changes in TMO_2 layers on cycling performance of Na_xTMO_2 , the goal of the present chapter is to figure out the reason for better cycling performance in core-shell design Na_xTMO_2 materials from the sight of local structure changes around TM atoms. We intentionally prepared the core-shell designed P3-type $\text{Na}_{0.67}\text{Mn}_{0.67}\text{Ni}_{0.33}\text{O}_2$ in two steps, which are illustrated in section 2.1.3. Beside, we investigate the cycling performance of this material as cathode for sodium ion batteries during fast charge and discharge. XANES spectra at Mn and Ni K-edge are

measured to compare the redox mechanism of Mn and Ni ions during the fast and slow charge and discharge. The reason for better cycling performance of P3-type $\text{Na}_{0.67}\text{Mn}_{0.67}\text{Ni}_{0.33}\text{O}_2$ with core-shell structure is quantitatively investigated by EXAFS spectroscopy from the sight of the dimensional changes of TMO_2 layers.

5.2 Results

5.2.1 Characteristics

Fig. 5.1 illustrates the difference between the core-shell designed and the normal P3-type $\text{Na}_{0.67}\text{Mn}_{0.67}\text{Ni}_{0.33}\text{O}_2$ by XRD and powder images.

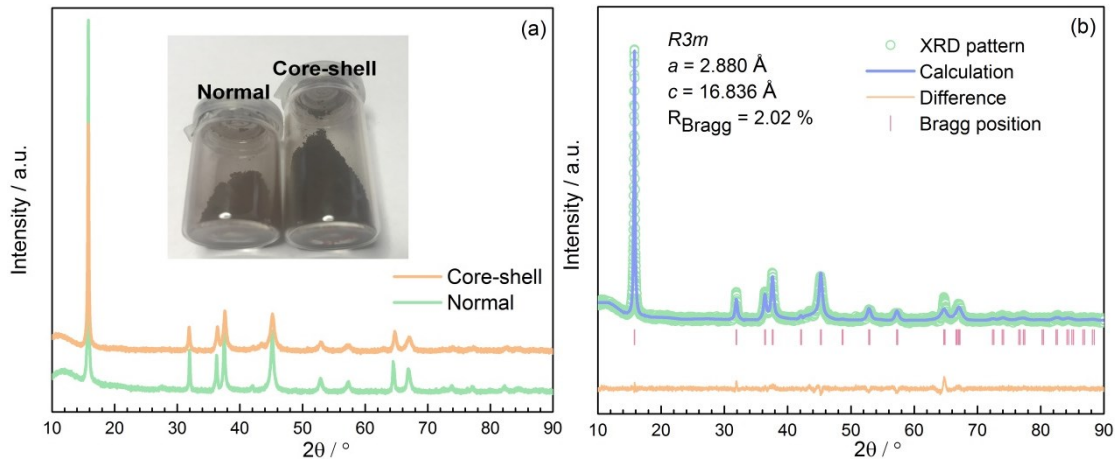


Fig. 5.1 X-ray diffraction patterns and powder images of the normal and the core-shell designed P3-type $\text{Na}_{0.67}\text{Mn}_{0.67}\text{Ni}_{0.33}\text{O}_2$ (a) and Rietveld refinement result of the core-shell designed P3-type $\text{Na}_{0.67}\text{Mn}_{0.67}\text{Ni}_{0.33}\text{O}_2$

The core-shell designed and the normal P3-type $\text{Na}_{0.67}\text{Mn}_{0.67}\text{Ni}_{0.33}\text{O}_2$ materials were synthesized at the same temperature (700 °C) for 24 hours. As shown in Fig. 5.1(a), the color of the core-shell designed P3-type $\text{Na}_{0.67}\text{Mn}_{0.67}\text{Ni}_{0.33}\text{O}_2$ powders is darker than that of the normal P3-type powders. The XRD pattern of the core-shell designed P3-type $\text{Na}_{0.67}\text{Mn}_{0.67}\text{Ni}_{0.33}\text{O}_2$ is similar to that of the normal P3-type material. The similar peak positions in XRD patterns indicate the similar crystal structure between the core-shell designed and the normal P3-type materials. The reflection peaks in XRD pattern of the normal P3-type material are relatively sharp and narrow while those of the core-shell designed P3-type material are broad. As shown in Fig. 5.1(b), the crystal structure of the core-shell designed material is consistent with that of P3-type $\text{Na}_{0.67}\text{TMO}_2$, which is indexed by the hexagonal crystal structure using the $R3m$ space group^[125]. The lattice parameters of the core-shell designed P3-type material determined by Rietveld refinement are $a = 2.880 \text{ \AA}$ and $c = 16.836 \text{ \AA}$.

Fig. 5.2 illustrates the morphology of the normal and the core-shell designed P3-type $\text{Na}_{0.67}\text{Mn}_{0.67}\text{Ni}_{0.33}\text{O}_2$ recorded by SEM. The morphology of the core-shell designed P3-type $\text{Na}_{0.67}\text{Mn}_{0.67}\text{Ni}_{0.33}\text{O}_2$ is heterogeneous while that of the normal P3-type material is homogeneous. We observe the aggregation of particles, on the scale of tens of nanometers, on the surface of the core-shell designed material. The particle size of the normal P3-type material is several hundred nanometers. The molar ratio between Mn and Ni in the normal P3-type material is 2.28 and that in the core-shell designed P3-type material is 2.12. These two values are close to the stoichiometric ratio between Mn and Ni in the normal and the core-shell designed P3-type $\text{Na}_{0.67}\text{Mn}_{0.67}\text{Ni}_{0.33}\text{O}_2$. Here, these two materials are regarded as P3-type $\text{Na}_{0.67}\text{Mn}_{0.67}\text{Ni}_{0.33}\text{O}_2$

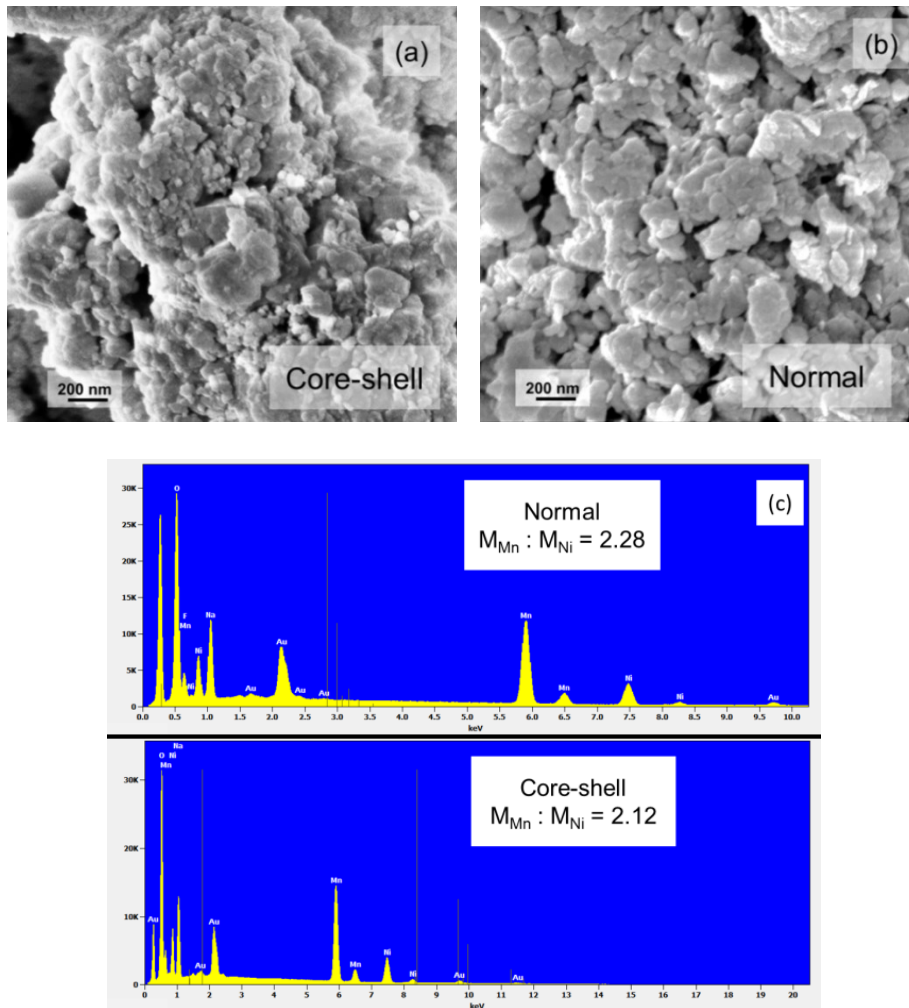


Fig. 5.2 Scanning electron microscopy images of the core-shell designed (a) and the normal (b) P3-type $\text{Na}_{0.67}\text{Mn}_{0.67}\text{Ni}_{0.33}\text{O}_2$ and results of energy dispersive X-ray spectroscopy measurements on these two materials (c)

In order to cut particles of the core-shell designed and the normal P3-type materials, we used focused ion beam (FIB) technique. Fig. 5.3 illustrates the cross section of the core-shell designed and the normal P3-type $\text{Na}_{0.67}\text{Mn}_{0.67}\text{Ni}_{0.33}\text{O}_2$ recorded by SEM. We

observe pores within two different P3-type particles. The cross section of this P3-type material without core-shell structure is different from that of the normal P3-type material introduced in chapter 4, see Fig. 4.2(d) and Fig. 5.3(b). This is ascribed to different raw materials. We synthesized the normal P3-type material by different salts of transition metals, see section 2.1.2. As shown in Fig. 5.3, the inner part of the core-shell designed material is less consolidated than that of the normal P3-type material. The smaller particles existing on the surface of the core-shell designed material are observed within of the core-shell designed particle.

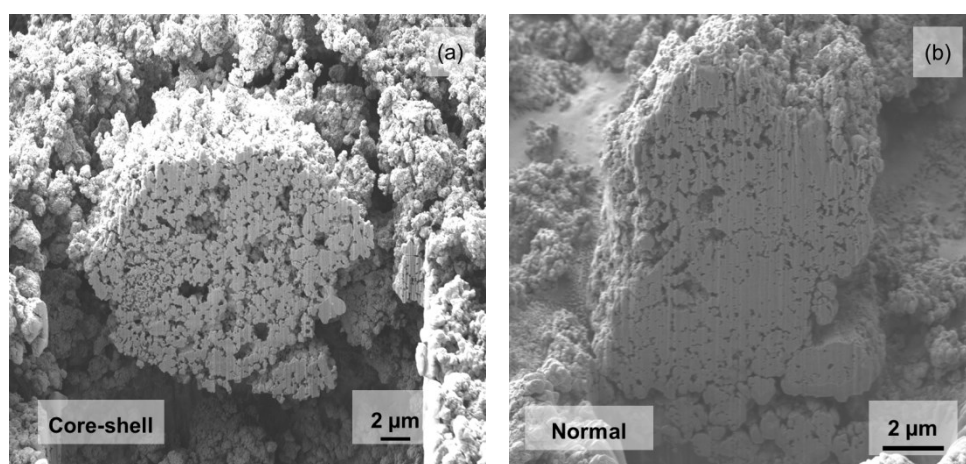


Fig. 5.3 Cross section of the gradient core-shell designed (a) and the normal (b) P3-type $\text{Na}_{0.67}\text{Mn}_{0.67}\text{Ni}_{0.33}\text{O}_2$

In the last chapter, the concentration gradient of Ni in the core-shell designed P3-type $\text{Na}_{0.67}\text{Mn}_{0.67}\text{Ni}_{0.33}\text{O}_2$ cannot be confirmed by EDX on the cross section of aggregated particles, though the electrochemical performance is improved and the structure evolution is changed after the core-shell design. Hence, we performed TEM and EDX together to explore the existence of Ni rich particles in the core-shell designed P3-type material

Fig. 5.4 illustrates TEM images of the gradient core-shell designed and the normal P3-type particles. The range of the molar ratio between Mn and Ni is from 1.37 to 1.79 in the normal P3-type material, illustrated in Fig. 5.4(a), which is smaller than the result in Fig. 5.2(c). However, we can qualitatively compare the difference in concentration of Mn and Ni between the normal and the core-shell designed materials. In Fig. 5.4(a), the molar ratio between Mn and Ni in the center of particles, marked as point 1, 2 and 3, is slightly larger than that in the normal P3-type particles illustrated in Fig. 5.4(b). This indicates the concentration of some particles in P3-type material is larger in the core-shell designed material. The largest molar ratio between Mn and Ni is observed on the

edge of nanoscale particles, marked as point 4, 5 and 6. We observe larger concentration of Ni at point 7 and 8, which confirms the existence of Ni rich part in the core-shell designed material.

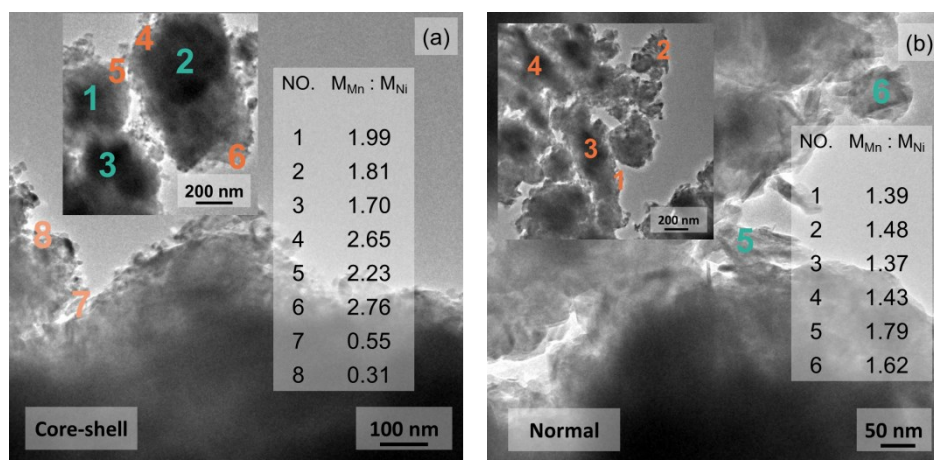


Fig. 5.4 Transmission electron microscopy images with energy dispersive X-ray spectroscopy results at different points of the core-shell designed (a) and the normal (b) P3-type $\text{Na}_{0.67}\text{Mn}_{0.67}\text{Ni}_{0.33}\text{O}_2$

5.2.2 Electrochemistry

In order to investigate the feasibility of the gradient core-shell designed material as cathodes for fast cycled sodium ion batteries, the electrochemical tests of this material were performed at different charge and discharge rates in the voltage range 2.0 - 4.1 V. We name charge and discharge process at different rates as nC and mD, respectively. “nC” represents charge to 4.1 V at n C rate ($n = 1$ or 20 , $1 \text{ C} = 100 \text{ mA} \cdot \text{g}^{-1}$) and “mD” represents discharge to 2.0 V at m C rate ($m = 1$ or 20), respectively.

Fig. 5.5 illustrates the charge and discharge curves of the core-shell designed P3-type $\text{Na}_{0.67}\text{Mn}_{0.67}\text{Ni}_{0.33}\text{O}_2$ in the voltage ranges 2.0 - 4.1 V at different rates in the 1st cycles and in the 4th cycle after cycling at 0.1 C for three cycles. As shown in Fig. 5.5(a), the initial charge capacities after 1C and 20C are 71 and 67 $\text{mAh} \cdot \text{g}^{-1}$, respectively. The capacity of the core-shell designed material during slow charge is 6% larger than that of fast charged material in the first cycle. After slow charge (1C), the initial discharge capacities are 83 $\text{mAh} \cdot \text{g}^{-1}$ after slow discharge (1C1D) and 71 $\text{mAh} \cdot \text{g}^{-1}$ after fast discharge (1C20D). The capacity gap between 1C1D and 1C20D is 12 $\text{mAh} \cdot \text{g}^{-1}$. After fast charge (20C), the initial discharge capacities are 79 $\text{mAh} \cdot \text{g}^{-1}$ after slow discharge (20C1D) and 64 $\text{mAh} \cdot \text{g}^{-1}$ after fast discharge (20C20D). The capacity gap between 20C1D and 20C20D is 15 $\text{mAh} \cdot \text{g}^{-1}$. That means, the core-shell designed P3-type

material lost 23% discharge capacity after the fast cycling (20C20D) in comparison with the slow cycling (1C1D) in the first cycle.

After three cycles at 0.1 C rate, the core-shell designed P3-type $\text{Na}_{0.67}\text{Mn}_{0.67}\text{Ni}_{0.33}\text{O}_2$ delivers charge capacities as 90 and 84 $\text{mAh}\cdot\text{g}^{-1}$ after 1C and 20C in the 4th cycle, respectively, shown in Fig. 5.5(b). The capacity of the core-shell designed material during slow charge is 7% larger than that of fast charge in the 4th cycle. The discharge capacity of the core-shell designed P3-type $\text{Na}_{0.67}\text{Mn}_{0.67}\text{Ni}_{0.33}\text{O}_2$ is 86 $\text{mAh}\cdot\text{g}^{-1}$ after 1C1D and decreases to 65 $\text{mAh}\cdot\text{g}^{-1}$ after 20C20D in the 4th cycle. This means, the core-shell designed material loses 25% discharge capacity during the fast cycling compared to that after the slow cycling.

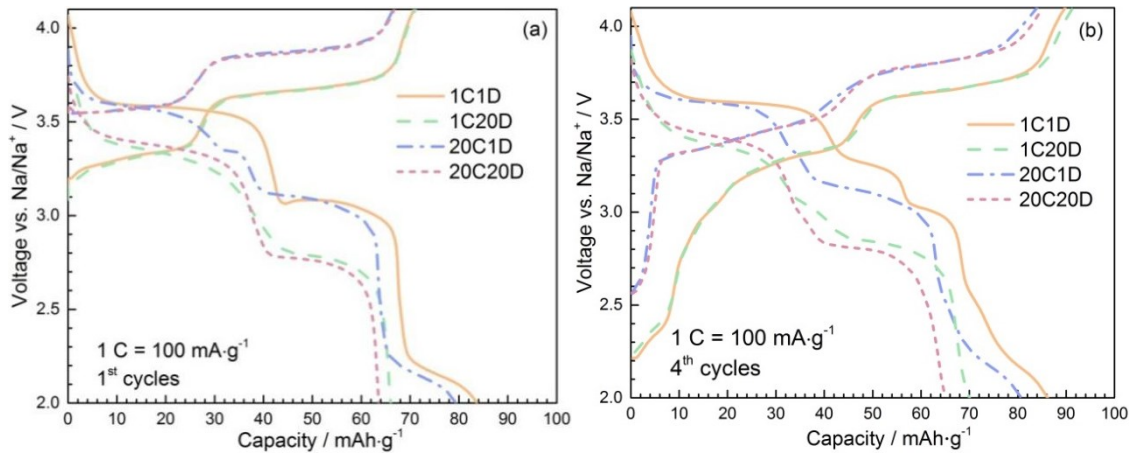


Fig. 5.5 Charge and discharge curves of the core-shell designed P3-type $\text{Na}_{0.67}\text{Mn}_{0.67}\text{Ni}_{0.33}\text{O}_2$ in the voltage range 2.0 - 4.1 V at different charge and discharge rates in the 1st cycles (a) and in the 4th cycles after cycling at 0.1 C for three cycles (b)

Fig. 5.6 illustrates the cycling performance of the core-shell designed P3-type material in the voltage range 2.0 - 4.1 V at charge rate of 1 C and discharge rates of 1 C and 20 C in comparison with the normal P3-type material. The capacities of the normal and the core-shell designed material both gradually decay during cycling with 1C1D. However, we observe increase in capacities of the normal and the core-shell designed P3-type materials in the first tens of cycles and then the capacities gradually decay during cycling with 1C20D. The capacities of the normal P3-type material during the first 50 cycles at 1C1D and 1C20D are higher than those of the core-shell designed material cycled under the same conditions. However, the capacity retentions of the core-shell designed material after 1C1D and 1C20D are both larger than those of the normal P3-type material cycled under the same conditions. The capacity retention of the core-shell designed P3-type $\text{Na}_{0.67}\text{Mn}_{0.67}\text{Ni}_{0.33}\text{O}_2$ is 90% after 350 cycles at 1C1D and 94% after

900 cycles at 1C20D in comparison with those after the 4th cycles under the same conditions, respectively.

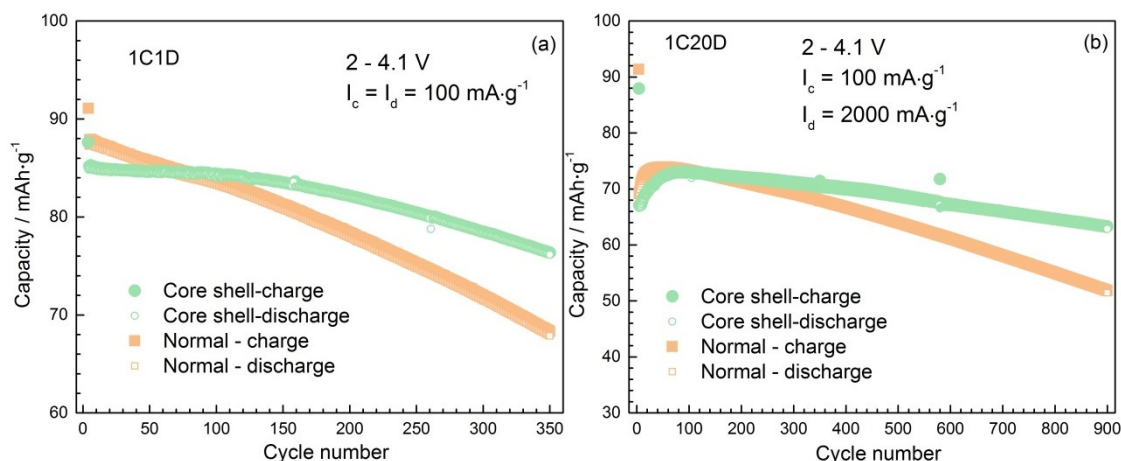


Fig. 5.6 Cycling performance of the core-shell designed P3-type $\text{Na}_{0.67}\text{Mn}_{0.67}\text{Ni}_{0.33}\text{O}_2$ in the voltage range 2.0 - 4.1 V after charge at 1 C and discharge at 1C from the 4th to the 350th cycles (a) and after charge at 1 C and discharge at 20 C from the 4th to the 900th cycle (b) in comparison with the normal P3-type $\text{Na}_{0.67}\text{Mn}_{0.67}\text{Ni}_{0.33}\text{O}_2$

Fig. 5.7 illustrates the cycling performance of the gradient core-shell designed P3-type material in the voltage range 2.0 - 4.1 V at charge rate of 20 C and discharge rates of 1 C and 20 C in comparison with the normal P3-type material.

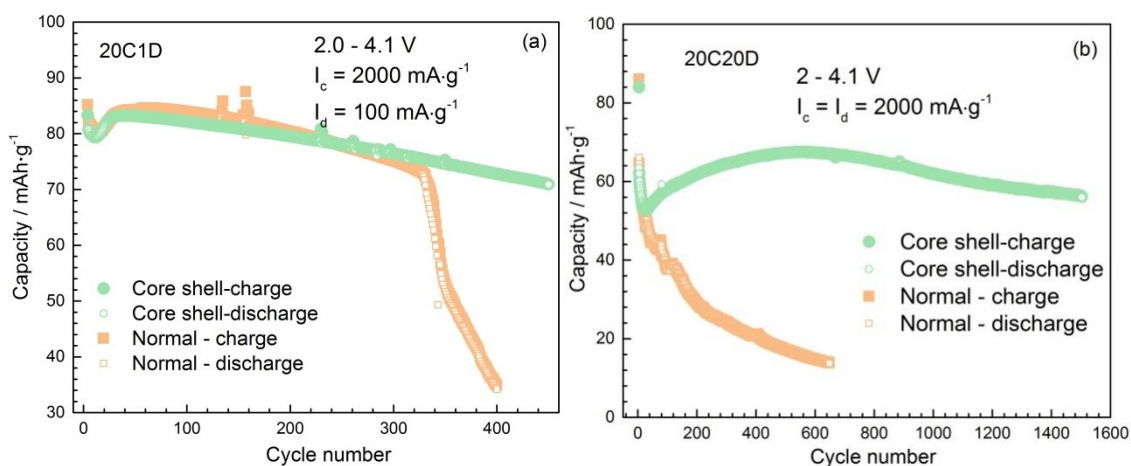


Fig. 5.7 Cycling performance of the core-shell designed P3-type $\text{Na}_{0.67}\text{Mn}_{0.67}\text{Ni}_{0.33}\text{O}_2$ in the voltage range 2.0 - 4.1 V after charge at 20 C and discharge at 1C from the 4th to the 450th cycle (a) and after charge at 20 C and discharge at 20 C from the 4th to the 1500th cycle (b) in comparison with the normal P3-type $\text{Na}_{0.67}\text{Mn}_{0.67}\text{Ni}_{0.33}\text{O}_2$

The cycling life of P3-type $\text{Na}_{0.67}\text{Mn}_{0.67}\text{Ni}_{0.33}\text{O}_2$ is obviously prolonged in the core-shell designed material during fast charge. We observe severe decrease and obvious increase in capacities during first tens of cycles of the core-shell designed material after 20C1D. Similar changes in capacities of the normal P3-type material are also observed during

20C1D. Then, the capacities of the normal P3-type material gradually decay and suddenly drop down after 340 cycles. The capacity of the core-shell designed P3-type material is $71 \text{ mAh}\cdot\text{g}^{-1}$ after 450 cycles and the discharge capacity retention of the core-shell designed material after 20C1D for 450 cycles is 88% in comparison with the 4th cycle of the core-shell designed material after 20C1D.

During cycling of the core-shell designed P3-type material with 20C20D, the capacity drastically decreases to $52 \text{ mAh}\cdot\text{g}^{-1}$ in the first 20 cycles, then gradually increases to $68 \text{ mAh}\cdot\text{g}^{-1}$ approaching the 600th cycle and slightly decreases to $56 \text{ mAh}\cdot\text{g}^{-1}$ approaching the 1500th cycles. The discharge capacity retention of the core-shell designed material is 89% after 1500 cycles in comparison with the discharge capacity in the 4th cycle. The capacity fading in the normal P3-type material is severe during fast charge and discharge and we cannot observe increase of capacity during the fast cycling.

5.2.3 XANES

Fig. 5.8 illustrates the normalized XANES spectra of the gradient core-shell designed P3-type $\text{Na}_{0.67}\text{Mn}_{0.67}\text{Ni}_{0.33}\text{O}_2$ at Mn and Ni K-edge after 1C, 1C1D and 1C20D process.

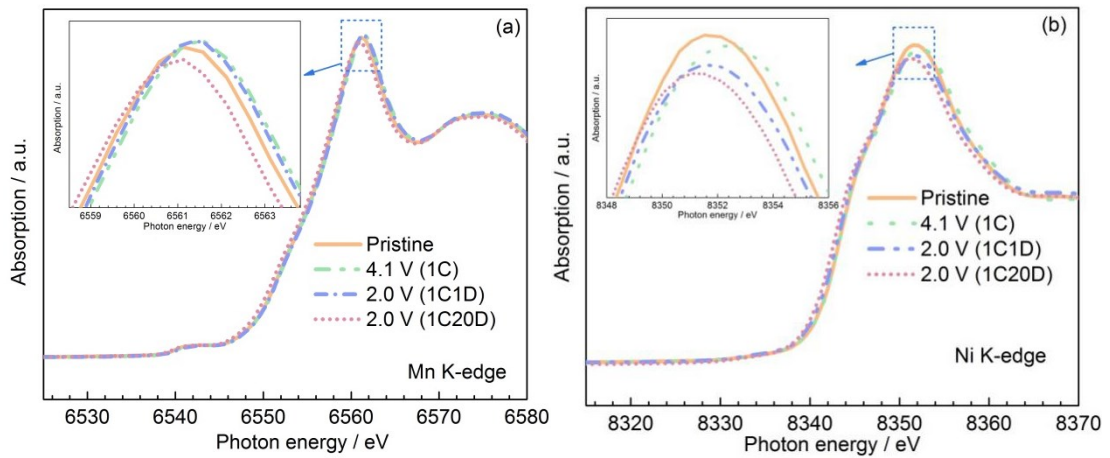


Fig. 5.8 Normalized X-ray absorption near edge structure spectra of the core-shell designed P3-type $\text{Na}_{0.67}\text{Mn}_{0.67}\text{Ni}_{0.33}\text{O}_2$ after the first cycle at 1 C charge rate (1 C = $100 \text{ mAh}\cdot\text{g}^{-1}$) at Mn (a) and Ni (b) K-edge

The obvious pre-edge of spectra at Mn K-edge, illustrated in Fig. 5.8(a), is related to the photoelectron transition from 1s to 3d orbital. The pre-edge is not obvious at the Ni K-edge of the core-shell designed P3-type $\text{Na}_{0.67}\text{Mn}_{0.67}\text{Ni}_{0.33}\text{O}_2$ at different charge and discharge states. The main peaks of the Mn and Ni K-edge correspond to the photoelectron transition from 1s to unoccupied 4p orbital. The energy position of the main peaks provides information about the average valence state of Mn and Ni in the

core-shell designed P3-type material at different states. After slow charge (1C), the main peaks of the Mn and Ni K-edge both shift to higher energy in comparison between the pristine material and the material after 1C. After slow discharge (1C1D), the energy position of Mn K-edge slightly shifts to low energy, while the shift of Ni K-edge from high energy to low energy is more visible. After fast discharge (1C20D), the energy position of the main peak at Mn K-edge at state of 1C20D is located at smaller energy position than that of the pristine state as well as that of the 1C1D state. The main peak at Ni K-edge of the 1C20D state is also located at lower energy in comparison with that of the pristine states and that of 1C1D state.

With regard to fast charge, the normalized XANES spectra of the gradient core-shell designed P3-type $\text{Na}_{0.67}\text{Mn}_{0.67}\text{Ni}_{0.33}\text{O}_2$ at Mn and Ni K-edge after 20C, 20C1D and 20C20D are illustrated in Fig. 5.9, respectively. During fast charge (20C), the energy of the main peak of the core-shell designed P3-type $\text{Na}_{0.67}\text{Mn}_{0.67}\text{Ni}_{0.33}\text{O}_2$ at the Mn and Ni K-edge shifts to higher energy, in comparison with the pristine state and the state of 20C. However, the energy position of Ni K-edge after 20C is smaller than that of Ni K-edge after 1C. After 20C1D and 20C20D, the energy of the main peaks at Mn K-edge shifts to the lower energy in comparison with that of the state after 20 C. The main peak at Mn K-edge is located at lower energy after 20C1D compared with that of the state of 20C20D. The main peak of the core-shell designed P3-type $\text{Na}_{0.67}\text{Mn}_{0.67}\text{Ni}_{0.33}\text{O}_2$ at Ni K-edge after 20C1D is located at energy position similar to that of the pristine state, while the energy position of the main peak at Ni K-edge after 20C20D is slightly lower than that of the pristine state. The lower energy position of Mn and Ni K-edge indicates lower average valence state of Mn and Ni in the core-shell designed P3-type material.

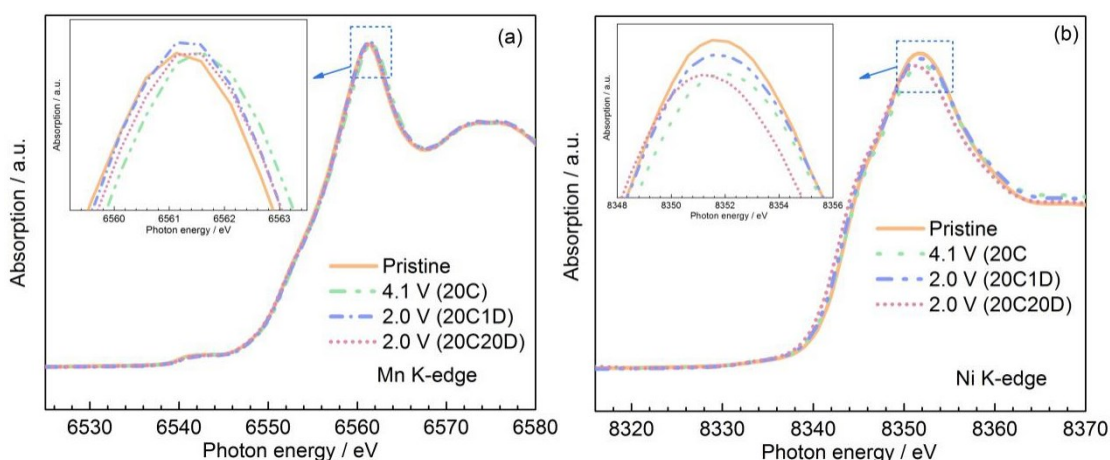


Fig. 5.9 Normalized X-ray absorption near edge structure spectra of the core-shell designed P3-type $\text{Na}_{0.67}\text{Mn}_{0.67}\text{Ni}_{0.33}\text{O}_2$ after the first cycle at 20 C charge rate (1 C = 100 $\text{mAh}\cdot\text{g}^{-1}$) at Mn (a) and Ni (b) K-edge

5.2.4 EXAFS

Fig. 5.10 illustrates the k^3 -weighted EXAFS data of the pristine gradient core-shell designed P3-type $\text{Na}_{0.67}\text{Mn}_{0.67}\text{Ni}_{0.33}\text{O}_2$ after Fourier transformation (FT) at the Mn K-edge with fitting curve in fitting range 1 - 4.9 Å.

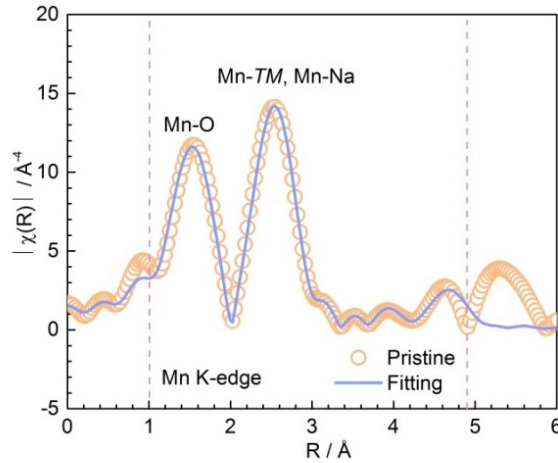


Fig. 5.10 Extended X-ray absorption fine structure spectra after Fourier transformation along with the fitting profiles of the core-shell designed P3-type $\text{Na}_{0.67}\text{Mn}_{0.67}\text{Ni}_{0.33}\text{O}_2$ at Mn K-edge in the pristine

The amplitude reduction factor (S_0^2) is determined as 0.86 ± 0.11 with R factor as 0.0049 by fitting of EXAFS data at Mn K-edge in the pristine core-shell designed P3-type $\text{Na}_{0.67}\text{Mn}_{0.67}\text{Ni}_{0.33}\text{O}_2$. The maximum in the range 1.0 - 2.0 Å is the result of photoelectron scattering from the absorbing Mn atom to the six nearest coordinated O atoms. The maximum in the range 2.0 - 3.0 Å comes from the scattering of photoelectrons between the absorbing Mn atom by the nearest occupied six *TM* and four Na atoms. Then, the amplitude reduction factor of EXAFS data at the Mn K-edge of the core-shell designed P3-type material in the pristine state are kept constant and utilized to assess the local structural changes around Mn during different charge and discharge. The calculated value of R factor at different charge and discharge states are smaller than 0.01 indicating the scattering model is physically reasonable to provide local coordination information around Mn in the gradient core-shell designed P3-type $\text{Na}_{0.67}\text{Mn}_{0.67}\text{Ni}_{0.33}\text{O}_2$ ^[112, 129].

Fig. 5.11 illustrate the k^3 -weighted EXAFS data of the core-shell designed P3-type $\text{Na}_{0.67}\text{Mn}_{0.67}\text{Ni}_{0.33}\text{O}_2$ at states of 1C, 1C1D and 1C20D after FT at the Mn K-edge with fitting curves in the fitting range 1 - 4.9 Å. The ratio between the first and second maxima is similar at different charge and discharge states.

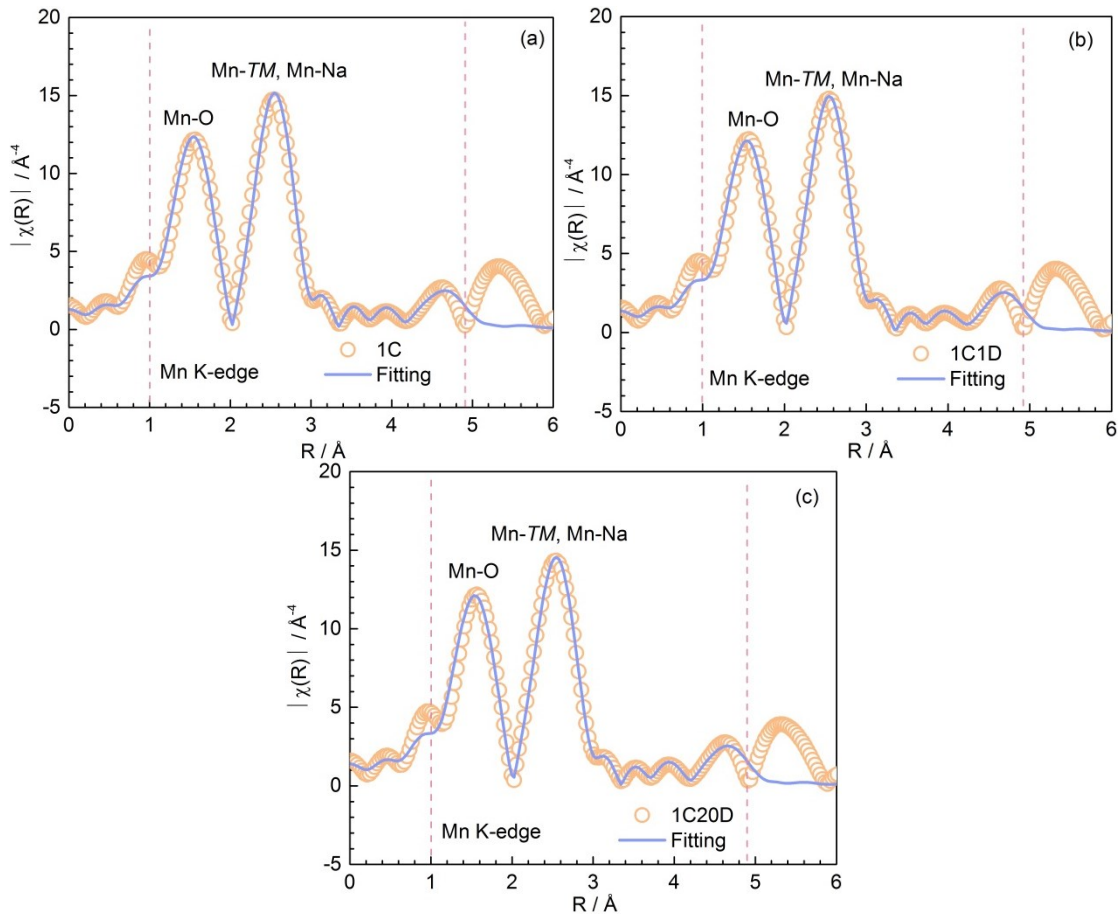


Fig. 5.11 Extended X-ray absorption fine structure spectra after Fourier transformation along with the fitting profiles of the core-shell designed P3-type $\text{Na}_{0.67}\text{Mn}_{0.67}\text{Ni}_{0.33}\text{O}_2$ at Mn K-edge at voltage state of 4.1 V after 1C (a), 2.0 V after 1C1D (b) and 2.0 V after 1C20D (c)

Fig. 5.12 shows the k^3 -weighted EXAFS data of the gradient core-shell designed P3-type $\text{Na}_{0.67}\text{Mn}_{0.67}\text{Ni}_{0.33}\text{O}_2$ at states of 20C, 20C1D and 20C20D after FT at the Mn K-edge with fitting curves in the fitting range 1 - 4.9 Å.

The maxima in the range 1 - 2 Å in Fig. 5.11 and Fig. 5.12 are also affected by photoelectron scattering between the absorbing Mn and six O atoms in the first coordination shell. The maxima in the range 2 - 3 Å in Fig. 5.11 and Fig. 5.12 are the result of photoelectron scattering between Mn and atoms in the second coordination shell, which consist of four Na atoms and six TM atoms. The changes in amplitude and position of maxima in Fig. 5.11 and Fig. 5.12 are not obvious at different charge and discharge states. The ratio between the first and the second maxima are smaller than 1 in the pristine state and at different charge and discharge states in Fig. 5.10 - Fig. 5.12.

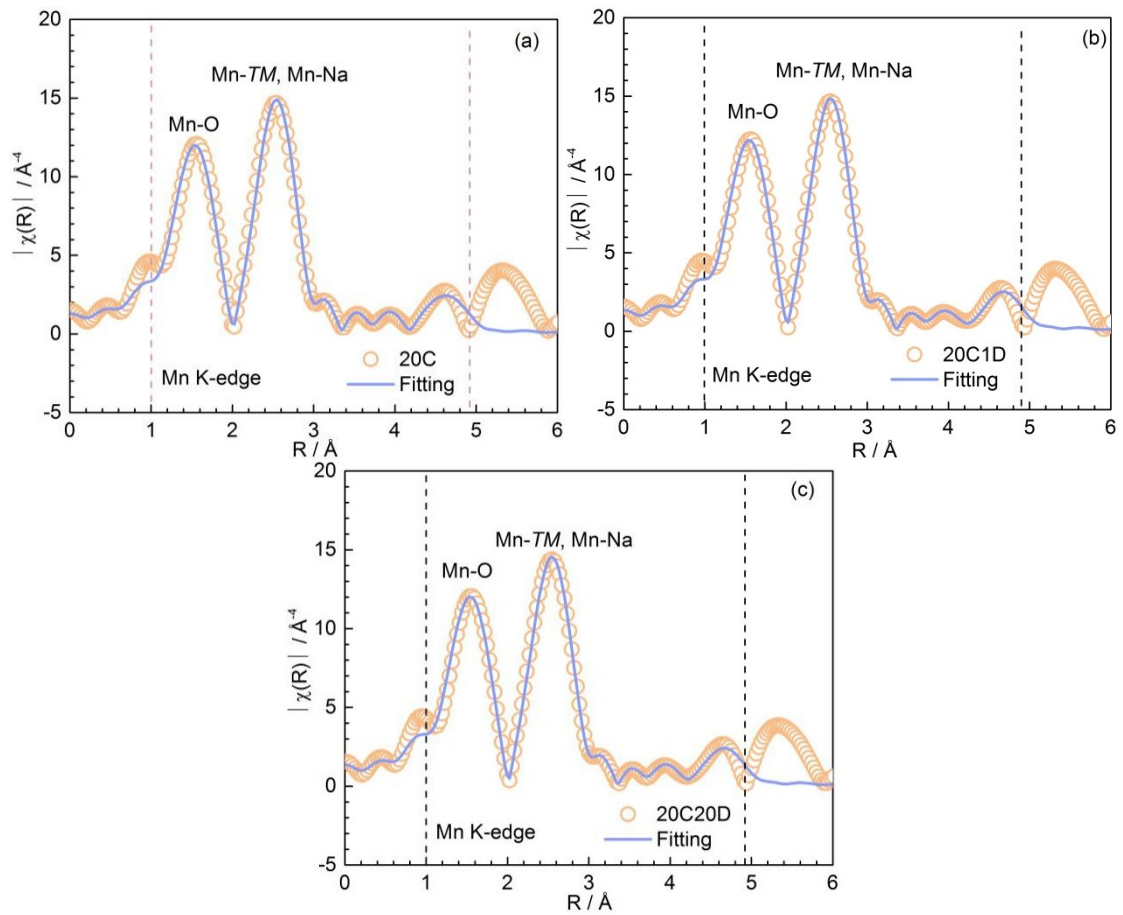


Fig. 5.12 Extended X-ray absorption fine structure spectra after Fourier transformation along with fitting profiles of the core-shell designed P3-type $\text{Na}_{0.67}\text{Mn}_{0.67}\text{Ni}_{0.33}\text{O}_2$ at Mn K-edge at voltage state of 4.1 V after 20C (a), 2.0 V after 20C1D (b) and 2.0 V after 20C20D (c)

Fig. 5.13 illustrate the k^3 -weighted EXAFS data of the pristine gradient core-shell designed P3-type $\text{Na}_{0.67}\text{Mn}_{0.67}\text{Ni}_{0.33}\text{O}_2$ after FT at the Ni K-edge with fitting curve in fitting range 1 - 4.9 Å. The amplitude reduction factor of Ni in the pristine core-shell designed P3-type $\text{Na}_{0.67}\text{Mn}_{0.67}\text{Ni}_{0.33}\text{O}_2$ is determined as $S_0^2 = 0.99 \pm 0.08$ with R factor $R = 0.0018$. The maximum in the range 1.0 - 2.0 Å is affected by photoelectron scattering from the absorbing Ni atom to the six nearest coordinated O atoms. The maximum in the range 2.0 - 3.0 Å is a result of the scattering of photoelectrons between the absorbing Ni atom by the nearest occupied six TM and four Na atoms. Then, the amplitude reduction factor of Ni is kept constant for all states of the core-shell designed P3-type $\text{Na}_{0.67}\text{Mn}_{0.67}\text{Ni}_{0.33}\text{O}_2$. The scattering model which is used to fit the EXAFS data after FT of the Ni K-edge is utilized to determine the local structural changes around Ni at different charge and discharge states. The calculated value of the R factor at the Ni K-edge of the core-shell designed P3-type $\text{Na}_{0.67}\text{Mn}_{0.67}\text{Ni}_{0.33}\text{O}_2$ at different charge and discharge states are smaller than 0.01. The results thus provide physical reliable local

structure information around Ni in the gradient core-shell designed P3-type $\text{Na}_{0.67}\text{Mn}_{0.67}\text{Ni}_{0.33}\text{O}_2$ ^[112, 129].

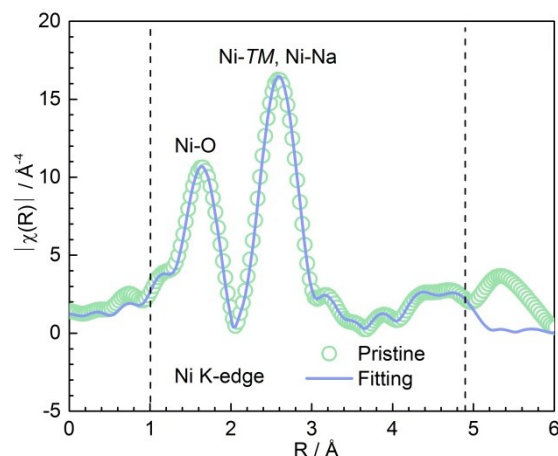


Fig. 5.13 Extended X-ray absorption fine structure spectra after Fourier transformation along with the fitting profiles of the core-shell designed P3-type $\text{Na}_{0.67}\text{Mn}_{0.67}\text{Ni}_{0.33}\text{O}_2$ at Ni K-edge in the pristine

Fig. 5.14 illustrate the k^3 -weighted EXAFS data of the gradient core-shell designed P3-type $\text{Na}_{0.67}\text{Mn}_{0.67}\text{Ni}_{0.33}\text{O}_2$ at the states of 1C, 1C1D, 1C20D, 20C, 20C1D and 20C20D after FT at the Ni K-edge with fitting curves in the fitting range 1 - 4.9 Å, respectively. The maxima in the range 1 - 2 Å in Fig. 5.14 are related to the photoelectron scattering between Ni and six O atoms in the nearest coordination shell. The maxima in the range 2 - 3 Å are affected by the scattering of photoelectrons from the absorbing Ni to the nearest coordinated six *TM* and four O atoms.

During charge, no matter whether slow charged (1C) or fast charged (20C), the amplitude of the maxima in the range 1 - 2 Å decreases at Ni K-edge after FT. During discharge, both after 20D and 1D, the amplitude of the maxima in the range 1 - 2 Å at Ni K-edge after FT slightly increases. The changes in amplitude of maxima in the range 2 - 3 Å at the Ni K-edge after FT are not obvious after 1C, 20C, 1C1D, 1C20D and 20C20D in comparison with the maximum in the same range of the pristine state. We observe increase in amplitude of the maximum in the range 2 - 3 Å at the Ni K-edge and mismatch in the range 1.0 - 1.1 Å between the data and the fit after 20C1D.

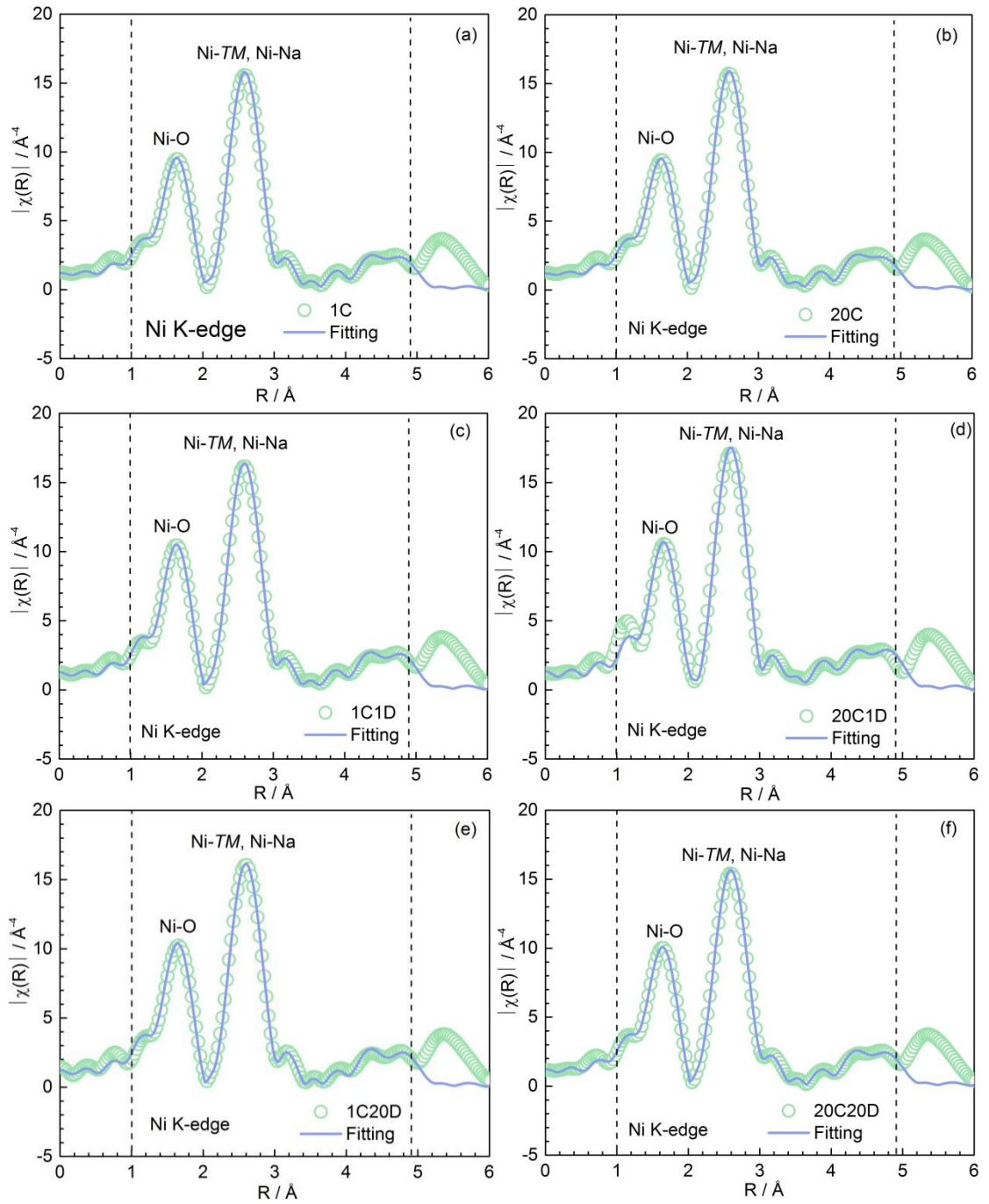


Fig. 5.14 Extended X-ray absorption fine structure spectra after Fourier transformation along with the fitting profiles of the core-shell designed P3-type $\text{Na}_{0.67}\text{Mn}_{0.67}\text{Ni}_{0.33}\text{O}_2$ at Ni K-edge at voltage state of 4.1 V after 1C (a), 4.1 V after 20C (b), 2.0 V after 1C1D (c), 2.0 V after 20C1D (d), 2.0 V after 1C20D and 2.0 V after 20C20D

The structural changes of MnO_6 and NiO_6 units during different charge and discharge according to the fitting results of EXAFS data at Mn and Ni K-edge are schematically illustrated in Fig. 5.15. In the pristine state of the core-shell designed P3-type $\text{Na}_{0.67}\text{Mn}_{0.67}\text{Ni}_{0.33}\text{O}_2$, the length of Ni-O bonds is 2.067 ± 0.005 Å which is longer than that of Mn-O bonds (1.900 ± 0.007 Å). The distance between Ni and TM is 2.906 ± 0.007 Å which is longer than that between Mn and TM (2.866 ± 0.009 Å). In

combination of crystal structure of the P3 phase and the local structure around *TM*, the angles between Mn-O and Ni-O bonds are calculated as 97.6° and 89.8°, respectively.

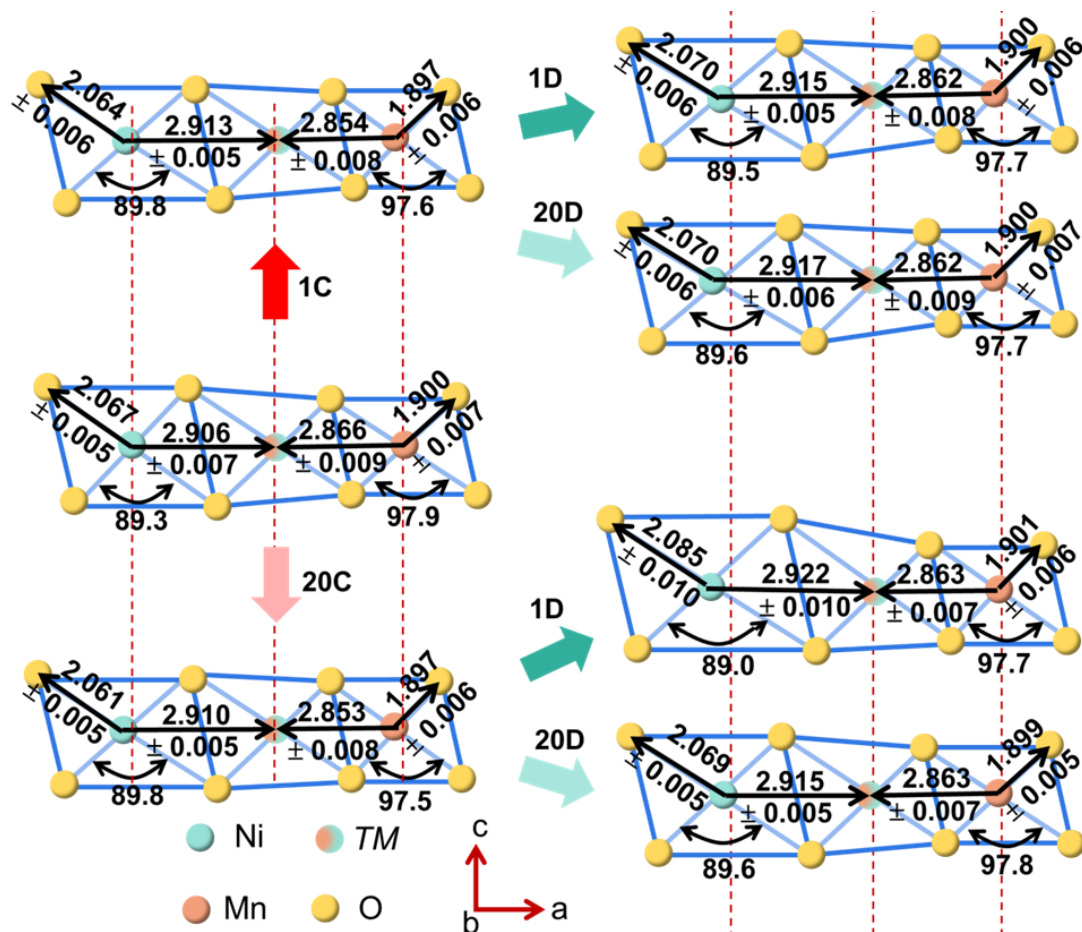


Fig. 5.15 Schematic depiction of the structural variation of TMO_6 units in the core-shell designed P3-type $Na_{0.67}Mn_{0.67}Ni_{0.33}O_2$ after different charge to 4.1 V and discharge to 2.0 V

First, we compare the local structure around Mn and Ni in the core-shell designed P3-type $Na_{0.67}Mn_{0.67}Ni_{0.33}O_2$ after slow charge. In comparison with the pristine state, the length of Ni-O and the distance between Ni and *TM* after 1C increase to 2.064 ± 0.006 and 2.913 ± 0.005 Å, respectively. The angle between Ni-O bonds increases to 89.8°, respectively. With regards to MnO_6 units, the length of Mn-O and the distance between Mn and *TM* after 1C decrease to 1.897 ± 0.006 and 2.854 ± 0.008 Å, respectively. The angle between Mn-O decreases to 97.6°.

At the state of 1C1D, the length of Ni-O bonds and the distance between Ni and *TM* are determined as 2.070 ± 0.006 and 2.915 ± 0.005 Å, respectively. The angle between Ni-O bonds is calculated as 89.5°. The length of Mn-O bonds and the distance between Mn and *TM* are 1.900 ± 0.006 and 2.862 ± 0.008 Å, respectively. The angle between Mn-O bonds is calculated as 97.7° at the state of 1C1D.

The average dimension and shape of MnO_6 units at the state of 1C20D is the same with those of MnO_6 units at the state of 1C1D, though the uncertainty in length of Mn-O bonds and distance between Mn and *TM* is slightly different from each other. The average length of Ni-O bonds at the state of 1C20D is the same with that of at the state of 1C1D, while the average distance between Ni and *TM* and the average angle between Ni-O bonds are slightly different from those of the state of 1C1D.

Then, we compare the local structural changes around Mn and Ni in the core-shell designed P3-type $\text{Na}_{0.67}\text{Mn}_{0.67}\text{Ni}_{0.33}\text{O}_2$ after fast charge. In comparison with pristine state, the length of Ni-O and the distance between Ni and *TM* after 20C increase to 2.061 ± 0.005 and 2.910 ± 0.005 Å, respectively. The changes in average interatomic distance are smaller than those after 1C. The calculated angle between Ni-O bonds after 20C is the same with that after 1C and increases to 89.8° . With regard to MnO_6 units, the length of Mn-O bonds after 20C is the same with that after 1C and decreases to 1.897 ± 0.006 Å. During fast charge, the distance between Mn and *TM* decreases to 2.853 ± 0.008 Å and the calculated angle between Mn-O bonds increases to 89.8° .

After 20C1D, the length of Ni-O bonds and the distance between Ni and *TM* are 2.085 ± 0.010 and 2.922 ± 0.010 Å, respectively. The angle between Ni-O bonds is calculated as 89.0° . The length of Mn-O bonds and the distance between Mn and *TM* after 20C1D are 1.901 ± 0.006 and 2.863 ± 0.007 Å, respectively. The angle between Mn-O bonds is calculated as 97.7° after 20C1D.

The average dimension of NiO_6 units after 20C20D is smaller than that of 20C1D within the *a-b* plane, which is observed as shorter length of Ni-O bonds (2.915 ± 0.005 Å) and smaller distance between Ni and *TM* (2.069 ± 0.005 Å). The decrease in average angle between Mn-O is smaller at the state of 20C20D in comparison with the state of 20C1D. The length of Mn-O bonds and the distance between Mn and *TM* at the state of 20C20D are 1.899 ± 0.005 and 2.863 ± 0.007 Å, respectively.

5.3 Discussion

The core-shell design in P3-type $\text{Na}_{0.67}\text{Mn}_{0.67}\text{Ni}_{0.33}\text{O}_2$ improves the cycling performance not only during slow charge and discharge but also for fast charge and discharge, and especially prolongs the cycling life of this material during fast charge. Although the electrochemical performance of P3-type $\text{Na}_{0.67}\text{Mn}_{0.67}\text{Ni}_{0.33}\text{O}_2$ is obviously improved by the core-shell design, it is difficult to confirm the existence of the core-shell structure

within P3-type $\text{Na}_{0.67}\text{Mn}_{0.67}\text{Ni}_{0.33}\text{O}_2$. The invisible concentration gradient of Ni is ascribed to the faster diffusion of Ni at 700 °C in comparison with Mn which is reported in the core-shell designed cathode for lithium ion batteries^[104]. There are two other reasons for unobvious core-shell structure in the core-shell designed P3-type $\text{Na}_{0.67}\text{Mn}_{0.67}\text{Ni}_{0.33}\text{O}_2$. One is ascribed to the existence of pores within the core-shell designed P3-type particle which affects the accuracy of concentration between Mn and Ni by EDX measurements. The other one is the different molar ratio between Mn and Ni exist in nanoscale particles, observed in Fig. 5.4. When these particles with different molar ratio between Mn and Ni aggregate together, the molar ratio between Mn and Ni in the aggregated particles is supposed to be average value of those of each nanoscale particle, which is hardly observed using EDX.

In addition, the capacity gap of the core-shell designed P3-type $\text{Na}_{0.67}\text{Mn}_{0.67}\text{Ni}_{0.33}\text{O}_2$ between different cycling rates, which is observed as smaller capacity during the fast cycling, still limits the practical utilization of the core-shell designed P3-type $\text{Na}_{0.67}\text{Mn}_{0.67}\text{Ni}_{0.33}\text{O}_2$ for fast cycling. The different capacities of the core-shell designed P3-type $\text{Na}_{0.67}\text{Mn}_{0.67}\text{Ni}_{0.33}\text{O}_2$ during the fast and slow cycling is related to different redox activity of Mn and Ni, which is compared by energy position of Mn and Ni K-edge in Fig. 5.8 and Fig. 5.9, respectively.

During slow charge (1C), the energy of Mn and Ni K-edge shifts to higher energy position which indicates the capacity during slow charge of the core-shell designed P3-type material is contributed by oxidation of Mn and Ni. The lower average valence state of Mn and Ni is observed after 1C20D rather than after 1C1D, reflected as lower energy position of Mn and Ni K-edge. This is inconsistent with electrochemistry result during the first cycle of 1C20D and 1C1D. The lower average valence state of Mn and Ni after 1C20D indicates larger reduction activity of Ni and Mn which is supposed to provide larger discharge capacity of the core-shell designed P3-type material during fast discharge.

During fast charge (20C), Mn and Ni are also oxidized to higher valence state observed as energy shift towards to higher energy of Mn and Ni K-edge, respectively. In comparison with the energy position of the main peaks at Mn K-edge, the energy positions of the Mn K-edge are similar after 1C and 20C. This indicates the oxidation of Mn is similar after fast and slow charge. However, the energy of the main peak at the Ni K-edge is smaller after 20C than that after 1C. This indicates the lower charge capacity

of the core-shell designed P3-type material after fast charge is supposed to be a result of lower oxidation activity of Ni. The reduction activity of Ni is larger after 20C20D than that of 20C1D, observed as larger energy shift of the main peak from the high energy to the low energy at the Ni K-edge. However, the reduction activity of Mn is slightly smaller after 20C20D than that after 20C1D. Due to the limitation of XANES, it is difficult to quantitatively compare the charge compensation of Mn and Ni to the capacity of the core-shell designed P3-type material after 20C1D and 20C20D.

The energy positions of Mn and Ni K-edge after 1C20D, see Fig. 5.8, are both lower than those of the state of 20C1D (Fig. 5.9). This indicates lower average valence state of Mn and Ni which is supposed to provide higher discharge capacity after 1C20D rather than after 20C1D. However, the opposite electrochemical results are illustrated in Fig. 5.5. There are several possible reasons for these inconsistent XANES and electrochemical results. One is the redox of O compensates charge and contributes to the capacity. The other one is the diffusion path of Na is different between fast and slow cycling. During fast discharge, more Na atoms prefer to occupied around Ni^{3+} and Mn^{3+} and reduce Ni^{3+} or Mn^{3+} to Ni^{2+} or Mn^{2+} , respectively. During slow charge, Na ions prefer to coordinate around Ni^{4+} and reduce Ni^{4+} to Ni^{3+} or around Mn^{4+} and reduce Mn^{4+} to Mn^{3+} . This indicates the diffusion of Na between TM^{3+} is easier than that between TM^{4+} during the fast discharge and it affects the capacity of the core-shell designed P3-type $\text{Na}_{0.67}\text{Mn}_{0.67}\text{Ni}_{0.33}\text{O}_2$ at different discharge rates. However, we cannot qualitatively confirm the number of reduced TM^{3+} and TM^{4+} ions during fast and slow cycling of the core-shell designed P3-type material by XANES. The diffusion path of Na and the redox activity of oxygen in the core-shell designed P3-type material is urgently to be figured out in the future.

In the following, the local structural changes around Mn and Ni are quantitatively compared to elucidate the reason for improvement of core-shell design in P3-type $\text{Na}_{0.67}\text{Mn}_{0.67}\text{Ni}_{0.33}\text{O}_2$ during the fast and slow cycling.

Firstly, the preferential occupancy of Na around Ni, which is discussed in the normal P3-type $\text{Na}_{0.67}\text{Mn}_{0.67}\text{Ni}_{0.33}\text{O}_2$ in the chapter 3, cannot be observed in the core-shell designed P3-type material. This indicates the preferential occupancy of Na around Ni in P3-type material is hindered by the core-shell design. Due to the core-shell design, the distribution of Mn and Ni is disordered resulting in different charge distribution in comparison with that of the normal P3-type material. In the core-shell designed P3-type

material, Na can both occupy around Mn and Ni. That means, the changes in electrostatic interaction between Ni and TMO_6 units accompanying by the extraction and insertion of Na become smaller. This leads to smaller dimensional changes of NiO_6 units caused by the extraction and insertion of Na.

According to the conclusion in the chapter 3, the shrinkage and expansion of TMO_2 layers, respectively, during charge and discharge within the a - b plane is responsible for capacity fading during the cycling. The average distance between Mn and TM in the core-shell designed material is slightly smaller, no matter during fast charge or slow charge, which indicates better structural stability of MnO_6 units in the core-shell designed P3-type $Na_{0.67}Mn_{0.67}Ni_{0.33}O_2$. We observe slightly stretch of average distance between Ni and TM during fast and slow charge of the core-shell designed material. This indicates NiO_6 units are going to slightly expand within the a - b plane. This indicates smaller dimensional changes of TMO_2 layers within the a - b plane during charge of the core-shell designed P3-type material and improve the cycling performance of it.

During fast and slow charge, the average length of Ni-O and Mn-O bonds slightly decreases. The oxidation of TM leads to larger electrostatic attraction between TM and O, which is supposed to stretch the distance between TM and O. If O atoms are oxidized during charge, the electrostatic attraction between TM and O becomes smaller resulting in longer interatomic distance between TM and O. In consideration of electrostatic interaction between Na and TMO_6 units, TMO_6 units are expected to be compressed accompanying with extraction of Na and be elongated accompanying by the insertion of Na. Hence, the slight decline in average length of TM -O bonds indicates the electrostatic interaction between TM and O keeps a balance accompanied by the extraction of Na and the oxidation of TM and O. Independently of the discharge rates, the average length of Mn-O and Ni-O bonds both slightly increases. This reflects the core-shell design improves the structural stability of P3-type material. The dimensional changes of Mn-O and Ni-O bonds, caused by the reduction activity of Mn and Ni atoms and the insertion of Na, are offset by each other.

The dimension of NiO_6 units at the state of 20C1D is larger than other NiO_6 units at the state of 1C1D, 1C20D and 20C20D. The longest Ni-O and Ni- TM bonds after 20C1D is supposed to be a result of the cation mixing between Ni and Na in the core-shell designed P3-type $Na_{0.67}Mn_{0.67}Ni_{0.33}O_2$ ^[141, 145]. After 20C1D, some TM occupancy sites

in TMO_2 layers are occupied by Na ions, while those Ni atoms occupied at occupancy of Na sites reveal larger electrostatic attraction prolonging the distance between Ni and O in NiO_6 units at the state of 20C1D.

The dimensional changes of NiO_6 and MnO_6 units in the core-shell designed P3-type material, not only interatomic distance but also the bond angle, are much smaller than that in the normal P3-type material indicating better structural stability, which provide better cycling performance of P3-type material.

5.4 Conclusions

In this chapter, the core-shell designed P3-type material is utilized as a promising cathode for ultrafast sodium ion batteries, which is a result of better structural stability of TMO_2 layers. The cycling retention of this special P3-type material is 94% after 900 cycles of slow charge and fast discharge and 89% after 1500 cycles of fast charge and fast discharge. Mn and Ni are both oxidized during fast and slow charge and reduced during fast and slow discharge. This compensates a part of charge in the core-shell designed P3-type material. The preferential occupancy of Na around Ni in the normal P3-type material is hindered. Na atoms in the core-shell designed P3-type materials occupy around Mn and Ni. The dimensional changes of MnO_6 and NiO_6 units in the core-shell designed P3-type material are much smaller than those in the normal P3-type material. During fast cycling, the MnO_6 and NiO_6 units in the core-shell designed P3-type material also reveal outstanding structural stability. The stable structure of TMO_6 units is ascribed to the dimensional compensation caused by the extraction and insertion of Na and the redox of TM and O and leads to stable structure of TMO_2 layers. This is the reason for better cycling performance of the core-shell designed P3-type material.

6 Conclusions

We synthesized different P2-type and P3-type $\text{Na}_{0.67}\text{Mn}_{0.67}\text{Ni}_{0.33}\text{O}_2$ materials at different temperatures, investigated the reason for capacity fading in P3-type materials and designed a special synthesis method which improves the electrochemical performance of P3-type material.

- The synthesis temperature of P3-type $\text{Na}_{0.67}\text{Mn}_{0.67}\text{Ni}_{0.33}\text{O}_2$ is lower than that of P2-type $\text{Na}_{0.67}\text{Mn}_{0.67}\text{Ni}_{0.33}\text{O}_2$. This indicates lower energy consumption during the preparation of P3-type material. P3-type $\text{Na}_{0.67}\text{Mn}_{0.67}\text{Ni}_{0.33}\text{O}_2$ delivers higher initial capacities than P2-type $\text{Na}_{0.67}\text{Mn}_{0.67}\text{Ni}_{0.33}\text{O}_2$ as cathode for sodium ion batteries. The discharge capacity retention of P3-type material is lower than that of P2-type material. During cycling of P2-type and P3-type material, Mn and Ni atoms both join the redox reaction but the redox activity of Ni atoms mainly contributes to the capacities of P3-type material.
- The local structural changes around Mn and Ni atoms in P3-type $\text{Na}_{0.67}\text{Mn}_{0.67}\text{Ni}_{0.33}\text{O}_2$ are investigated by EXAFS. During charge, MnO_6 and NiO_6 units shrink within the a - b plane. During discharge, MnO_6 and NiO_6 units expand within the a - b plane. Na atoms prefer to occupy sites around Ni. The previous sites of Na remain as vacancies around Mn. This is a result of the electrostatic interaction between TM and Na atoms and the ordered arrangement of TM ions. The different occupancy of Na around Mn and Ni leads to different electrostatic interactions between Na and TMO_6 units, which have different effects on structural changes of MnO_6 and NiO_6 units during the cycling. Hence, changing the ordered arrangement of Mn and Ni into the disordered

distribution likely decreases the dimensional changes of NiO_6 units caused by the extraction and insertion of Na around Ni and improves the cycling performance.

- Core-shell design is an effective method to improve the electrochemical performance of P3-type $\text{Na}_{0.67}\text{Mn}_{0.67}\text{Ni}_{0.33}\text{O}_2$. In the precursor of the core-shell designed P3-type $\text{Na}_{0.67}\text{Mn}_{0.67}\text{Ni}_{0.33}\text{O}_2$, Ni rich material is designed as the core and the shell is made up of Mn rich material. The crystal structure of the core-shell designed material is the same as that of the normal P3-type counterpart. However, the particles on the surface of the core-shell designed material are smaller than that of the normal P3-type material. The core-shell designed P3-type material demonstrates higher initial capacities in the voltage range 1.5 - 4.5 V and better cycling performance in the voltage range 2.0 - 4.1 V in comparison to normal P3-type material.
- Core-shell designed P3-type $\text{Na}_{0.67}\text{Mn}_{0.67}\text{Ni}_{0.33}\text{O}_2$ is a promising cathode for fast charged and discharged sodium ion batteries in the voltage range 2.0 - 4.1 V. The reason for better cycling performance of the core-shell designed P3-type material is ascribed to a better structural stability of the crystal structure and TMO_2 layers in the core-shell designed P3-type $\text{Na}_{0.67}\text{Mn}_{0.67}\text{Ni}_{0.33}\text{O}_2$.

7 Outlook

Followings are the recommendations for future work:

- Core-shell designed P3-type $\text{Na}_{0.67}\text{Mn}_{0.67}\text{Ni}_{0.33}\text{O}_2$ demonstrates better cycling performance. However, its capacities are relatively low during fast and slow cycling. Hence, some other core-shell designed P3-type materials with higher concentrations of Na should be explored to enlarge the specific capacities of those materials.
- Because Ni atoms are the main part of the redox reaction and contribute to the capacities of P3-type $\text{Na}_{0.67}\text{Mn}_{0.67}\text{Ni}_{0.33}\text{O}_2$, increasing the concentration of Ni in the core-shell designed P3-type $\text{Na}_{0.67}\text{Mn}_x\text{Ni}_{1-x}\text{O}_2$ is supposed to be an effective method to increase the specific capacities. However, this will lead to more pronounced capacity fading in $\text{Na}_{0.67}\text{Mn}_x\text{Ni}_{1-x}\text{O}_2$. Hence, the optimal molar ratio between Mn and Ni should be investigated.
- Although the core-shell designed P3-type $\text{Na}_{0.67}\text{Mn}_{0.67}\text{Ni}_{0.33}\text{O}_2$ delivers higher initial capacities than the normal P3-type material in the voltage range 1.5 - 4.5 V, the severe capacity decay in the voltage range 1.5 - 4.5 V still hinders its practical application. Doping or surface modification could be performed to improve the cycling performance of the core-shell designed P3-type material at larger operate potential.

8 Reference

- [1] B. L. Ellis and L. F. Nazar. Sodium and sodium-ion energy storage batteries. *Current Opinion in Solid State and Materials Science* [J]. 2012, 16 (4): 168-177
- [2] Y. Kim, K. H. Ha, S. M. Oh and K. T. Lee. High-capacity anode materials for sodium-ion batteries. *Chemistry-A European Journal* [J]. 2014, 20 (38): 11980-11992
- [3] X. Xiang, K. Zhang and J. Chen. Recent advances and prospects of cathode materials for sodium-ion batteries. *Advanced materials* [J]. 2015, 27 (36): 5343-5364
- [4] S. W. Kim, D. H. Seo, X. Ma, G. Ceder and K. Kang. Electrode materials for rechargeable sodium-ion batteries: potential alternatives to current lithium-ion batteries. *Advanced Energy Materials* [J]. 2012, 2 (7): 710-721
- [5] M. H. Han, E. Gonzalo, G. Singh and T. Rojo. A comprehensive review of sodium layered oxides: powerful cathodes for Na-ion batteries. *Energy & Environmental Science* [J]. 2015, 8 (1): 81-102
- [6] M. D. Slater, D. Kim, E. Lee and C. S. Johnson. Sodium-ion batteries. *Advanced Functional Materials* [J]. 2013, 23 (8): 947-958
- [7] T. Risthaus, D. Zhou, X. Cao, X. He, B. Qiu, J. Wang, L. Zhang, Z. Liu, E. Paillard and G. Schumacher. A high-capacity P2 $\text{Na}_{2/3}\text{Ni}_{1/3}\text{Mn}_{2/3}\text{O}_2$ cathode material for sodium ion batteries with oxygen activity. *Journal of Power Sources* [J]. 2018, 395 16-24
- [8] P. Hou, J. Yin, X. Lu, J. Li, Y. Zhao and X. Xu. A stable layered P3/P2 and spinel intergrowth nanocomposite as a long-life and high-rate cathode for sodium-ion batteries. *Nanoscale* [J]. 2018, 10 (14): 6671-6677
- [9] C. Delmas, C. Fouassier and P. Hagenmuller. Structural classification and properties of the layered oxides. *Physica B+ c* [J]. 1980, 99 (1-4): 81-85
- [10] S. M. Kang, J.-H. Park, A. Jin, Y. H. Jung, J. Mun and Y.-E. Sung. Na^+ /vacancy disordered P2- $\text{Na}_{0.67}\text{Co}_{1-x}\text{Ti}_x\text{O}_2$: high-energy and high-power cathode materials for sodium ion batteries. *ACS applied materials & interfaces* [J]. 2018, 10 (4): 3562-3570
- [11] Y. Tsuchiya, K. Takanashi, T. Nishinobo, A. Hokura, M. Yonemura, T. Matsukawa, T. Ishigaki, K. Yamanaka, T. Ohta and N. Yabuuchi. Layered $\text{Na}_x\text{Cr}_x\text{Ti}_{1-x}\text{O}_2$ as bifunctional electrode materials for rechargeable sodium batteries. *Chemistry of Materials* [J]. 2016, 28 (19): 7006-7016

- [12] H. Hou, B. Gan, Y. Gong, N. Chen and C. Sun. P2-type $\text{Na}_{0.67}\text{Ni}_{0.23}\text{Mg}_{0.1}\text{Mn}_{0.67}\text{O}_2$ as a high-performance cathode for a sodium-ion battery. *Inorganic chemistry* [J]. 2016, 55 (17): 9033-9037
- [13] J. Billaud, G. Singh, A. R. Armstrong, E. Gonzalo, V. Roddatis, M. Armand, T. Rojo and P. G. Bruce. $\text{Na}_{0.67}\text{Mn}_{1-x}\text{Mg}_x\text{O}_2$ ($0 \leq x \leq 0.2$): a high capacity cathode for sodium-ion batteries. *Energy & Environmental Science* [J]. 2014, 7 (4): 1387-1391
- [14] N. Yabuuchi, M. Kajiyama, J. Iwatate, H. Nishikawa, S. Hitomi, R. Okuyama, R. Usui, Y. Yamada and S. Komaba. P2-type $\text{Na}_x[\text{Fe}_{1/2}\text{Mn}_{1/2}]\text{O}_2$ made from earth-abundant elements for rechargeable Na batteries. *Nature materials* [J]. 2012, 11 (6): 512
- [15] C. Didier, M. Guignard, M. R. Suchomel, D. Carlier, J. Darriet and C. Delmas. Thermally and electrochemically driven topotactical transformations in sodium layered oxides Na_xVO_2 . *Chemistry of Materials* [J]. 2016, 28 (5): 1462-1471
- [16] S.-H. Bo, X. Li, A. J. Toumar and G. Ceder. Layered-to-rock-salt transformation in desodiated Na_xCrO_2 ($x < 0.4$). *Chemistry of Materials* [J]. 2016, 28 (5): 1419-1429
- [17] X. Ma, H. Chen and G. Ceder. Electrochemical properties of monoclinic NaMnO_2 . *Journal of The Electrochemical Society* [J]. 2011, 158 (12): A1307-A1312
- [18] J. Zhao, L. Zhao, N. Dimov, S. Okada and T. Nishida. Electrochemical and thermal properties of $\alpha\text{-NaFeO}_2$ cathode for Na-ion batteries. *Journal of The Electrochemical Society* [J]. 2013, 160 (5): A3077-A3081
- [19] X. Wang, G. Liu, T. Iwao, M. Okubo and A. Yamada. Role of ligand-to-metal charge transfer in O3-type $\text{NaFeO}_2\text{-NaNiO}_2$ solid solution for enhanced electrochemical properties. *The Journal of Physical Chemistry C* [J]. 2014, 118 (6): 2970-2976
- [20] D. Yuan, W. He, F. Pei, F. Wu, Y. Wu, J. Qian, Y. Cao, X. Ai and H. Yang. Synthesis and electrochemical behaviors of layered $\text{Na}_{0.67}[\text{Mn}_{0.65}\text{Co}_{0.2}\text{Ni}_{0.15}]\text{O}_2$ microflakes as a stable cathode material for sodium-ion batteries. *Journal of Materials Chemistry A* [J]. 2013, 1 (12): 3895-3899
- [21] H. Yu, S. Guo, Y. Zhu, M. Ishida and H. Zhou. Novel titanium-based O3-type $\text{NaTi}_{0.5}\text{Ni}_{0.5}\text{O}_2$ as a cathode material for sodium ion batteries. *Chemical Communications* [J]. 2014, 50 (4): 457-459
- [22] Q. Liu, Z. Hu, M. Chen, Q. Gu, Y. Dou, Z. Sun, S. Chou and S. X. Dou. Multiangular rod-shaped $\text{Na}_{0.44}\text{MnO}_2$ as cathode materials with high rate and long life for sodium-ion batteries. *ACS applied materials & interfaces* [J]. 2017, 9 (4): 3644-3652
- [23] B. Fu, X. Zhou and Y. Wang. High-rate performance electrospun $\text{Na}_{0.44}\text{MnO}_2$ nanofibers as cathode material for sodium-ion batteries. *Journal of Power Sources* [J]. 2016, 310 102-108
- [24] S. Guo, H. Yu, D. Liu, W. Tian, X. Liu, N. Hanada, M. Ishida and H. Zhou. A novel tunnel $\text{Na}_{0.61}\text{Ti}_{0.48}\text{Mn}_{0.52}\text{O}_2$ cathode material for sodium-ion batteries. *Chemical Communications* [J]. 2014, 50 (59): 7998-8001
- [25] S. Xu, Y. Wang, L. Ben, Y. Lyu, N. Song, Z. Yang, Y. Li, L. Mu, H. T. Yang and L. Gu. Fe-based tunnel-type $\text{Na}_{0.61}[\text{Mn}_{0.27}\text{Fe}_{0.34}\text{Ti}_{0.39}]\text{O}_2$ designed by a new strategy as a cathode material for sodium-ion batteries. *Advanced Energy Materials* [J]. 2015, 5 (22): 1501156
- [26] Y. Wang, J. Liu, B. Lee, R. Qiao, Z. Yang, S. Xu, X. Yu, L. Gu, Y.-S. Hu and W. Yang. Ti-substituted tunnel-type $\text{Na}_{0.44}\text{MnO}_2$ oxide as a negative electrode for aqueous sodium-ion batteries. *Nature communications* [J]. 2015, 6 6401

- [27] W. Shen, C. Wang, H. Liu and W. Yang. Towards highly stable storage of sodium ions: a porous $\text{Na}_3\text{V}_2(\text{PO}_4)_3/\text{C}$ cathode material for sodium-ion batteries. *Chemistry-A European Journal* [J]. 2013, 19 (43): 14712-14718
- [28] S. M. Wood, C. Eames, E. Kendrick and M. S. Islam. Sodium ion diffusion and voltage trends in phosphates $\text{Na}_4\text{M}_3(\text{PO}_4)_2\text{P}_2\text{O}_7$ (M= Fe, Mn, Co, Ni) for possible high-rate cathodes. *The Journal of Physical Chemistry C* [J]. 2015, 119 (28): 15935-15941
- [29] P. Barpanda, T. Ye, S.-i. Nishimura, S.-C. Chung, Y. Yamada, M. Okubo, H. Zhou and A. Yamada. Sodium iron pyrophosphate: a novel 3.0 V iron-based cathode for sodium-ion batteries. *Electrochemistry communications* [J]. 2012, 24 116-119
- [30] B. Ellis, W. Makahnouk, Y. Makimura, K. Toghill and L. Nazar. A multifunctional 3.5 V iron-based phosphate cathode for rechargeable batteries. *Nature materials* [J]. 2007, 6 (10): 749
- [31] G. Oyama, S. i. Nishimura, Y. Suzuki, M. Okubo and A. Yamada. Off-stoichiometry in alluaudite-type sodium iron sulfate $\text{Na}^{2+}_{2x}\text{Fe}_{2-x}(\text{SO}_4)_3$ as an advanced sodium battery cathode material. *ChemElectroChem* [J]. 2015, 2 (7): 1019-1023
- [32] P. Barpanda, J. Lu, T. Ye, M. Kajiyama, S.-C. Chung, N. Yabuuchi, S. Komaba and A. Yamada. A layer-structured $\text{Na}_2\text{CoP}_2\text{O}_7$ pyrophosphate cathode for sodium-ion batteries. *Rsc Advances* [J]. 2013, 3 (12): 3857-3860
- [33] C.-Y. Chen, K. Matsumoto, T. Nohira, R. Hagiwara, Y. Orikasa and Y. Uchimoto. Pyrophosphate $\text{Na}_2\text{FeP}_2\text{O}_7$ as a low-cost and high-performance positive electrode material for sodium secondary batteries utilizing an inorganic ionic liquid. *Journal of Power Sources* [J]. 2014, 246 783-787
- [34] K. Saravanan, C. W. Mason, A. Rudola, K. H. Wong and P. Balaya. The first report on excellent cycling stability and superior rate capability of $\text{Na}_3\text{V}_2(\text{PO}_4)_3$ for sodium ion batteries. *Advanced Energy Materials* [J]. 2013, 3 (4): 444-450
- [35] K. H. Ha, S. H. Woo, D. Mok, N. S. Choi, Y. Park, S. M. Oh, Y. Kim, J. Kim, J. Lee and L. F. Nazar. $\text{Na}_{4-\alpha}\text{M}^{2+}_{\alpha/2}(\text{P}_2\text{O}_7)_2$ ($2/3 \leq \alpha \leq 7/8$, M= Fe, $\text{Fe}_{0.5}\text{Mn}_{0.5}$, Mn): a promising sodium ion cathode for Na - ion batteries. *Advanced Energy Materials* [J]. 2013, 3 (6): 770-776
- [36] D.-l. Ma, H.-g. Wang, Y. Li, D. Xu, S. Yuan, X.-l. Huang, X.-b. Zhang and Y. Zhang. In situ generated FeF_3 in homogeneous iron matrix toward high-performance cathode material for sodium-ion batteries. *Nano Energy* [J]. 2014, 10 295-304
- [37] I. D. Gocheva, M. Nishijima, T. Doi, S. Okada, J.-i. Yamaki and T. Nishida. Mechanochemical synthesis of NaMF_3 (M= Fe, Mn, Ni) and their electrochemical properties as positive electrode materials for sodium batteries. *Journal of Power Sources* [J]. 2009, 187 (1): 247-252
- [38] A. Kitajou, J. Yamaguchi, S. Hara and S. Okada. Discharge/charge reaction mechanism of a pyrite-type FeS_2 cathode for sodium secondary batteries. *Journal of Power Sources* [J]. 2014, 247 391-395
- [39] L. Wang, J. Song, R. Qiao, L. A. Wray, M. A. Hossain, Y.-D. Chuang, W. Yang, Y. Lu, D. Evans and J.-J. Lee. Rhombohedral prussian white as cathode for rechargeable sodium-ion batteries. *Journal of the American Chemical Society* [J]. 2015, 137 (7): 2548-2554
- [40] X. Wu, Y. Luo, M. Sun, J. Qian, Y. Cao, X. Ai and H. Yang. Low-defect prussian blue nanocubes as high capacity and long life cathodes for aqueous Na-ion batteries. *Nano Energy* [J]. 2015, 13 117-123
- [41] C. P. Guntlin, T. Zünd, K. V. Kravchyk, M. Wörle, M. I. Bodnarchuk and M. V. Kovalenko. Nanocrystalline FeF_3 and MF_2 (M= Fe, Co, and Mn) from metal

- trifluoroacetates and their Li (Na)-ion storage properties. *Journal of Materials Chemistry A* [J]. 2017, 5 (16): 7383-7393
- [42] N. Yabuuchi, K. Kubota, M. Dahbi and S. Komaba. Research development on sodium-ion batteries. *Chemical reviews* [J]. 2014, 114 (23): 11636-11682
- [43] K. Sakaushi, E. Hosono, G. Nickerl, T. Gemming, H. Zhou, S. Kaskel and J. Eckert. Aromatic porous-honeycomb electrodes for a sodium-organic energy storage device. *Nature communications* [J]. 2013, 4 1485
- [44] D. Stevens and J. Dahn. High capacity anode materials for rechargeable sodium-ion batteries. *Journal of the Electrochemical Society* [J]. 2000, 147 (4): 1271-1273
- [45] Y. Xu, Y. Zhu, Y. Liu and C. Wang. Electrochemical performance of porous carbon/tin composite anodes for sodium-ion and lithium-ion batteries. *Advanced Energy Materials* [J]. 2013, 3 (1): 128-133
- [46] J. Sun, H.-W. Lee, M. Pasta, H. Yuan, G. Zheng, Y. Sun, Y. Li and Y. Cui. A phosphorene-graphene hybrid material as a high-capacity anode for sodium-ion batteries. *Nature nanotechnology* [J]. 2015, 10 (11): 980
- [47] Y. Cao, L. Xiao, M. L. Sushko, W. Wang, B. Schwenzer, J. Xiao, Z. Nie, L. V. Saraf, Z. Yang and J. Liu. Sodium ion insertion in hollow carbon nanowires for battery applications. *Nano letters* [J]. 2012, 12 (7): 3783-3787
- [48] F. Yang, Z. Zhang, K. Du, X. Zhao, W. Chen, Y. Lai and J. Li. Dopamine derived nitrogen-doped carbon sheets as anode materials for high-performance sodium ion batteries. *Carbon* [J]. 2015, 91 88-95
- [49] H. g. Wang, Z. Wu, F. l. Meng, D. l. Ma, X. l. Huang, L. m. Wang and X. b. Zhang. Nitrogen-doped porous carbon nanosheets as low-cost, high-performance anode material for sodium-ion batteries. *ChemSusChem* [J]. 2013, 6 (1): 56-60
- [50] Y. Qu, Z. Zhang, K. Du, W. Chen, Y. Lai, Y. Liu and J. Li. Synthesis of nitrogen-containing hollow carbon microspheres by a modified template method as anodes for advanced sodium-ion batteries. *Carbon* [J]. 2016, 105 103-112
- [51] R. Alcántara, P. Lavela, G. F. Ortiz, J. L. Tirado, R. Menéndez, R. Santamaría and J. M. Jimenez-Mateos. Electrochemical, textural and microstructural effects of mechanical grinding on graphitized petroleum coke for lithium and sodium batteries. *Carbon* [J]. 2003, 41 (15): 3003-3013
- [52] D. Datta, J. Li and V. B. Shenoy. Defective graphene as a high-capacity anode material for Na-and Ca-ion batteries. *ACS applied materials & interfaces* [J]. 2014, 6 (3): 1788-1795
- [53] Y. Wen, K. He, Y. Zhu, F. Han, Y. Xu, I. Matsuda, Y. Ishii, J. Cumings and C. Wang. Expanded graphite as superior anode for sodium-ion batteries. *Nature communications* [J]. 2014, 5:4033
- [54] J. Wang, C. Luo, T. Gao, A. Langrock, A. C. Mignerey and C. Wang. An advanced MoS₂/carbon anode for high-performance sodium-ion batteries. *Small* [J]. 2015, 11 (4): 473-481
- [55] L. David, R. Bhandavat and G. Singh. MoS₂/graphene composite paper for sodium-ion battery electrodes. *ACS nano* [J]. 2014, 8 (2): 1759-1770
- [56] Y. Yan, Y. X. Yin, Y. G. Guo and L. J. Wan. A sandwich-like hierarchically porous carbon/graphene composite as a high-performance anode material for sodium-ion batteries. *Advanced Energy Materials* [J]. 2014, 4 (8): 1301584
- [57] C.-H. Lim, T.-Y. Huang, P.-S. Shao, J.-H. Chien, Y.-T. Weng, H.-F. Huang, B. J. Hwang and N.-L. Wu. Experimental study on sodiation of amorphous silicon for use as sodium-ion battery anode. *Electrochimica Acta* [J]. 2016, 211 265-272
- [58] L. Baggetto, J. K. Keum, J. F. Browning and G. M. Veith. Germanium as negative electrode material for sodium-ion batteries. *Electrochemistry Communications* [J]. 2013, 34 41-44

- [59] Z. Li, J. Ding and D. Mitlin. Tin and tin compounds for sodium ion battery anodes: phase transformations and performance. *Accounts of chemical research* [J]. 2015, 48 (6): 1657-1665
- [60] H. Hou, M. Jing, Y. Yang, Y. Zhu, L. Fang, W. Song, C. Pan, X. Yang and X. Ji. Sodium/lithium storage behavior of antimony hollow nanospheres for rechargeable batteries. *ACS applied materials & interfaces* [J]. 2014, 6 (18): 16189-16196
- [61] C. Yue, Y. Yu, S. Sun, X. He, B. Chen, W. Lin, B. Xu, M. Zheng, S. Wu and J. Li. High performance 3D Si/Ge nanorods array anode buffered by TiN/Ti interlayer for sodium-ion batteries. *Advanced Functional Materials* [J]. 2015, 25 (9): 1386-1392
- [62] H. Xie, W. P. Kalisvaart, B. C. Olsen, E. J. Lubner, D. Mitlin and J. M. Buriak. Sn-Bi-Sb alloys as anode materials for sodium ion batteries. *Journal of Materials Chemistry A* [J]. 2017, 5 (20): 9661-9670
- [63] M. He, M. Walter, K. V. Kravchyk, R. Erni, R. Widmer and M. V. Kovalenko. Monodisperse SnSb nanocrystals for Li-ion and Na-ion battery anodes: synergy and dissonance between Sn and Sb. *Nanoscale* [J]. 2015, 7 (2): 455-459
- [64] L. Baggetto, M. Marszewski, J. Górka, M. Jaroniec and G. M. Veith. AlSb thin films as negative electrodes for Li-ion and Na-ion batteries. *Journal of Power Sources* [J]. 2013, 243 699-705
- [65] L. Baggetto, E. Allcorn, A. Manthiram and G. M. Veith. Cu₂Sb thin films as anode for Na-ion batteries. *Electrochemistry Communications* [J]. 2013, 27 168-171
- [66] L. Baggetto, E. Allcorn, R. R. Unocic, A. Manthiram and G. M. Veith. Mo₃Sb₇ as a very fast anode material for lithium-ion and sodium-ion batteries. *Journal of Materials Chemistry A* [J]. 2013, 1 (37): 11163-11169
- [67] R. Ding, L. Qi and H. Wang. An investigation of spinel NiCo₂O₄ as anode for Na-ion capacitors. *Electrochimica Acta* [J]. 2013, 114 726-735
- [68] W.-H. Ryu, J.-W. Jung, K. Park, S.-J. Kim and I.-D. Kim. Vine-like MoS₂ anode materials self-assembled from 1-D nanofibers for high capacity sodium rechargeable batteries. *Nanoscale* [J]. 2014, 6 (19): 10975-10981
- [69] H. Xiong, M. D. Slater, M. Balasubramanian, C. S. Johnson and T. Rajh. Amorphous TiO₂ nanotube anode for rechargeable sodium ion batteries. *The journal of physical chemistry letters* [J]. 2011, 2 (20): 2560-2565
- [70] Q. Sun, Y. Dai, Y. Ma, T. Jing, W. Wei and B. Huang. Ab initio prediction and characterization of Mo₂C monolayer as anodes for lithium-ion and sodium-ion batteries. *The journal of physical chemistry letters* [J]. 2016, 7 (6): 937-943
- [71] J. Fullenwarth, A. Darwiche, A. Soares, B. Donnadieu and L. Monconduit. NiP₃: a promising negative electrode for Li-and Na-ion batteries. *Journal of Materials Chemistry A* [J]. 2014, 2 (7): 2050-2059
- [72] T. Yu, Z. Zhao, L. Liu, S. Zhang, H. Xu and G. Yang. TiC₃ monolayer with high specific capacity for sodium-ion batteries. *Journal of the American Chemical Society* [J]. 2018, 140 (18): 5962-5968
- [73] R. Alcántara, M. Jaraba, P. Lavela and J. Tirado. NiCo₂O₄ spinel: first report on a transition metal oxide for the negative electrode of sodium-ion batteries. *Chemistry of Materials* [J]. 2002, 14 (7): 2847-2848
- [74] C. Bommier and X. Ji. Electrolytes, SEI formation, and binders: a review of nonelectrode factors for sodium-ion battery anodes. *Small* [J]. 2018, 14 (16): 1703576
- [75] K. Vignarooban, R. Kushagra, A. Elango, P. Badami, B.-E. Mellander, X. Xu, T. Tucker, C. Nam and A. M. Kannan. Current trends and future challenges of

- electrolytes for sodium-ion batteries. *International Journal of Hydrogen Energy* [J]. 2016, 41 (4): 2829-2846
- [76] A. Ponrouch, E. Marchante, M. Courty, J.-M. Tarascon and M. R. Palacin. In search of an optimized electrolyte for Na-ion batteries. *Energy & Environmental Science* [J]. 2012, 5 (9): 8572-8583
- [77] A. Ponrouch, D. Monti, A. Boschini, B. Steen, P. Johansson and M. Palacin. Non-aqueous electrolytes for sodium-ion batteries. *Journal of Materials Chemistry A* [J]. 2015, 3 (1): 22-42
- [78] E. Jónsson and P. Johansson. Modern battery electrolytes: ion-ion interactions in Li^+/Na^+ conductors from DFT calculations. *Physical Chemistry Chemical Physics* [J]. 2012, 14 (30): 10774-10779
- [79] S. Komaba, T. Ishikawa, N. Yabuuchi, W. Murata, A. Ito and Y. Ohsawa. Fluorinated ethylene carbonate as electrolyte additive for rechargeable Na batteries. *ACS applied materials & interfaces* [J]. 2011, 3 (11): 4165-4168
- [80] L. Wu, D. Buchholz, D. Bresser, L. G. Chagas and S. Passerini. Anatase TiO_2 nanoparticles for high power sodium-ion anodes. *Journal of power sources* [J]. 2014, 251 379-385
- [81] J. Huang, D. Yuan, H. Zhang, Y. Cao, G. Li, H. Yang and X. Gao. Electrochemical sodium storage of $\text{TiO}_2(\text{B})$ nanotubes for sodium ion batteries. *Rsc Advances* [J]. 2013, 3 (31): 12593-12597
- [82] A. Bhide, J. Hofmann, A. K. Dürr, J. Janek and P. Adelhelm. Electrochemical stability of non-aqueous electrolytes for sodium-ion batteries and their compatibility with $\text{Na}_{0.7}\text{CoO}_2$. *Physical Chemistry Chemical Physics* [J]. 2014, 16 (5): 1987-1998
- [83] F. Wu, N. Zhu, Y. Bai, L. Liu, H. Zhou and C. Wu. Highly safe ionic liquid electrolytes for sodium-ion battery: wide electrochemical window and good thermal stability. *ACS applied materials & interfaces* [J]. 2016, 8 (33): 21381-21386
- [84] D. Monti, E. Jónsson, M. R. Palacin and P. Johansson. Ionic liquid based electrolytes for sodium-ion batteries: Na^+ solvation and ionic conductivity. *Journal of Power Sources* [J]. 2014, 245 630-636
- [85] H. Pan, X. Lu, X. Yu, Y. S. Hu, H. Li, X. Q. Yang and L. Chen. Sodium storage and transport properties in layered $\text{Na}_2\text{Ti}_3\text{O}_7$ for room-temperature sodium-ion batteries. *Advanced Energy Materials* [J]. 2013, 3 (9): 1186-1194
- [86] J. Qian, Y. Chen, L. Wu, Y. Cao, X. Ai and H. Yang. High capacity Na-storage and superior cyclability of nanocomposite Sb/C anode for Na-ion batteries. *Chemical Communications* [J]. 2012, 48 (56): 7070-7072
- [87] R. J. Clément, J. Billaud, A. R. Armstrong, G. Singh, T. Rojo, P. G. Bruce and C. P. Grey. Structurally stable Mg-doped $\text{P2-Na}_{2/3}\text{Mn}_{1-y}\text{Mg}_y\text{O}_2$ sodium-ion battery cathodes with high rate performance: insights from electrochemical, NMR and diffraction studies. *Energy & Environmental Science* [J]. 2016, 9 (10): 3240-3251
- [88] Y. Xiao, P. F. Wang, Y. X. Yin, Y. F. Zhu, X. Yang, X. D. Zhang, Y. Wang, X. D. Guo, B. H. Zhong and Y. G. Guo. A layered-tunnel intergrowth structure for high-performance sodium-ion oxide cathode. *Advanced Energy Materials* [J]. 2018, 8 (22): 1800492
- [89] F. De Groot. High-resolution X-ray emission and X-ray absorption spectroscopy. *Chemical Reviews* [J]. 2001, 101 (6): 1779-1808
- [90] C. Ma, J. Alvarado, J. Xu, R. I. J. Clément, M. Kodur, W. Tong, C. P. Grey and Y. S. Meng. Exploring oxygen activity in the high energy P2-type $\text{Na}_{0.78}\text{Ni}_{0.23}\text{Mn}_{0.69}\text{O}_2$ cathode material for Na-ion batteries. *Journal of the American Chemical Society* [J]. 2017, 139 (13): 4835-4845

- [91] D. Cabaret, P. Saintavit, P. Ildefonse and A.-M. Flank. Full multiple scattering calculations of the X-ray absorption near edge structure at the magnesium K-edge in pyroxene. *American Mineralogist* [J]. 1998, 83 (3-4): 300-304
- [92] P.-H. Butler: Point Group Symmetry Applications, Methods and Tables. Plenum Press, New York and London 1981. 567
- [93] F. Farges, G. E. Brown and J. Rehr. Ti K-edge XANES studies of Ti coordination and disorder in oxide compounds: comparison between theory and experiment. *Physical Review B* [J]. 1997, 56 (4): 1809
- [94] K. Tohji, Y. Udagawa, S. Tanabe and A. Ueno. Catalyst preparation procedure probed by EXAFS spectroscopy. 1. nickel on silica. *Journal of the American Chemical Society* [J]. 1984, 106 (3): 612-617
- [95] B.-K. Teo, P. Lee, A. Simons, P. Eisenberger and B. Kincaid. EXAFS: approximation, parameterization, and chemical transferability of amplitude functions. *Journal of the American Chemical Society* [J]. 1977, 99 (11): 3854-3856
- [96] J.-J. Ding, Y.-N. Zhou, Q. Sun and Z.-W. Fu. Cycle performance improvement of NaCrO₂ cathode by carbon coating for sodium ion batteries. *Electrochemistry Communications* [J]. 2012, 22 85-88
- [97] J.-Y. Hwang, S.-T. Myung, J. U. Choi, C. S. Yoon, H. Yashiro and Y.-K. Sun. Resolving the degradation pathways of the O3-type layered oxide cathode surface through the nano-scale aluminum oxide coating for high-energy density sodium-ion batteries. *Journal of Materials Chemistry A* [J]. 2017, 5 (45): 23671-23680
- [98] Y. Liu, X. Fang, A. Zhang, C. Shen, Q. Liu, H. A. Enaya and C. Zhou. Layered P2-Na_{2/3}[Ni_{1/3}Mn_{2/3}]O₂ as high-voltage cathode for sodium-ion batteries: the capacity decay mechanism and Al₂O₃ surface modification. *Nano Energy* [J]. 2016, 27 27-34
- [99] T.-R. Chen, T. Sheng, Z.-G. Wu, J.-T. Li, E.-H. Wang, C.-J. Wu, H.-T. Li, X.-D. Guo, B.-H. Zhong and L. Huang. Cu²⁺ dual-doped layer-tunnel hybrid Na_{0.6}Mn_{1-x}Cu_xO₂ as a cathode of sodium-ion battery with enhanced structure stability, electrochemical property, and air stability. *ACS applied materials & interfaces* [J]. 2018, 10 (12): 10147-10156
- [100] X. Wu, J. Guo, D. Wang, G. Zhong, M. J. McDonald and Y. Yang. P2-type Na_{0.66}Ni_{0.33-x}Zn_xMn_{0.67}O₂ as new high-voltage cathode materials for sodium-ion batteries. *Journal of Power Sources* [J]. 2015, 281 18-26
- [101] X.-H. Zhang, W.-L. Pang, F. Wan, J.-Z. Guo, H.-Y. Lü, J.-Y. Li, Y.-M. Xing, J.-P. Zhang and X.-L. Wu. P2-Na_{2/3}Ni_{1/3}Mn_{5/9}Al_{1/9}O₂ microparticles as superior cathode material for sodium-ion batteries: enhanced properties and mechanism via graphene connection. *ACS applied materials & interfaces* [J]. 2016, 8 (32): 20650-20659
- [102] H. Yoshida, N. Yabuuchi, K. Kubota, I. Ikeuchi, A. Garsuch, M. Schulz-Dobrick and S. Komaba. P2-type Na_{2/3}Ni_{1/3}Mn_{2/3-x}Ti_xO₂ as a new positive electrode for higher energy Na-ion batteries. *Chemical communications* [J]. 2014, 50 (28): 3677-3680
- [103] L. Mu, S. Xu, Y. Li, Y. S. Hu, H. Li, L. Chen and X. Huang. Prototype sodium-ion batteries using an air-stable and Co/Ni-free O3-layered metal oxide cathode. *Advanced materials* [J]. 2015, 27 (43): 6928-6933
- [104] Y.-K. Sun, S.-T. Myung, B.-C. Park, J. Prakash, I. Belharouak and K. Amine. High-energy cathode material for long-life and safe lithium batteries. *Nature materials* [J]. 2009, 8 (4): 320

- [105] Y.-K. Sun, Z. Chen, H.-J. Noh, D.-J. Lee, H.-G. Jung, Y. Ren, S. Wang, C. S. Yoon, S.-T. Myung and K. Amine. Nanostructured high-energy cathode materials for advanced lithium batteries. *Nature materials* [J]. 2012, 11 (11): 942
- [106] Y.-K. Sun, B.-R. Lee, H.-J. Noh, H. Wu, S.-T. Myung and K. Amine. A novel concentration-gradient $\text{Li}[\text{Ni}_{0.83}\text{Co}_{0.07}\text{Mn}_{0.10}]\text{O}_2$ cathode material for high-energy lithium-ion batteries. *Journal of Materials chemistry* [J]. 2011, 21 (27): 10108-10112
- [107] J.-Y. Liao, S.-M. Oh and A. Manthiram. Core/double-shell type gradient Ni-rich $\text{LiNi}_{0.76}\text{Co}_{0.10}\text{Mn}_{0.14}\text{O}_2$ with high capacity and long cycle life for lithium-ion batteries. *ACS applied materials & interfaces* [J]. 2016, 8 (37): 24543-24549
- [108] Y. Wang, R. Xiao, Y.-S. Hu, M. Avdeev and L. Chen. $\text{P2-Na}_{0.6}[\text{Cr}_{0.6}\text{Ti}_{0.4}]\text{O}_2$ cation-disordered electrode for high-rate symmetric rechargeable sodium-ion batteries. *Nature communications* [J]. 2015, 6: 6954
- [109] D. M. Többsens and S. Zander. KMC-2: an X-ray beamline with dedicated diffraction and XAS endstations at BESSY II. *Journal of large-scale research facilities JLSRF* [J]. 2016, 2: 49
- [110] B. Ravel and M. Newville. ATHENA, ARTEMIS, HEPHAESTUS: data analysis for X-ray absorption spectroscopy using IFEFFIT. *Journal of synchrotron radiation* [J]. 2005, 12 (4): 537-541
- [111] Z. Lu, R. Donaberger and J. Dahn. Superlattice ordering of Mn, Ni, and Co in layered alkali transition metal oxides with P2, P3, and O3 structures. *Chemistry of materials* [J]. 2000, 12 (12): 3583-3590
- [112] J. J. Rehr and R. C. Albers. Theoretical approaches to X-ray absorption fine structure. *Reviews of modern physics* [J]. 2000, 72 (3): 621
- [113] X. Chen, X. Zhou, M. Hu, J. Liang, D. Wu, J. Wei and Z. Zhou. Stable layered P3/P2 $\text{Na}_{0.66}\text{Co}_{0.5}\text{Mn}_{0.5}\text{O}_2$ cathode materials for sodium-ion batteries. *Journal of Materials Chemistry A* [J]. 2015, 3 (41): 20708-20714
- [114] I. Zizak. mySpot: a versatile microfocussing station for scanning methods at BESSY II. *Journal of large-scale research facilities JLSRF* [J]. 2016, 2 101
- [115] J. Wang, X. He, D. Zhou, F. Schappacher, X. Zhang, H. Liu, M. C. Stan, X. Cao, R. Kloepsch and M. S. Sofy. O3-type $\text{Na}[\text{Fe}_{1/3}\text{Ni}_{1/3}\text{Ti}_{1/3}]\text{O}_2$ cathode material for rechargeable sodium ion batteries. *Journal of Materials Chemistry A* [J]. 2016, 4 (9): 3431-3437
- [116] P. F. Wang, H. R. Yao, X. Y. Liu, J. N. Zhang, L. Gu, X. Q. Yu, Y. X. Yin and Y. G. Guo. Ti-substituted $\text{NaNi}_{0.5}\text{Mn}_{0.5-x}\text{Ti}_x\text{O}_2$ cathodes with reversible O3-P3 phase transition for high-performance sodium-ion batteries. *Advanced Materials* [J]. 2017, 29 (19): 1700210
- [117] S. Kalluri, K. H. Seng, W. K. Pang, Z. Guo, Z. Chen, H.-K. Liu and S. X. Dou. Electrospun P2-type $\text{Na}_{2/3}(\text{Fe}_{1/2}\text{Mn}_{1/2})\text{O}_2$ hierarchical nanofibers as cathode material for sodium-ion batteries. *ACS applied materials & interfaces* [J]. 2014, 6 (12): 8953-8958
- [118] B. Song, E. Hu, J. Liu, Y. Zhang, X.-Q. Yang, J. Nanda, A. Huq and K. Page. A novel P3-type $\text{Na}_{2/3}\text{Mg}_{1/3}\text{Mn}_{2/3}\text{O}_2$ as high capacity sodium-ion cathode using reversible oxygen redox. *Journal of Materials Chemistry A* [J]. 2019, 7 (4): 1491-1498
- [119] D. Buchholz, L. G. Chagas, C. Vaalma, L. Wu and S. Passerini. Water sensitivity of layered P2/P3- $\text{Na}_x\text{Ni}_{0.22}\text{Co}_{0.11}\text{Mn}_{0.66}\text{O}_2$ cathode material. *Journal of Materials Chemistry A* [J]. 2014, 2 (33): 13415-13421
- [120] I. Hasa, D. Buchholz, S. Passerini, B. Scrosati and J. Hassoun. High performance $\text{Na}_{0.5}[\text{Ni}_{0.23}\text{Fe}_{0.13}\text{Mn}_{0.63}]\text{O}_2$ cathode for sodium-ion batteries. *Advanced Energy Materials* [J]. 2014, 4 (15): 1400083

- [121] E. Talaie, V. Duffort, H. L. Smith, B. Fultz and L. F. Nazar. Structure of the high voltage phase of layered $\text{P2-Na}_{2/3-z}[\text{Mn}_{1/2}\text{Fe}_{1/2}]\text{O}_2$ and the positive effect of Ni substitution on its stability. *Energy & Environmental Science* [J]. 2015, 8 (8): 2512-2523
- [122] P. F. Wang, Y. You, Y. X. Yin, Y. S. Wang, L. J. Wan, L. Gu and Y. G. Guo. Suppressing the P2-O2 phase transition of $\text{Na}_{0.67}\text{Mn}_{0.67}\text{Ni}_{0.33}\text{O}_2$ by magnesium substitution for improved sodium-ion batteries. *Angewandte Chemie International Edition* [J]. 2016, 55 (26): 7445-7449
- [123] J. Xu, D. H. Lee, R. I. J. Clément, X. Yu, M. Leskes, A. J. Pell, G. Pintacuda, X.-Q. Yang, C. P. Grey and Y. S. Meng. Identifying the critical role of Li substitution in $\text{P2-Na}_x[\text{Li}_y\text{Ni}_z\text{Mn}_{1-y-z}]\text{O}_2$ ($0 < x, y, z < 1$) intercalation cathode materials for high-energy Na-ion batteries. *Chemistry of Materials* [J]. 2014, 26 (2): 1260-1269
- [124] S. Komaba, N. Yabuuchi, T. Nakayama, A. Ogata, T. Ishikawa and I. Nakai. Study on the reversible electrode reaction of $\text{Na}_{1-x}\text{Ni}_{0.5}\text{Mn}_{0.5}\text{O}_2$ for a rechargeable sodium-ion battery. *Inorganic chemistry* [J]. 2012, 51 (11): 6211-6220
- [125] J. Paulsen and J. Dahn. Studies of the layered manganese bronzes, $\text{Na}_{2/3}[\text{Mn}_{1-x}\text{M}_x]\text{O}_2$ with $\text{M} = \text{Co}, \text{Ni}, \text{Li}$, and $\text{Li}_{2/3}[\text{Mn}_{1-x}\text{M}_x]\text{O}_2$ prepared by ion-exchange. *Solid State Ionics* [J]. 1999, 126 (1-2): 3-24
- [126] M. Ruiz-Lopez and A. Munoz-Paez. A theoretical study of the XANES spectra of rutile and anatase. *Journal of Physics: Condensed Matter* [J]. 1991, 3 (45): 8981
- [127] M. Belli, A. Scafati, A. Bianconi, S. Mobilio, L. Palladino, A. Reale and E. Burattini. X-ray absorption near edge structures (XANES) in simple and complex Mn compounds. *Solid State Communications* [J]. 1980, 35 (4): 355-361
- [128] S. Calvin. XAFS for everyone. CRC press: 2013
- [129] S. Webb. SIXpack: a graphical user interface for XAS analysis using IFEFFIT. *Physica scripta* [J]. 2005, 2005 (T115): 1011
- [130] D. Carlier, J. Cheng, R. Berthelot, M. Guignard, M. Yoncheva, R. Stoyanova, B. Hwang and C. Delmas. The $\text{P2-Na}_{2/3}\text{Co}_{2/3}\text{Mn}_{1/3}\text{O}_2$ phase: structure, physical properties and electrochemical behavior as positive electrode in sodium battery. *Dalton Transactions* [J]. 2011, 40 (36): 9306-9312
- [131] J. Rana, M. Stan, R. Kloepsch, J. Li, G. Schumacher, E. Welter, I. Zizak, J. Banhart and M. Winter. Structural changes in Li_2MnO_3 cathode material for Li-ion batteries. *Advanced Energy Materials* [J]. 2014, 4 (5): 1300998
- [132] X. Wu, G.-L. Xu, G. Zhong, Z. Gong, M. J. McDonald, S. Zheng, R. Fu, Z. Chen, K. Amine and Y. Yang. Insights into the effects of zinc doping on structural phase transition of P2-type sodium nickel manganese oxide cathodes for high-energy sodium ion batteries. *ACS applied materials & interfaces* [J]. 2016, 8 (34): 22227-22237
- [133] M. Cao, T. Wang, Z. Shadike, K. Nam, Y. Zhou and Z. Fu. Reversible multi-electron transfer of $\text{Cr}^{2.8+}/\text{Cr}^{4.4+}$ in O3-type layered $\text{Na}_{0.66}\text{Fe}_{1/3}\text{Cr}_{1/3}\text{Ti}_{1/3}\text{O}_2$ for sodium-ion batteries. *Journal of The Electrochemical Society* [J]. 2018, 165 (3): A565-A574
- [134] W. Olszewski, M. Ávila Pérez, C. Marini, E. Paris, X. Wang, T. Iwao, M. Okubo, A. Yamada, T. Mizokawa and N. L. Saini. Temperature dependent local structure of Na_xCoO_2 cathode material for rechargeable sodium-ion batteries. *The Journal of Physical Chemistry C* [J]. 2016, 120 (8): 4227-4232
- [135] Y. Tsai, B. Hwang, G. Ceder, H. Sheu, D. Liu and J. Lee. In-situ X-ray absorption spectroscopic study on variation of electronic transitions and local

- structure of $\text{LiNi}_{1/3}\text{Co}_{1/3}\text{Mn}_{1/3}\text{O}_2$ cathode material during electrochemical cycling. *Chemistry of materials* [J]. 2005, 17 (12): 3191-3199
- [136] Y. Wang, Z. Feng, S.-Z. Yang, C. Gagnon, V. Gariépy, D. Laul, W. Zhu, R. Veillette, M. L. Trudeau and A. Guerfi. Layered oxides- $\text{LiNi}_{1/3}\text{Co}_{1/3}\text{Mn}_{1/3}\text{O}_2$ as anode electrode for symmetric rechargeable lithium-ion batteries. *Journal of Power Sources* [J]. 2018, 378 516-521
- [137] T. Risthaus, D. Zhou, X. Cao, X. He, B. Qiu, J. Wang, L. Zhang, Z. Liu, E. Paillard and G. Schumacher. A high-capacity P2 $\text{Na}_{2/3}\text{Ni}_{1/3}\text{Mn}_{2/3}\text{O}_2$ cathode material for sodium ion batteries with oxygen activity. *Journal of Power Sources* [J]. 2018, 395: 16-24
- [138] R. T. Shannon and C. T. Prewitt. Effective ionic radii in oxides and fluorides. *Acta Crystallographica Section B: Structural Crystallography and Crystal Chemistry* [J]. 1969, 25 (5): 925-946
- [139] G. Singh, J. M. L. del Amo, M. Galceran, S. Pérez-Villar and T. Rojo. Structural evolution during sodium deintercalation/intercalation in $\text{Na}_{2/3}[\text{Fe}_{1/2}\text{Mn}_{1/2}]\text{O}_2$. *Journal of Materials Chemistry A* [J]. 2015, 3 (13): 6954-6961
- [140] D. Wu, X. Li, B. Xu, N. Twu, L. Liu and G. Ceder. NaTiO_2 : a layered anode material for sodium-ion batteries. *Energy & Environmental Science* [J]. 2015, 8 (1): 195-202
- [141] D. H. Lee, J. Xu and Y. S. Meng. An advanced cathode for Na-ion batteries with high rate and excellent structural stability. *Physical Chemistry Chemical Physics* [J]. 2013, 15 (9): 3304-3312
- [142] C. Chen, Y. Wen, X. Hu, X. Ji, M. Yan, L. Mai, P. Hu, B. Shan and Y. Huang. Na^+ intercalation pseudocapacitance in graphene-coupled titanium oxide enabling ultra-fast sodium storage and long-term cycling. *Nature communications* [J]. 2015, 6: 6929
- [143] G. Fang, Z. Wu, J. Zhou, C. Zhu, X. Cao, T. Lin, Y. Chen, C. Wang, A. Pan and S. Liang. Observation of pseudocapacitive effect and fast ion diffusion in bimetallic sulfides as an advanced sodium-ion battery anode. *Advanced Energy Materials* [J]. 2018, 8 (19): 1703155
- [144] J. Deng, W. B. Luo, X. Lu, Q. Yao, Z. Wang, H. K. Liu, H. Zhou and S. X. Dou. High energy density sodium-ion battery with industrially feasible and air-stable O3-type layered oxide cathode. *Advanced Energy Materials* [J]. 2018, 8 (5): 1701610
- [145] K. Park, D. Han, H. Kim, W.-s. Chang, B. Choi, B. Anass and S. Lee. Characterization of a P2-type chelating-agent-assisted $\text{Na}_{2/3}\text{Fe}_{1/2}\text{Mn}_{1/2}\text{O}_2$ cathode material for sodium-ion batteries. *RSC Advances* [J]. 2014, 4 (43): 22798-22802